MODELING IRRADIATION OF INTERSTELLAR ICES BY COSMIC RAYS

Alec G. Paulive

Boca Raton, Florida

Bachelor of Science, Chemistry, University of Florida, 2017

Bachelor of Arts, Philosophy, University of Florida, 2017

A Dissertation submitted to the Graduate Faculty

of the University of Virginia in Candidacy for the Degree of

Doctor of Philosophy

Department of Chemistry

University of Virginia

December 2022

Eric Herbst, Advisor

Rob T. Garrod, Chair

Kateri DuBay

Ilse Cleeves

Zhi-Yun Li

Modeling irradiation of interstellar ices by cosmic rays

Alec G. Paulive

(ABSTRACT)

Throughout the interstellar medium (ISM), there are multiple ongoing questions on the role of gaseous, dust surface, ice surface, and ice bulk chemistry in the formation of rotationally observed molecules. Both experiments and models suggest the importance of ices upon the grain surface in complex chemical formation, especially at low temperatures (Garrod et al., 2008; Herbst & van Dishoeck, 2009). Many recent discoveries of complex organic molecules (COMs) have occurred toward cold dark clouds, which were thought to have less chemical diversity compared to warmer star forming regions (SFRs), as the lack of higher temperature gas phase chemistry limited chemical models (McGuire, 2022). To explain the chemical diversity at 10 K in cold dark clouds, efficient low temperature chemical routes and desorption methods are needed (Herbst, 2021). Vast chemical networks, with over 15000 reactions, are utilized by computer models solving systems of rate equations to model the chemical evolution of environments in the ISM. As a way around the limitations of cold chemistry, bombardment of interstellar ices are a common source of energy throughout the interstellar medium. Irradiation caused by cosmic rays, atomic nuclei traveling at significant fractions of the speed of light, have previously been shown to increase chemical diversity of interstellar grain ices (Blasi, 2013; Abplanalp et al., 2016; Shingledecker et al., 2018). This thesis expands upon the chemistry of cosmic ray collisions with grain ices, by addressing the formation of $C_2H_4O_2$ isomers, and precursor chemistry leading to the formation and destruction of PAHs. The $C_2H_4O_2$ isomers are shown

to have increased abundances with the inclusion of radiolysis chemistry reactions, which is notable because glycolaldehyde is a sugar-adjacent molecule. Additionally, the added destruction pathways of these molecules do not reduce the predicted abundance, suggesting that the production is more efficient than destruction. Additionally, the chemical model is enhanced with a new non-thermal desorption method resulting from cosmic ray collisions with ices, called sputtering (Behrisch & Eckstein, 2007). Experiments and other models have shown sputtering via swift heavy ions to be effective at removing material from the surface of amorphous solid water, thought to be analagous to interstellar ices (Dartois et al., 2018; Wakelam et al., 2021). Models with sputtering enable significant desorption of all molecules on and within ices, though we do not see uniform increases in gas phase abundances for all species, partially because of efficient thermal gas-phase destruction pathways. The effects of sputtering on COMs and precursor species to PAHs is also addressed; while the inclusion of sputtering, radiolysis, and the expansion of the chemical network to include speculative grain reactions does increase the abundance of molecules to match with observation in the case of some molecules, not every molecule is enhanced enough with the inclusion of sputtering and radiolysis to match observations. We discuss the lack of thermal reactions as a possible reason, and possible remedies to the problem of three-phase models not reproducing observed abundances for PAH-related molecules and precursors.

Dedication

For Isabel,

For all of the people who encouraged the pursuit of knowledge,

For those who will read this,

Thank you

Contents

List of Figures **x**

List of Tables **xvii**

1 Introduction **1**

1.1 Astrochemical Background and History 1

1.2 Cosmic Rays and Collisional Effects 6

1.3 Rate-Equation Based Models 10

1.4 Scope of Thesis 13

2 Radiolysis of $C_2H_4O_2$ isomers and Dimethyl Ether in Cold Dark Clouds **15**

2.1 Introduction 16

2.2 Model 19

2.2.1 Nautilus 19

2.2.2 Network 20

2.2.3 Radiolysis 22

2.3 Results and Analysis 28

2.3.1 Methyl Formate 29

2.3.2 Acetic Acid . . . 33
2.3.3 Glycolaldehyde . . . 36
2.3.4 Dimethyl Ether . . . 39
2.4 Astrochemical Implications . . . 43
2.5 Conclusions . . . 49

3 Sputtering of interstellar dust grains 51
3.1 Introduction . . . 52
3.2 Models . . . 54
3.2.1 Network . . . 57
3.2.2 Sputtering Theory . . . 58
3.3 Results and Analysis . . . 71
3.3.1 Water Ice Models . . . 74
3.3.2 Carbon Dioxide Ice Models . . . 76
3.3.3 Mixed Ice Models . . . 79
3.4 Astrochemical Implications . . . 82
3.5 Conclusions . . . 89

4 Radiolysis and Sputtering of Naphthalene and Precursors 90
4.1 Introduction . . . 90
4.2 Models and Methods . . . 94

4.2.1 Network 95

4.2.2 Cosmic Ray - Ice Interactions 98

4.3 Results and Analysis 107

4.3.1 Benzene and Benzonitrile 107

4.3.2 Vinyl acetylene and C_4H_3CN Isomers 115

4.3.3 Propargyl radical, cyanopropyne, and 1-cyanopropargyl radical 118

4.3.4 Naphthalene, 1-cyanonaphthalene, and 2-cyanonaphthalene . . 122

4.4 Astrochemical Implications 125

4.5 Conclusions 128

5 Conclusions **130**

5.1 Major Conclusions 130

5.1.1 Chapter 2 130

5.1.2 Chapter 3 131

5.1.3 Chapter 4 132

5.2 Future Work 134

5.2.1 Radiolysis 134

5.2.2 Sputtering 135

5.2.3 General Surface Improvements 136

Bibliography **138**

Appendices **152**

Appendix A Supplementary material from Chapter 2 **153**

Appendix B Enhanced Sputtering and additional tables to environments other than TMC-1 for Chapter 3 **154**

Appendix C Additional Radiolysis Reactions relevant to Chapter 4 **159**

List of Figures

1.1 Simplified image of stellar life cycle, by G. A. Cruz Díaz, from NASA images 2

1.2 Image of Cosmic ray intensities against energy from multiple studies. Reproduced from (Blasi, 2013) 7

1.3 Modeled path of secondary electrons in water ice, with data from (Shingledecker et al., 2017). The initial path of the primary cosmic ray is in red, while secondary electrons are in black. 7

2.1 Abundance of methyl formate. Gas phase is in red, ice surface in green, and ice bulk in blue. Both models have the same physical and starting conditions, and are run at 10 K. The solid lines refer to the model without radiolysis (Model 1), while the dashed lines refer to the model with radiolysis turned on (Model 2). Horizontal black lines refer to observed abundances in L1689B, TMC-1, and B1-b. 34

2.2 Abundance of acetic acid. Gas phase is in red, ice surface in green, and ice bulk in blue. Both models have the same physical and starting conditions, and are run at 10 K. The solid lines show the model without radiolysis, while the dashed lines show the model with radiolysis turned on. 37

2.3 Abundance of glycolaldehyde. Gas phase is in red, ice surface in green, and ice bulk in blue. Both models have the same physical and starting conditions, and are run at 10 K. The solid line shows the model with radiolysis off, while the dashed line is the model with radiolysis turned on. 40

2.4 Abundance of dimethyl ether in the gas phase (red), ice surface (green), and ice bulk (blue). Both models have the same physical and starting conditions, and are run at 10 K. The solid line shows the model without radiolysis, while the dashed line is the model with radiolysis. Horizontal black lines refer to observed abundances in TMC-1, L1544, and B1-b. 41

2.5 Abundances of selected precursor species on the ice surface at 10 K. The solid line refers to the model without radiolysis (Model 1), while the dashed line refers to the model with radiolysis (Model 2). 44

2.6 Rates of relevant CH_3OCH_3 production mechanisms. Reactions 27 and 28 are in Model 1 (solid lines) and 2 (dashed lines), reactions 29, 31, and 32 are only in Model 2. 45

3.1 Cosmic ray energy distribution function, from Spitzer & Tomasko (1968). The cosmic ray flux in particles cm^{-2} s^{-1} is obtained by integrating j(E) over the cosmic ray energy distribution, from 3×10^{-4} GeV to 100 GeV. This results in an overall cosmic ray flux of 8.6 particles cm^{-2} s^{-1}. 62

3.2 Electronic and nuclear stopping powers of H^+ and Fe^{26+} ions impacting liquid water. H^+ electronic stopping powers are yellow dots, nuclear are purple dot-dashed. Iron incident ion electronic stopping powers are solid blue, nuclear are orange dashed. Energy ranges from 3×10^{-4} GeV to 100 GeV. At these energies, S_e of hydrogen is consistently $> 10^2$ than the S_n. Liquid water is used as an approximation for amorphous solid water, which is not included in the `SR-NIEL` web tool. Calculated using `SR-NIEL` web tools http://www.sr-niel.org/index.php/. 65

3.3 Heatmaps comparing models 1H and 2HS; each heatmap has model time on the y axis, with various species on the x axis. Species with a "J" designation represent surface ices, or a "K" for bulk ices. The different colours on the heatmap represent relative differences in abundance between models. Note the different colour bar scales and ranges 71

3.4 Heatmaps comparing models 1H and 3S; each heatmap has model time on the y axis, with various species on the x axis. Species with a "J" designation represent surface ices or a "K" for bulk ices. The different colours on the heatmap represent relative differences in abundance between species in the compared models. Note the different colour bar scales and ranges 72

3.5 Modeled fractional abundance of relevant COMs under cold dark cloud conditions at 10 K. Models 2HS and 3S have water ice sputtering rates of 2.55×10^{-18} cm^{-3} s^{-1} at 5×10^5 yr. The dashed line is model 2HS, the solid line is model 1H, the dotted-dashed line is model 3S. All COMs examined for this graph are gas-phase. Both sputtering models show increases in abundances for methyl formate and glycoaldehyde. 77

3.6 Gas-phase fractional abundances of select COMs with respect to hydrogen. Models 4HSC and 5SC have carbon dioxide ice sputtering rates of 1.48×10^{-16} cm^{-3} s^{-1} at 5×10^5 yr. Different colors represent different species. The fiducial model (1H) has a solid line, the model with carbon dioxide sputtering and heating (4HSC) a dashed line, and the model with just sputtering is has a dotted and dashed line (5SC). All molecules presented here show increases of varying degrees in gas-phase abundances, with acetaldehyde (CH_3CHO) showing less of an increase (a factor of 1.12) compared with other COMs when comparing abundnances between the models with sputtering and the fiducial model. 78

3.7 Gas-phase fractional abundances of select COMs with respect to hydrogen. Models 6HSM and 7SM have mixed water and carbon dioxide ice sputtering rates of 7.02×10^{-17} cm^{-3} s^{-1} for water and 8.21×10^{-17} cm^3 s^{-1} for carbon dioxide at 5×10^5 yr. Different colors represent different species, the fiducial model (1H) is a solid line, the model with carbon dioxide sputtering and heating (6HSM) is dashed, the model with pure sputtering is dotted and dashed (7SM). All molecules presented here show increases of varying degrees in gas-phase abundances, with the acetaldehyde (CH_3CHO) showing less of an increase compared to other COMs. 80

3.8 Grain surface and mantle abundances of water ice and carbon dioxide ice, for models 1H, 6HSM, and 7SM. Other models used in this work differ in water and carbon dioxide fractional abundance by 10% at most. The models from 1×10^3 yr and 1×10^6 yr have differences by factors of 0.0001, or approximately 0.01%. 81

4.1 Fractional abundances of benzene and benzonitrile with respect to hydrogen in the gas phase, ice surface, and ice bulk, each with a different color. The base model is represented through a solid line, the gas-phase only model is represented with a dashed line, and the model with radiolysis and sputtering is a dotted-dashed line. 108

4.2 Fractional abundances of vinyl acetylene and C_4H_3CN isomers with respect to hydrogen in the gas phase, ice surface, and ice bulk, each with a different color. The base model is represented through a solid line, the gas-phase only model is represented with a dashed line, and the model with radiolysis and sputtering is a dotted-dashed line. . . . 114

4.3 Fractional abundances of propargyl radical, cyanopropyne, and 1-cyanopropargyl with respect to hydrogen in the gas phase, ice surface, and ice bulk, each with a different color. The base model is represented through a solid line, the gas-phase only model is represented with a dashed line, and the model with radiolysis and sputtering is a dotted-dashed line. 119

4.4 Fractional abundances of naphthalene, 1-cyanonaphthalene, and 2-cyanonaphthalene with respect to hydrogen in the gas phase, ice surface, and ice bulk, each with a different color. The base model is represented through a solid line, the gas-phase only model is represented with a dashed line, and the model with radiolysis and sputtering is a dotted-dashed line. 122

B.1 Fractional abundance graphs of various ice species with respect to hydrogen. At the right are the surface abundances of select species, at the left are the bulk abundances. Individual species are a specific colour.At the top are common ices, while the bottom shows simple ices. Model 1H, without sputtering, is a solid line, models 4HSC and 5SC are dashed and dotted-dashed lines, respectively. Notable in these figures is that the ice abundances are not significantly affected by sputtering, showing that sputtering is not fast enough to significantly deplete ices on the grain surface, even with an increased rate coefficient for sputtering of CO_2 ices. 156

B.2 Fractional abundance graphs of various common ices with respect to hydrogen. At the right are the surface abundances of select species, at the left are the bulk abundances. Individual species are a specific colour. At the top are common ices, while the bottom is simple molecules. Model 1H, without sputtering, is a solid line, models 6HSM and 7SM are dashed and dotted-dashed lines, respectively. Notable in these figures is that the ice abundances are not significantly affected by sputtering, despite the increased sputtering rate coefficient of a mixed ice. 157

B.3 Plot of the fractional gas-phase abundance of various COMs with respect to hydrogen. Different species are different colours, the solid lines are model 1H, the dashed lines are model 4HSC, and the dotted-dashed lines are model 8HSC10, a model with 10 times the rate coefficient of sputtering in model 4HSC. The resulting rate of sputtering for carbon dioxide ices in model 8HSC10 is 1.42×10^{-15} cm^{-3} s^{-1}. 158

List of Tables

2.1 Initial abundances of elements with respect to total hydrogen nuclei . 21

2.2 Physical conditions for TMC-1 utilized 21

2.3 Binding Energies 22

2.4 Parameters used to estimate G values. 27

2.5 Estimated G values (extent per 100 eV) 27

3.1 Initial abundances of elements with respect to total hydrogen nuclei . 55

3.2 Physical conditions utilized in models for this work, based on TMC-1 conditions 56

3.3 Model identifiers with a listing of the active sputtering rate and whether cosmic ray heating was included 57

3.4 Parameters for nuclear sputtering calculations on amorphous solid water. 67

3.5 Parameters for calculating electronic sputtering terms on amorphous solid water. 69

3.6 Parameters for CO_2 sputtering cross section and yield calculations . . 70

3.7 List of observed column densities and estimated fractional abundances for examined COMs in TMC-1 methanol peak (MP) and cyanopolyyine peak (CP). Column densities are in cm^{-2}, while fractional abundances are with respect to hydrogen, and unitless. 83

3.8 List of modeled peak fractional abundances for select COMs, distinguished by model. 83

4.1 Table of examined species' binding energies, in kelvin 95

4.2 Initial abundances of elements with respect to total hydrogen nuclei . 97

4.3 Physical conditions utilized in models for this work, based on TMC-1 conditions 98

4.4 Parameters for nuclear sputtering calculations on amorphous solid water. 101

4.5 Parameters for calculating electronic sputtering terms on amorphous solid water. 102

4.6 Parameters for CO_2 sputtering cross section and yield calculations . . 103

4.7 List of G values for additional radiolysis reactions by type, with units of ionizations or excitations per 100 eV. New radiolysis reactions are displayed in Tables C.1 and C.2. G values are calculated via the Shingledecker-Herbst method, described in Shingledecker & Herbst (2018), and this work. 106

B.1 List of observed column densities in cm^{-2} for selected molecules toward B1-b, with a reported H_2 column density of 10^{23} cm^{-2} (Cernicharo et al., 2012). 154

B.2 List of observed column densities in cm^{-2} for selected molecules toward L483. All observed abundances are from Agúndez et al. (2019), and with a H_2 column density of approximately 4×10^{23} cm^{-2} 155

B.3 List of observed column densities in cm^{-2} for selected molecules toward L1989B. The reported H_2 column density is 4×10^{23} cm^{-2}. Methanol detection is from Bacmann & Faure (2015) and other abundances are from Bacmann et al. (2012). 155

B.4 List of observed column densities in cm^{-2} for selected molecules toward Barnard 5, H_2 column density of 10^{21} cm^{-2} (Taquet et al., 2017). . 155

C.1 Table of new suprathermal reactions of aromatic species discussed in Chapter 4. All reactions are for both surface ices and bulk ices. . . . 160

C.2 Table of new suprathermal reactions of nitrogen bearing species discussed in Chapter 4. All reactions are for both surface ices and bulk ices. 161

Chapter 1

Introduction

1.1 Astrochemical Background and History

In recent years, the number of detections of molecules in the interstellar medium has been increasing at an accelerating rate (McGuire, 2022). The first detection of a molecule in interstellar space using visual wavelength telescopes, was methylidine (CH) in 1937 Swings & Rosenfeld (1937). As radio telescopes improved, the complexity and number of molecules observed has exploded. Current speeds of detections can be partially attributed to the prevalence of radio telescopes, and even more recently, radio interferometers, such as ALMA, in diverse areas of the interstellar medium (Belloche et al., 2019). Perhaps of the most importance, is the detection of pre-biotic molecules in space, though some, like glycine, are contested (Hollis et al., 2000; Kuan et al., 2003; Belloche et al., 2008). These environments of studies are collectively referred to as the ISM, identified as specific objects in different stages throughout the stellar life cycle, shown in Figure 1.1, though there are other areas of space study not considered to be a part of the ISM.

There are multiple ongoing questions on the role of gaseous, dust surface, ice surface, and ice bulk chemistry in the formation of observed molecules. Both experiments and models suggest the importance of ices upon the grain surface in creating chemical complexity that has been observed in various regions of space. Even within the ISM,

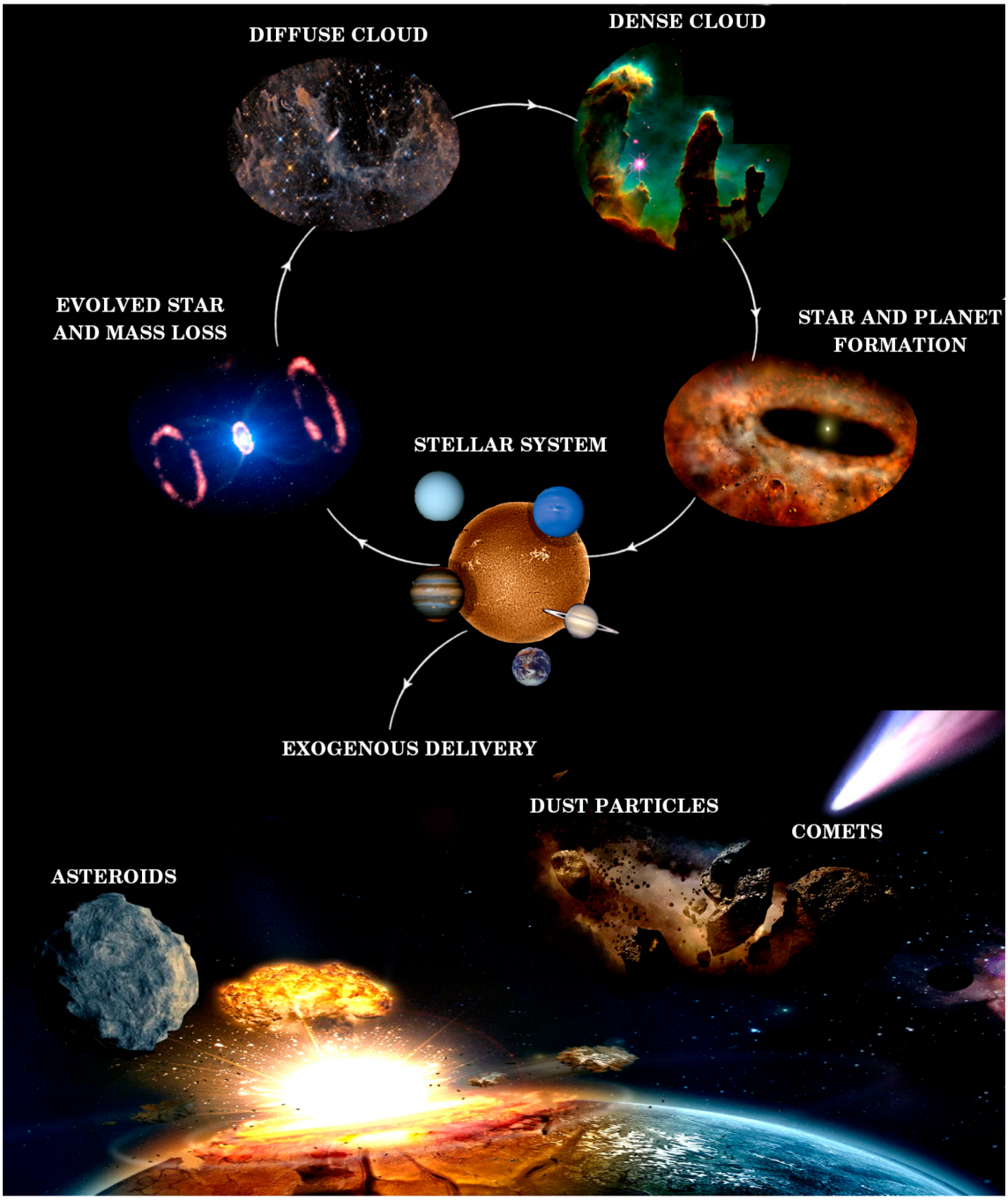

Figure 1.1: Simplified image of stellar life cycle, by G. A. Cruz Díaz, from NASA images

the conditions can vary widely in terms of temperature, density, irradiation rates of photons and cosmic rays, and resulting chemical abundance and diversity (Wakelam et al., 2012). The chemically rich areas are categorized into various stages based on stellar life cycles, and are shown in 1.1. These areas, formerly called nebula, have been replaced with more descriptive terms such as cold dark clouds, as "nebula" is a (for lack of a better word) nebulous term. What was considered a nebula now encompasses many different regions of space. A recent survey by McGuire (2022) neatly complies the current (as of early 2022) state of detections in the ISM, with over 220 molecules detected, notably the first Polycyclic Aromatic Hydrocarbons (PAHs).

We can "enter" the stellar life cycle with diffuse clouds, also called the cold neutral medium. These clouds are areas of slightly higher gas density of than the average ISM number density of 1 cm^{-3}. For comparison, earth's atmosphere at sea level has a density of approximately 10^{19} cm^{-3}. The low density of diffuse clouds are easily penetrated by the entire spectrum of photons, due to their low visual extinction, hence the name "diffuse". The high photon fluxes throughout the clouds allow for efficient photoionization of gases, and the majority of hydrogen, the most common element in the ISM, is found as protons. In addition to ionization, UV photons efficiently destroy many COMs found in diffuse clouds through photodissociation. As time progresses, the gas and dust present in diffuse clouds slowly accretes, and the cloud enters the stage known as a dense cloud. The dense cloud is the environment where the work in this thesis models, and will be discussed more later in the thesis.

Star forming regions, such as Sagittarius B2, are dense clouds that have passed another mass threshold, when the gas and dust begins to collapse into itself due to gravity, causing rotation and heating. These areas of the interstellar medium that are at the intersection between dense clouds and stars, have seen the most detections

of molecules in the different regions of the interstellar medium (McGuire, 2022). These areas were thought in the past to be the most chemically complex region of the interstellar medium, due to multiple factors. The first is that star forming regions have both a colder startup phase, where ice accrues on dust surfaces, and allows for efficient surface chemistry (Garrod et al., 2007). This is in addition to colder gas-phase chemistry, where efficient ion-molecule and neutral-neutral reactions drive gas phase chemistry (Herbst & van Dishoeck, 2009). This cold accretion phase is thought to have efficient surface reactions for generation of carbon bearing simple and complex organic molecules that remain stuck in the ice, due to a lack of thermal desorption (Garrod et al., 2007; Garrod, 2013). There is a focus on organic molecules to try and explain the origin of organic molecules on Earth, along with the production routes and origin of molecules that are necessary for carbon-based life found on Earth. Another factor is the subsequent collapse and warm up phases. As the gas and dust cloud gets large enough, over time, gravity causes the gas and dust to condense, forming an area of higher density gas and dust that is simultaneously warming up. This center of denser, warmer gas and dust eventually forms a star, but while still in the early stages is called a pre-stellar core. The increase in density and temperature allow for gas chemistry similar to earth temperatures to occur, at least up to approximately 300 K. There is another benefit: the heating of the dust grains sublimates the adsorbed ices, releasing the chemically rich ices into the gas phase, where it can be easily detected with rotational spectrosocopy.

In contrast to star forming regions, dense clouds, such as the cold dark cloud TMC-1, are star forming regions that have yet to start collapsing and heating up. Densities are higher than diffuse regions, generally on the order of 10000 per cubic centimeter, with temperatures ranging from 7 K to 20 K. At these temperatures, many thermal

processes, such as diffusion and desorption, are inefficient for most species apart from light atoms and diatomics (Minissale et al., 2013). Many reactions are also inefficient at low temperatures, due to the lack of free energy available to overcome reaction barriers. Low temperatures, coupled with comparatively low densities to terrestrial environments, present unique chemistry, as most chemistry studied is both in solution, as a liquid, and at higher temperatures. Despite these conditions seeming far removed from terrestrial chemistry, there is a history of complex molecule modeling in these environments, starting with the first chemical model of the interstellar medium (Herbst & Klemperer, 1973). From there, there have been multiple improvements in the modeling of chemistry in the interstellar medium, from the beginning of efficient gas phase neutral-neutral and ion-neutral reactions (Herbst & Klemperer, 1976; Herbst & van Dishoeck, 2009). As more mechanisms was included, and the number of molecules expanded, the chemistry of grain ices were included, particularly as a pathway for efficient hydrogenation of radicals (Hasegawa et al., 1992).

With recent detections of aromatic rings and PAHs toward TMC-1, more chemistry is needed to explain the ever-increasing number of complex molecules (McGuire et al., 2018, 2021; Burkhardt et al., 2021). Despite the challenges to theories of terrestrial chemistry that exist in cold dark clouds, the detections of complex molecules and prebiotic molecules in cold regions of the ISM suggest that there are still new pathways to explain the production of these molecules (Ioppolo et al., 2021). One such field, radiolysis chemistry, the chemical effects of bombardment by high energy particles, has already shown to increase COM formation on grain surfaces (Abplanalp et al., 2016; Shingledecker et al., 2018).

1.2 Cosmic Rays and Collisional Effects

One class of high energy particles that is the focus of the chemistry discussed in this thesis are cosmic rays. Produced by supernovae and by the massive black holes at galactic centers, cosmic rays are mostly composed of atomic nuclei without electrons, travelling at significant fractions of the speed of light (Blasi, 2013). Most cosmic rays (about 90%) are hydrogen nuclei, a single proton, while approximately 9% are helium nuclei, followed by the other 1%, composed of high atomic number and energy nuclei (Cummings et al., 2016). Figure 1.2, reproduced from Blasi (2013) shows the cosmic ray intensity plotted against energy, which is used to define the cosmic ray ionization rate, or ζ. In the gas phase, the ionization of hydrogen by cosmic rays has been shown to have significant impacts on the physical conditions of the ISM, as well as the the chemistry (Spitzer & Tomasko, 1968; Indriolo et al., 2009). Cosmic rays have also been found to penetrate entire interstellar clouds (Cesarsky & Volk, 1978). Until Shingledecker et al. (2018) the majority of cosmic ray driven chemistry was in the gas phase, through ionization of H_2, and dissociation of gases (Herbst & Klemperer, 1973).

When an incident ion, also called the primary, strikes atoms along the ion's path, called the "target", there are physical and chemical effects that happen on multiple timescales: The fastest, on the order of 10^{-13} s, is the transfer of energy, caused by discrete collisions of two types: nuclear collisions, caused by interactions between the nuclei of atoms, result in energy transfer to the nucleus of the target, and electronic collisions, caused by interactions from charges and fields, result in energy transferring to the electrons of the target. Nuclear collisions, also called elastic collisions, cause atomic motion, often as heat, or enough motion to cause atoms or entire molecules

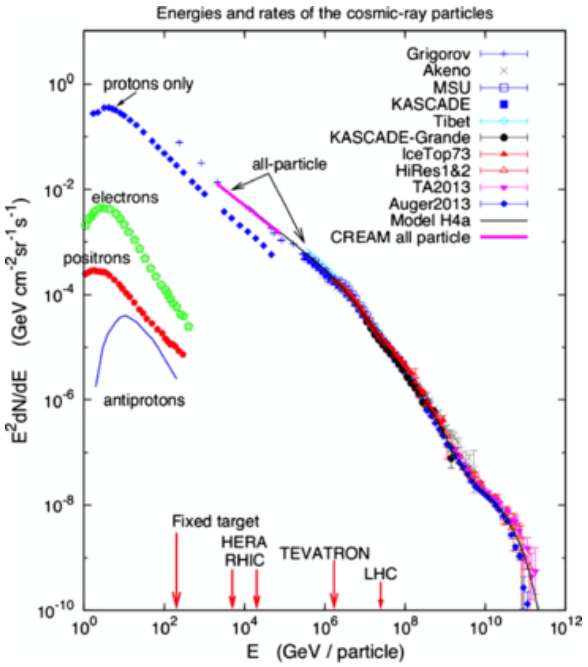

Figure 1.2: Image of Cosmic ray intensities against energy from multiple studies. Reproduced from (Blasi, 2013)

.

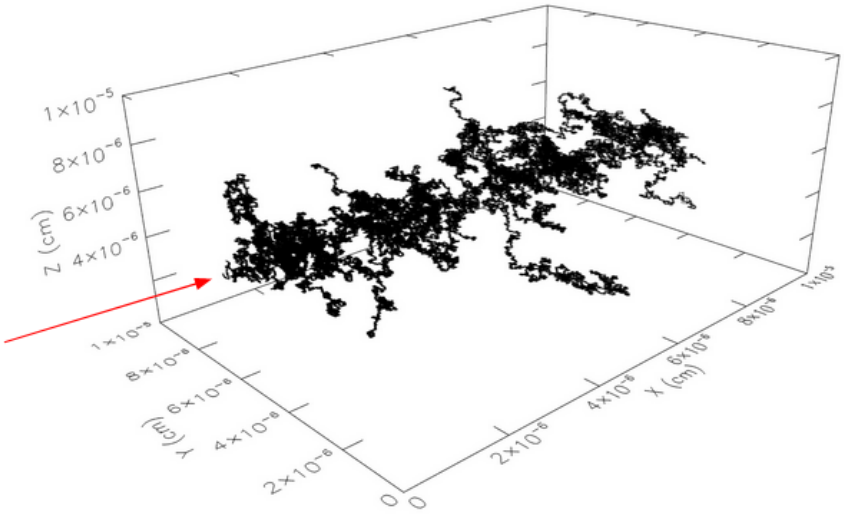

Figure 1.3: Modeled path of secondary electrons in water ice, with data from (Shingledecker et al., 2017). The initial path of the primary cosmic ray is in red, while secondary electrons are in black.

from the surface to be ejected. The process of target particles leaving a surface after energetic particle bombardment is called sputtering (Behrisch & Eckstein, 2007). Sputtering may be important in the interstellar medium because of the number of COMs that form on grain surfaces that are unable to thermally desorb, remaining stuck on and within dust grain ices (Iqbal & Wakelam, 2018). Electronic collisions in this case, cause ionizations and excitations in the target solids (Shingledecker et al., 2017). Ionized electrons are then free to collide with other members on the ice, causing further ionizations and excitations. Electrons that are high enough in energy to cause further ionizations and excitations from the primary track are called secondary electrons, and are important in energy transfer throughout solids (Platzman, 1955; Arumainayagam et al., 2019). An image of the modeled path of a primary ion in red, and secondary electrons generated, in black, is shown in Figure 1.3. Energy transfer can generally be split by collisional type, and the total energy loss of some particle per unit area can be expressed as

$$-\frac{dE}{dx} \approx n_{\mathrm{B}}(S_{\mathrm{n}} + S_{\mathrm{e}}) \tag{1.1}$$

where n_{B} is the number density of the target, and S_{n} and S_{e} are the nuclear and electronic stopping power cross sections (also just called stopping power), respectively. The electronic stopping power can be estimated at relevant cosmic ray energies in the form of the Bethe equation (Bethe, 1932)

$$S_{\mathrm{e}} \approx \frac{4\pi Z_{\mathrm{x}}^2 Z_{\mathrm{y}} e^4}{m_{\mathrm{e}}\nu^2}\left[\ln\left(\frac{2m_{\mathrm{e}}\nu^2}{E_{ion}}\right) - 1 - \frac{C}{Z_{\mathrm{y}}}\right] \tag{1.2}$$

where e is the fundamental charge, m_{e} is the electron mass, ν is the velocity of the

primary, Z are the atomic numbers of the target ($Z_{\rm x}$), and the primary ($Z_{\rm y}$), and $E_{\rm ion}$ is the energy required to ionize the target. C is the speed of light. The nuclear stopping power can be numerically calculated using the form described in Johnson (1990),

$$S_{\rm n} = \frac{\gamma E_{\rm y}}{2}\sigma_d \tag{1.3}$$

where $E_{\rm y}$ is the energy of the incident ion, $\sigma_{\rm d}$ is the diffusion or momentum transfer cross section (Johnson, 1982; Banks & Kockarts, 1973), and γ is the mass factor, given as $4M_{\rm x}M_{\rm y}/(M_{\rm y} + M_{\rm y})^2$, where M is the mass of the primary ($M_{\rm y}$) and the target ($M_{\rm x}$). Nuclear stopping powers at cosmic ray energies are often orders of magnitude less than electronic stopping powers due to near-relativistic speeds and quantum effects, and will be discussed later.

After the collisional transfer of energy is the physio-chemical stage, at approximately 10^{-11} s. This is when ionized species recombine, either cations with anions, or cations with electrons. This stage is important to radiolysis chemistry as this stage produces the electronically excited suprathermal species through recombination in the situation where ionization occurs instead of direct excitation. Following the physio-chemical stage is the luminescence stage, so named for the timescale of molecules that can emit photons when electronically excited to relax, on the order of 10^{-9} s. In later chapters, this phase is where the electronically excited molecules are quenched, not by photon emission, but either react, or relax through surface motion. The final stage is the chemical stage, or all events that happen on timescales slower than 10^{-6} s, all the way up to the chemistry in clouds that occur over millions of years. In this timescale, energetic reactions are less likely to occur, these timescales are for surface reactions

guided by diffusion at low temperatures, or other thermal mechanisms in the gas phase that are the backbone of the chemical network used in models.

1.3 Rate-Equation Based Models

> "Essentially, all models are wrong, but some are useful."
> - George E. P. Box (Box & Draper, 1987)
> "...So since all models are wrong, it is very important to know what to worry about; or to put it another way, what models are likely to produce procedures in practice (where exact assumptions are never true)"
> - George E. P. Box (Box et al., 2009)

If there are chemical reactions that can happen over the course of multiple years, there needs to be a time efficient way to study them. There are two commonly used chemical model types: stochastic Monte Carlo models , based on random number generation to produce slightly different results each time (Chuang et al., 2016), and deterministic models that solve systems of equations (Herbst & Klemperer, 1973; Wakelam et al., 2012). This work utilized the latter to better explain long term chemical evolution of cold dark clouds to be directly compared to observations, by expanding upon already existing chemical networks and adding new processes to the model.

Rate-equation based models are able to cover chemical evolution over thousands of years faster than Monte Carlo methods due to computational efficiency. Computationally, solving a system of equations is dependant on the number of equations, or in the case of our model, the number of astrochemical species that are included. In contrast, a Monte Carlo model generates a random number to decide which singular

species will be called upon. The model then solves what that species will do, but does so by progressing time slightly forward. This is inefficient because the tracking of a single species' process cannot be spread across multiple computational units, called parallelization. While this is incredibly useful for modeling microscopic effects on a singular grain, the ratio of hydrogen to other molecules means that hydrogen is the dominating moving part of the model, even artificially lowering the rate that hydrogen is called upon in the model still carries a high computational cost. That is not to say Monte Carlo models are not useful, as they provide insight to the state of microscopic grain systems (van Dishoeck & Black, 1988).

A simplistic, general rate equation for the change in gas-phase abundance for a single species, i, can be described as the sum of all the reactions producing and destroying species i. The complexity comes from all of the ways that the abundance of i can be changed that the model accounts for: through bimolecular reactions of two other species, j and l, through unimolecular destruction routes that only involve i and some other non-chemical phenomena, like photoionization or dissociation, and through interaction with grain ices, can be combined into a single rate equation

$$\frac{dn(i)}{dt} = \sum_j \sum_l k_{jl} n(j) n(l) - n(i) \sum_j k_{ij} n(j) \pm \sum k_{grain} n_s(i) \tag{1.4}$$

where $n(i, j, l)$ represents the concentration of a species, i,j,or l. k represents the rate constant of the unimolecular processes k_j, bimolecular processes k_{jl}, or in the case of the far right term $\sum k_{grain} n_s(i)$ the sum of all adsorption and desorption processes that depend on the by the concentration of species i on the surface, written generally as $n_s(i)$. The addition of grain chemistry to rate-equation models makes the model more complex; where a gas-phase only model only depends on the coupled

concentrations of gas species, including a grain portion practically doubles the coupled rate equations, creating coupled rate equations for all surface species. In the case of a three-phase model (the three phases being gas, surface ices, and bulk ices), the number of species being considered can triple, as a distinction is made between "surface" species that are at the border between the gas and ice, and the remainder of the ice that does not have access to the gas, called the bulk. However, the inclusion of grains allows for an expansion of chemistry, and is an important route for COM formation (Hasegawa et al., 1992; Garrod et al., 2008; Ioppolo et al., 2021).

Another aspect of complexity of rate-equation based models is a side effect of their efficiency. In contrast with how Monte Carlo models progress through one molecule at a time, rate equation models results are averaged over time. To give a relevant example, processes that happen a discrete number of times, but have large impacts, such as a heavy cosmic ray hitting a dust grain, have the results averaged over time. To further clarify, the way our model treats a heavy cosmic ray hitting a grain is not mimicking the number of grains and the cosmic ray that will hit the grains, it takes a weighted average of the energy of the cosmic rays and applies that to all grains within a period of time. The period of time itself varies, as the time modeled increase with each time step of the model. For example, a model may run 500 time steps until it is finished. The first time step models a tenth of a year, while one of the last time steps will model 10^6 years. While the difference in time step is accounted for, as most processes used in the model happen more frequently than once every million years, this inherently spreads out less frequent events over the time step period during the model. This makes our model inherently wrong, hence the quote at the start of this chapter. The model loses the specifics of different cosmic rays and different grains. For events that happen frequently, like diffusion of hydrogen on surfaces, or certain

gas-phase reactions, there is not a significant problem, as the possible results have a lesser effect overall, and the range of possibilities are covered by the average as events happen. For infrequent events, such as those which occur on the order of hundreds of years, rate-equation based models treat the events as slower, continuous events happening over long time periods, which lessens the intensity by spreading effects over longer periods of time than what is physical. This is a weakness that we must be conscious of and try to account for, however, with the far more frequent hydrogen cosmic rays, occurring multiple times per second per square meter (Blasi, 2013), this is mostly a problem for early model times, which are inaccurate with regards to chemistry for the same reason. All of this is to say that cosmic rays and their effect on interstellar chemistry can be modeled using rate equations.

1.4 Scope of Thesis

This thesis is focused on modeling interactions between cosmic rays and interstellar grain ices, and the effects of these interactions on species throughout the interstellar medium. A theme is the effects of nonthermal desorption methods that enhance gas-phase abundances of detected interstellar molecules through reactive desorption through quick reactions of electronically excited suprathermal species and sputtering.

Chapter 2 considers the effects of binding energies and radiolysis chemistry on three $C_2H_4O_2$ isomers that have been detected in warmer regions of the ISM, such as star forming regions. The main idea of the chapter is that radiolysis chemistry in cold cores may be able to expand chemical diversity through efficient reactions, and efficient nonthermal desorption when the molecules in question are made on the grain surface. We also show that increasing the abundance on the grain surface is possible,

even when including radiolysis reactions destroying the complex molecules we are trying to create.

Chapter 3 presents a theoretical method for including sputtering reactions in rate-equation based astrochemical models. Where the effectiveness of radiolysis chemistry is dependent on varying factors for individual species, notably binding energy and actual reaction pathways needing to be included, sputtering is shown to be a less specific desorption method, as there is a possibility of multiple molecules being sputtered from the surface at the same time. In this chapter, we also explain the physics of sputtering, and examine a broad number of simple molecules across the three phases, while considering how effective is sputtering when limiting other thermal desorption methods.

In Chapter 4, we combine the enhancements of radiolysis chemistry and sputtering to address their role in the formation of polycyclic aromatic hydrocarbons and a sample of detected precursors in TMC-1. We address the viability of a bottom up approach for the formation of PAHs, and show that sputtering and radiolysis enhance gas-phase abundances of most species examined, while at the same time, not replicating observed abundances of some molecules. We also discuss the included thermal pathways to the examined molecules, and possible future directions of modeling to address shortcomings that may become more common when dealing with PAHs.

Finally, Chapter 5 summarizes the results presented in this work, and suggestions for the improvement of radiolysis chemistry and sputtering. Two examples are the implementation of Bragg's law for obtaining species-specific cross sections, and discussions about cosmic ray processing of the physical structure of ices and the effect of heavy cosmic rays on sputtering and radiolysis.

Chapter 2

Radiolysis of $C_2H_4O_2$ isomers and Dimethyl Ether in Cold Dark Clouds

Complex organic molecules (COMs) have been detected in a variety of interstellar sources. The abundances of these COMs in warming sources can be explained by syntheses linked to increasing temperatures and densities, allowing quasi-thermal chemical reactions to occur rapidly enough to produce observable amounts of COMs, both in the gas phase, and upon dust grain ice mantles. The COMs produced on grains then become gaseous as the temperature increases sufficiently to allow their thermal desorption. The recent observation of gaseous COMs in cold sources has not been fully explained by these gas-phase and dust grain production routes. Radiolysis chemistry is a possible non-thermal method of producing COMs in cold dark clouds. This new method greatly increases the modeled abundance of selected COMs upon the ice surface and within the ice mantle due to excitation and ionization events from cosmic ray bombardment. We examine the effect of radiolysis on three $C_2H_4O_2$ isomers – methyl formate ($HCOOCH_3$), glycolaldehyde ($HCOCH_2OH$), and acetic acid (CH_3COOH)

– and a chemically similar molecule, dimethyl ether (CH_3OCH_3), in cold dark clouds. We then compare our modeled gaseous abundances with observed abundances in TMC-1, L1689B, and B1-b. [1]

2.1 Introduction

The isomers of $C_2H_4O_2$ – methyl formate ($HCOOCH_3$), glycolaldehyde ($HCOCH_2OH$), and acetic acid (CH_3COOH) – are all important chemical components of the interstellar medium. First detected by Brown et al. (1975) toward Sgr B2N, methyl formate, the most abundant of the three commonly occurring $C_2H_4O_2$ isomers, has been detected toward warm sources, such as Sgr B2N and Orion A, and cold molecular clouds, such as TMC-1 and L1544 (Brown et al., 1975; Ellder et al., 1980; Jiménez-Serra et al., 2016; Soma et al., 2018). Soma et al. (2018) determined the column density of methyl formate toward TMC-1 to be $(1.5 \pm 0.1) \times 10^{12}$ cm^{-2}. This column density, along with the estimated molecular hydrogen column density of 10^{22} cm^{-2} yields a fractional abundance of approximately 1.5×10^{-10}. Abundances of methyl formate toward L1689B and B1-b have been reported as 7.4×10^{-10}, and 2.0×10^{-11}, respectively (Bacmann et al., 2012; Cernicharo et al., 2012).

As far as we know, both acetic acid and glycolaldehyde have yet to be detected toward cold molecular clouds, although both have been observed toward Sgr B2N (Remijan et al., 2002, 2003, 2004), among other warm molecular clouds and star-forming regions. Indeed, glycolaldehyde was first detected toward Sgr B2N by Hollis et al. (2000), while acetaldehyde was first detected in Sgr B2, Orion KL, and W51 by Mehringer et al. (1997). Glycolaldehyde is a sugar-related molecule (Carroll et al.,

[1] Originally published as Paulive et al. (2021)

2010) that might serve as a precursor to the kinds of true sugars, such as ribose and deoxyribose, that are critical constituent molecules in RNA and DNA, respectively. Acetic acid is a simple carboxylic acid, with a common functional group in biologically relevant compounds, and an amine group distant from the simplest amino acid, glycine. Another molecule that we will consider in the chapter is dimethyl ether. While not an isomer of $C_2H_4O_2$, it has been shown to share spatial abundance with methyl formate in areas of the ISM (Taquet et al., 2017; Soma et al., 2018).

The synthesis of COMs in warming sources in the interstellar medium is generally well understood, principally by efficient diffusion processes of radicals produced on grain surfaces by photodissociation, but also by gas-phase reactions. The surface radicals combine to form COMs and other species, which, at still higher temperatures, desorb thermally into the gas where they are detected. The granular synthesis is not thermally active, however, at temperatures below 20 K, since radicals - with the exception of light species such as atomic hydrogen - cannot diffuse rapidly enough to react. A number of other approaches to the synthesis of COMs in cold regions have been reported in the literature. These include both gas-phase chemistry, grain surface chemistry, and combinations of the two (Chang & Herbst, 2016; Vasyunin & Herbst, 2013a; Balucani et al., 2015). The grain surface routes require some non-thermal mechanism to desorb molecules at low temperatures. The major desorption processes considered include reactive desorption, photo-desorption, and cosmic ray-induced desorption via heating and sputtering, most of which are only understood at a semi-quantitative level. (Garrod et al., 2007; Hasegawa & Herbst, 1993; Öberg et al., 2009; Kalvāns & Kalnin, 2019).

There are a variety of low-temperature methods for producing COMs on grains prior to non-thermal desorption into the gas. While diffusive (Langmuir-Hinshelewood)

grain reactions at low temperatures tend to be inefficient unless one of the reactants is an atom or diatomic molecule, non-diffusive processes do exist (Hasegawa & Herbst, 1993). One such mechanism is the Eley-Rideal mechanism, in which species from the gas phase directly react with surface molecules (Ruaud et al., 2015). This process can be efficient if there are sufficient reactive species on the grain surface and if the reactions do not possess activation energy. Another non-diffusive mechanism is the hot atom mechanism, in which energized granular species with enough energy to overcome diffusion barriers travel swiftly around sites on the surface until all excess energy is lost to the surface itself, or they react.

In addition to their effect on desorption, cosmic rays can induce a non-thermal chemistry as they bombard and travel through grain mantles, initially producing reactive secondary electrons. The non-thermal chemistry, known as radiolysis, has been studied experimentally by a number of groups, who utilize either energetic protons or electrons to bombard low temperature ices and produce many molecules including COMs (Abplanalp et al., 2016; Rothard et al., 2017; Boyer et al., 2016). This cosmic-ray induced chemistry was recently studied theoretically by Shingledecker & Herbst (2018), Shingledecker et al. (2019a), and Shingledecker et al. (2018) who developed and expanded upon the idea that cosmic rays can cause ionization and excitation within the ice surface and mantle, thereby generating short-lived "suprathermal species" - a term for electronically excited molecules. These molecules can react with nearest neighbors either on the ice surface, or within the bulk ice, overcoming large reaction barriers, a constraint that makes thermal reactions with barriers typically slow at temperatures under 20 K. These "suprathermal" species either react or are quenched, and have been shown to enhance the abundances of certain species in low temperature sources, including methyl formate (Shingledecker et al., 2018). Under some circumstances,

photodissociation of molecules on ices to form reactive radicals can be a competitive mechanism (Jin & Garrod, 2020).

In this chapter, we use the approach undertaken previously by Shingledecker et al. (2018) to study the abundances of the three isomers and dimethyl ether with and without radiolysis in cold sources. We compare our results with observed abundances for methyl formate and dimethyl ether in TMC-1, L1544, L1689, and B1-b, and predict abundances for those species not yet observed. We also study why radiolysis can enhance the abundance of some COMs in low temperature sources such as the three isomers studied and have smaller to nil effects on others, such as dimethyl ether. In Section 2.2, we discuss our model, while in Section 2.3 our results are shown. The astrochemical implications are explained in Section 2.4, while Section 2.5 contains our conclusions.

2.2 Model

2.2.1 Nautilus

The chemical simulations reported in this chapter use the three-phase rate equation-based gas-grain code `Nautilus-1.1` (Ruaud et al., 2016). A three-phase model is one which distinguishes species upon the surface of the grain ice (two monolayers in this case) from the remaining bulk. This distinction is relevant to diffusive chemistry, reactive desorption, and other desorption mechanisms that drive COMs from the surface into the surrounding gas, where they are more easily observed. In addition to the base `Nautilus-1.1` program, other features have been added to allow for the inclusion of radiolysis and suprathermal chemistry, as described in Shingledecker

& Herbst (2018). Radiolysis chemistry will be further described in Section 2.2.3. The chosen initial abundances are displayed in Table 2.1, with relevant constant and homogeneous physical conditions in Table 2.2. Relevant to later sections is the cosmic ray ionization rate (ζ), $1.3 \times 10^{-17} s^{-1}$. Table 2.3 lists the binding energies on water ice for $C_2H_4O_2$ isomers and dimethyl ether. The design of the `Nautilus` program allows the user to enable or disable a variety of mechanisms related to gas- and grain-processes (Ruaud et al., 2016). These mechanisms and their status in this study are itemized in Table S4 of the supplementary material, entitled Nautilus Switches.

In addition to the switches listed in supplementary Table S4, others have been added to update `Nautilus` with more options. A competitive tunneling mechanism for diffusive species, labelled "Modified_tunneling" is described in Herbst & Millar (2008). This choice is set to the faster option. The option "Only_light_tunnel" prevents all species but H and H_2 from tunneling under activation energy barriers of surface reactions, and is set to "on" (Shingledecker et al., 2019a). There are switches regarding nonthermal desorption mechanisms for surface species. These include reactive desorption at 1 per cent probability (Garrod et al., 2007), photodesorption (Bertin et al., 2013), and cosmic ray induced photodesorption (Hasegawa & Herbst, 1993). These three switches are set to "on", with the photodesorption yield set at 1×10^{-4}.

2.2.2 Network

The `Nautilus` reaction network used in this study has been expanded to include more complex chemical species and intermediates that lead up to $C_2H_4O_2$ isomers, as well as dimethyl ether. The base network of gaseous reactions is taken from the KIDA network (Wakelam et al., 2012). The granular reaction network is from the

Table 2.1: Initial abundances of elements with respect to total hydrogen nuclei

Species	Abundance
H_2[a]	0.499
He[a]	9.000×10^{-2}
N[a]	6.200×10^{-5}
C[b]	1.700×10^{-4}
O[c]	2.429×10^{-4}
S[d]	8.000×10^{-8}
Na[d]	2.000×10^{-9}
Mg[d]	7.000×10^{-9}
Si[d]	8.000×10^{-9}
P[d]	2.000×10^{-10}
Cl[d]	1.000×10^{-9}
Fe[d]	3.000×10^{-9}
F[e]	6.680×10^{-9}

[a] (Wakelam & Herbst, 2008)
[b] (Jenkins, 2009)
[c] (McGuire et al., 2018)
[d] (Graedel & McGill, 1982)
[e] (Neufeld et al., 2005)

Table 2.2: Physical conditions for TMC-1 utilized

Parameter	TMC-1
n_{H} (cm^{-3})	10^4
n_{dust} (cm^{-3})	1.8×10^{-8}
T_{gas} (K)	10
T_{dust} (K)	10
N_{site} (cm^{-2})	1.5×10^{15}
ζ (s^{-1})	1.3×10^{-17}

Table 2.3: Binding Energies

Species	E_b (K)
$JHCOOCH_3$	5200^a
$JHCOCH_2OH$	6680^a
JCH_3COOH	6300^a
JCH_3OCH_3	3675^a

a (Garrod, 2013)

`Nautilus` package, with additional thermal grain-surface reaction pathways leading to $C_2H_4O_2$ isomer precursors from Garrod & Herbst (2006). Used initially in hot core models, these reactions have been included here to provide likely thermal pathways to COMs in competition with radiolysis. Other notable additions include new gas-phase reactions for acetic acid and glycolaldehyde from Skouteris et al. (2018). The full list of additional reactions is contained in the supplementary material, Tables S1 S2, and S3 (available online), with important reactions discussed in Sections 2.3.1, 2.3.3, and 2.3.2. Species with the first letter "J" are those on the surface of the ice mantle, while species with a "K" lie within the bulk of the ice, which, after the simulation has completed running (10^7 yrs), contains close to 100 monolayers of ice. Additional binding energies $E_{\rm D}$ for the four principal molecules studied were taken from Garrod (2013) and are listed in Table 2.3. The diffusion barriers ($E_{\rm b}$) for all granular species are $0.4 \times E_{\rm D}$ for ice surface species, and $0.8 \times E_{\rm D}$ for bulk species.

2.2.3 Radiolysis

The method used for radiolysis was first developed by Shingledecker & Herbst (2018). It describes four different results that follow an incoming cosmic ray or secondary electron interacting initially with a target species A, for which we use a "$\rightsquigarrow$". The subsequent results can be described by the following equations, which represent dif-

ferent paths to ions and suprathermal neutrals, the latter denoted with an asterisk:

$$\mathrm{A} \rightsquigarrow \mathrm{A}^+ + \mathrm{e}^- \tag{2.1}$$

$$\mathrm{A} \rightsquigarrow \mathrm{A}^+ + \mathrm{e}^- \rightarrow \mathrm{A}^* \rightarrow \mathrm{B}^* + \mathrm{C}^* \tag{2.2}$$

$$\mathrm{A} \rightsquigarrow \mathrm{A}^* \rightarrow \mathrm{B} + \mathrm{C} \tag{2.3}$$

$$\mathrm{A} \rightsquigarrow \mathrm{A}^* \tag{2.4}$$

The first process leads to the ionisation of A, while the second process describes the formation of suprathermal fragments B and C with an intermediate suprathermal A formed via dissociative recombination of the A ion. The third process describes the direct formation of an intermediate suprathermal species followed by its fragmentation into non-excited products, while the last process describes the formation of suprathermal A, which does not subsequently fragment.

In order to implement both generation of suprathermal species, and fast suprathermal reactions into the rate-equation based model used, we can derive a pseudo first-order rate coefficient by multiplying a cross section (σ_e), in cm^2, with a cosmic ray flux (ϕ) ,in cm^{-2} s^{-1}. In order to obtain a cross section, we start with a stopping power cross section $S(E)$, which is defined through the loss of kinetic energy of a projectile with distance and is in units of eV cm^2. It can be calculated using the Bethe equation (Bethe, 1932; Johnson, 1990):

$$S_e(E) = \frac{4\pi Z_x Z_y e^4}{m_e \nu^2} \left[\ln \left(\frac{2 m_e \nu^2}{E_{ion}} \right) - 1 - \frac{C}{Z_y} \right] \tag{2.5}$$

where Z_x and Z_y are the atomic numbers of the target species, and the incoming particle, respectively, e is the charge of an electron, m_e is electron mass, and v is the velocity of the incoming particle. The equation refers to the electronic stopping cross section, which is the energy lost per unit area for inelastic collisions with electrons, or cosmic ray protons. At cosmic ray energies, nuclear stopping cross sections are multiple orders of magnitude lower compared with electronic stopping cross sections; therefore, inelastic electron collisions dominate. These electronic stopping cross sections can be easily calculated using the online program `PSTAR`, which uses the Bethe equation for particles at high energies, and fits to experimental data for lower energy particles (Berger et al., 1999).

From an electronic stopping cross section, we can then approximate an electronic cross section by dividing S by the average energy loss per ionization for an inelastic collision ($\bar{W}$). The average energy lost is a sum of all the processes that can result from the inelastic collisions of cosmic rays or secondary electrons with the target. These processes include the energy lost to excitation ($\bar{W_{exc}}$), the energy loss from the generation of secondary electrons ($\bar{W_s}$), and the ionization energy (E_{ion}), which is the average energy loss of ionization ($\bar{W_{ion}}$) minus the energy of the ionized electron (ϵ). Thus, the total average energy lost per ionization due to inelastic collisions can be defined as follows:

$$\bar{W} = E_{ion} + \xi \bar{W_{exc}} + \bar{W_s} \tag{2.6}$$

where ξ is the average number of excitations per ionization. The value for $\bar{W}$ is approximately 27 eV for water, but can range from 60 eV at low energy collisions to 20 eV for high energy collisions above 100 eV (Dalgarno et al., 1958), and will be similar for most other molecules present in interstellar ices. For this reason, along with lack of measured values for other molecules, the average energy loss is estimated to be that of water for all reactions.

The other factor needed to calculate the quasi-first-order rate coefficient is the cosmic ray flux. We use the Spitzer & Tomasko (1968) cosmic ray distribution, integrated over their cosmic ray energy range, which Shingledecker & Herbst (2018) calculated to result in a flux (ϕ_{st}) of 8.6 particles cm^{-2} s^{-1}. Shingledecker & Herbst (2018) also introduced a scaling factor, ζ, (with units of inverse seconds), based on the cosmic ray ionization rate of hydrogen, in order to easily adapt models to areas of higher or lower cosmic ray bombardment rates. Our overall flux is then:

$$\phi = \phi_{st} \frac{\zeta}{10^{-17}} \tag{2.7}$$

The product of ϕ and σ_e yields the needed quasi-first-order rate coefficient:

$$k = \sigma_e \phi = \frac{S_e}{\bar{W}} \phi_{st} \frac{\zeta}{10^{-17}} \tag{2.8}$$

This resulting rate coefficient must be further separated into specific rate coefficients for Reaction 2.1, 2.2, 2.3, and 2.4. However, we assume the probability of Reaction 2.1 to be 0, as the resulting electron will either immediately recombine, or be high enough in energy to be a reactive secondary electron. Therefore, the network does not take into account reactions similar to Reaction 2.1. The resulting reactions

that are included in the chemical network, Reactions 2.2, 2.3, and 2.4 are referred to in Shingledecker et al. (2018) as Type I, II, and III reactions, respectively.

In order to account for the differences in rates for the different ionizations or excitations, it is helpful to use the G value, which is simply a measure of the extent of a process occurring with an input of 100 eV from the cosmic ray or secondary electron. G values can be used instead of the specific average energy loss, as shown in Equation 2.9:

$$G = \frac{100eV}{\bar{W}}. \tag{2.9}$$

We can estimate G values from ionization energies and average energy loss to excitation using the Shingledecker-Herbst method. (Shingledecker & Herbst, 2018). This substitution results in the final form of our equation used to obtain pseudo-first order rate coefficients for the formation of suprathermal species.

$$k_{\mathrm{n}} = S_e \left(\frac{G_{\mathrm{n}}}{100eV} \right) \phi_{ST} \left(\frac{\zeta}{10^{-17}} \right). \tag{2.10}$$

The W values for excitation and ionization plus the ionization energies E_{ion} used to obtain G values are shown in Table 2.4. The G values for reaction types I, II, and III for the COMs studied in the chapter are shown in Table 2.5.

The suprathermal species rate coefficients are then added to the network. The result of the inclusion of suprathermal species is multifaceted. By the generation of suprathermal species, the model has access to nearly instantaneous reactions that easily surmount activation energy barriers. In addition to this effect, the speed of these reactions is also enhanced because they occur between a suprathermal species

Table 2.4: Parameters used to estimate G values.

Species	E^a_{ion} (eV)	W^b_{exc} (eV)	W_s (eV)
$HCOOCH_3$	10.84	5.390	3.636
$HCOCH_2OH$	10.86	4.132	3.639
CH_3COOH	10.65	6.199	3.614
CH_3CHO	10.23	4.025	3.563
HCO	8.12	2.017	3.256

[a] (Lias et al., 2020)
[b] (Keller-Rudek et al., 2013)

Table 2.5: Estimated G values (extent per 100 eV)

Species	G_I	G_{II}	G_{III}
$HCOOCH_3$	3.704	4.305	4.305
$HCOCH_2OH$	3.704	5.603	5.603
CH_3COOH	3.704	3.804	3.804
CH_3CHO	3.704	6.076	6.076
HCO	3.704	14.345	14.345

and its adjacent neighbors, negating often slow diffusion processes. Another outcome of a suprathermal species is quenching. In this process, the energy of the excited suprathermal species is vibrationally lost to the surface of the grain. The lifetime of the suprathermal species is not long enough for diffusive reactions to occur, so rapid reactions with an adjacent neighbor or quenching can remove the excess energy of the suprathermal species. These two processes happen independently of each other, so that the rate of destruction for suprathermal species is the sum of the rates of fast reactions and quenching. Equations for the rates of both rapid processes are given in Shingledecker et al. (2018). Despite this fast quenching process, the existence of suprathermal reactions often allows new routes to COMs to be enabled, even at low temperatures.

2.3 Results and Analysis

In our calculations, we have utilized two low temperature models, numbered 1 and 2. Model 1 does not contain radiolysis chemistry, and results with this model will be represented by solid lines in figures. Model 2 includes radiolysis chemistry, resulting in the generation of suprathermal species. Results with this model are shown in figures with dashed lines. Both models utilize the same set of choices regarding `Nautilus` switches, except for the switch that enables radiolysis. The models likewise share the same initial abundances and physical parameters.

New sets of reactions have been included in both of our models. New radiolysis reactions have been included to Model 2, which can increase the production of suprathermal species. Notable in Model 2 are not just the new suprathermal reactions that quickly produce the major molecules in our study, but also additional such reactions that destroy these molecules, which must be closely examined. Without these reactions, it is possible to overproduce the COMs we are studying in a non-physical manner. Model 1 includes the new thermal production and destruction reactions that are relevant to the species examined here that are also in Model 2.

In the modifications we have made to the networks, notable reactions include all production and destruction reactions involving acetic acid and glycolaldehyde on grains, as there are no reactions , thermal or suprathermal, that are included in the standard reaction network used. For example, in Model 2, we have included suprathermal hydrogen abstraction reactions that reduce double bonded oxygen atoms to hydroxy (-OH) groups. These reactions destroy acetic acid and glycolaldehyde. and generate suprathermal species. Also included are other new rapid reactions involving suprathermal species. However, the destruction reactions of more complex species,

not only for glycolaldehyde and acetic acid, have not been examined sufficiently, as most efforts to examine them have been focused on production routes. A detailed consideration of such destruction pathways have been found to be useful in previous investigations of families of isomers (Shingledecker et al., 2019b; Shingledecker, Molpeceres, Rivilla, Majumdar & Kästner, Shingledecker et al.), however such a study is beyond the scope of this work. Additionally, although methyl formate and dimethyl ether are both included in the base KIDA gas-phase network, glycolaldehyde and acetic acid are not, meaning there are very few thermal gas phase routes leading to their formation, and even fewer destruction reactions involving them, both in the gas phase and solid phase of the ice on the dust grains. This paucity of reactions must be eliminated.

2.3.1 Methyl Formate

In warmer environments, the main method of producing methyl formate is likely through a series of diffusive grain surface reactions (Laas et al., 2011). The final reaction in the chain is:

$$\mathrm{JHCO} + \mathrm{JCH_3O} \rightarrow \mathrm{HCOOCH_3}, \tag{2.11}$$

after which the methyl formate product is subsequently desorbed from the grain surface once the temperature reaches $\approx$ 100 K. At lower temperatures, desorption occurs mainly through the exothermicity of the reaction 1 per cent of the time. A series of gas phase reactions also leads to gaseous methyl formate with the final reaction involving atomic oxygen and a radical (Balucani et al., 2015):

$$CH_3OCH_2 + O \rightarrow HCOOCH_3 + H, \tag{2.12}$$

although the role of this reaction has mainly been studied at low temperatures.

Although the abundance of methyl formate in warm regions is reproduced satisfactorily by the approach of thermal diffusion reactions followed by thermal desorption, the situation is quite different at temperatures below 20 K. In addition to the difficulty of producing the molecule on grains, desorption can only occur by non-thermal means, such as reactive desorption. At these temperatures, methyl formate has been detected toward various sources with cold and pre-stellar cores, with approximate fractional abundances with respect to hydrogen of 7.4×10^{-10}) toward L1689B, 1.5×10^{-10} toward TMC-1, and 2.0×10^{-11} toward B1-b (Bacmann et al., 2012; Cernicharo et al., 2012; Soma et al., 2018) .

Let us first consider how the results of our non-radiolysis model (Model 1) compare with these observations. As shown in Figure 2.1, the predicted peak fractional abundance of gaseous methyl formate is only 7.5×10^{-13} at $\approx 3 \times 10^5$ yr whereas the observed value in B1-b is still a factor of 30 higher, that in TMC-1 a factor of 200 higher, and that in L1689 three orders of magnitude higher. Much better results are found in our model with radiolysis, which achieves a value of 3×10^{-11}, at a time of 2.75×10^5 yr, as can be seen in the figure, and will be discussed below. Nevertheless, even the result of Model 2 is more than an order of magnitude below the abundance in L1689B, although quite adequate for the other two sources.

Why does Model 1 fail to reproduce observed methyl formate abundances at 10 K. At this temperature, the main limitation to Reaction (2.11) is not the presence of an activation energy barrier, but diffusion barriers for both species (Garrod & Herbst,

2006). The radicals HCO and CH_3O are too massive to reliably tunnel under the diffusion barriers of 1600 K and 5080 K, respectively, and cannot overcome the barrier by hopping because of the low temperature (Garrod & Herbst, 2006). Therefore, in order to reproduce the observed abundances of methyl formate in parts of the ISM at 10 K, other methods are needed. Radiolysis is the method pursued here.

Shingledecker et al. (2018) used the `Nautilus-1.1` model to show how radiolysis increases the abundance of gaseous methyl formate, among other species, in TMC-1 and similar sources (Ruaud et al., 2016). Fig. 2.1 corroborates their results. In Model 2 and in their work, a peak abundance slightly greater than 10^{-11} is achieved at a time of $\approx 3 \times 10^5$ yr, while Model 2 has a larger abundance than their value at times earlier than $\sim 10^5$ yr. While all reactions examined in this section are included in Shingledecker et al. (2018), we have included additional thermal production and destruction mechanisms as well as new radiolysis destruction mechanisms for methyl formate. These newly included reactions are identified in the supplementary material (available online), and are not the dominant reactions that produce and destroy methyl formate (Shingledecker et al., 2018). However, the somewhat larger abundance of methyl formate in Model 2 at non-peak times is caused by the newly included reactions.

The dominant surface reaction scheme to form methyl formate was initially proposed by Bennett et al. (2005), and starts with the electron-irradiation of methanol and carbon monoxide ices, which lead to the production of both methyl formate and glycolaldehyde, depending upon whether the molecule reacting with HCO is methoxy (CH_3O), the precursor of methyl formate, or hydroxymethyl (CH_2OH), the precursor of glycolaldehyde. These reactions are included in Shingledecker et al. (2018). In our Model 2, either HCO or CH_3O can be suprathermal in order to produce methyl

formate efficiently as shown in the following reactions:

$$\mathrm{JHCO^{*} + JCH_3O \rightarrow HCOOCH_3}, \tag{2.13}$$

$$\mathrm{JHCO + JCH_3O^{*} \rightarrow HCOOCH_3}. \tag{2.14}$$

Indeed, reactions 2.13 and 2.14 are the two main reactions that produce methyl formate in our radiolysis model - Model 2. Reaction 2.14 is slightly more important, due to the higher abundance of CH_3O present in the ice, which contributes to a higher number of suprathermal CH_3O molecules being generated. There are multiple gas-phase formation routes, but we find these reactions to be slower than the suprathermal reactive desorption reactions above, which come directly from radiolysis.

For methyl formate, unlike the case for the other species in this study, there are already adequate destruction mechanisms both in the gas phase and for the ice surface and bulk. The main destruction pathways in both models for gaseous methyl formate are

$$\mathrm{HCOOCH_3 + C \rightarrow CO + CO + H + CH_3} \tag{2.15}$$

$$\mathrm{HCOOCH_3 + H_3^{+} \rightarrow H_2 + H_5C_2O_2^{+}} \tag{2.16}$$

Reaction 2.15 is dominant until approximately 10^6 yr while Reaction 2.16 is dominant after this time, while still being significant earlier. This difference arises from the time dependence of the abundance of gas phase C and H_3^+; C is mostly present at early

times until it gets trapped in other carbon-bearing species at later stages, even in purely gas-phase models. In contrast, the abundance of H_3^+ is consistently lower than C before 10^6 yr with an abundance of $\approx 4 \times 10^{-10}$. After 10^6 yr, the abundance of H_3^+ nearly matches that of gaseous carbon in both models, with abundances of $\approx 1.5 \times 10^{-8}$.

The calculated abundances of methyl formate in the ice phases as functions of time are also shown in Figure 2.1. At the current stage of infrared astronomy, however, it is not possible to compare the calculated ice abundances with observational results for a number of reasons, such as the difficulty of observing weak and broad features in space. With the eventual launch of the James Webb Space Telescope, more information on ice composition may become available.

2.3.2 Acetic Acid

Acetic acid has been detected toward SgrB2, but has yet to be detected toward colder regions of the ISM (Mehringer et al., 1997; Remijan et al., 2002; Xue et al., 2019b,a). Prior to this work, as far as we can determine, the abundance of acetic acid toward cold areas of the ISM has not been included in granular chemistry in previous modeling attempts of cold dark clouds.

Numerous gas phase methods have been proposed for assorted COMs, most involving ion-neutral reactions followed by dissociative electron recombination (Huntress & Mitchell, 1979; Ehrenfreund & Charnley, 2000; Blagojevic et al., 2003). As far as we know, very few of these suggestions involve the formation of gaseous acetic acid. However, recently a quantum chemical study was performed on the gas phase synthesis of acetic acid and glycolaldehyde originating from ethanol (Skouteris et al., 2018).

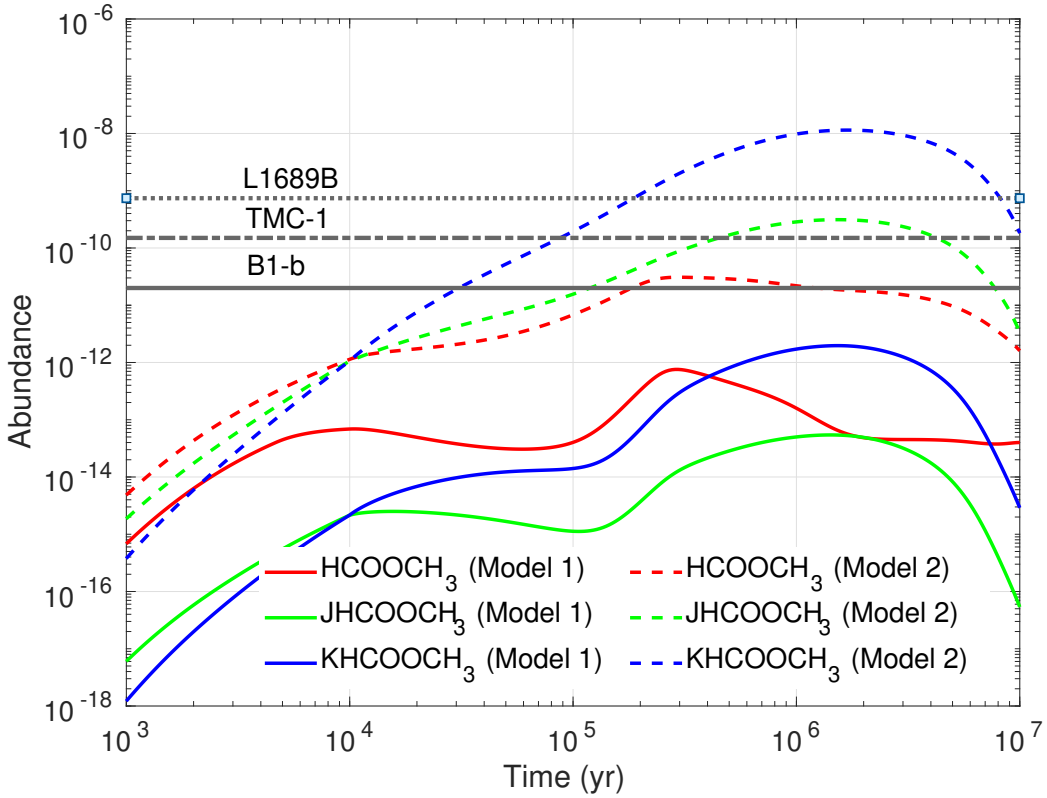

Figure 2.1: Abundance of methyl formate. Gas phase is in red, ice surface in green, and ice bulk in blue. Both models have the same physical and starting conditions, and are run at 10 K. The solid lines refer to the model without radiolysis (Model 1), while the dashed lines refer to the model with radiolysis turned on (Model 2). Horizontal black lines refer to observed abundances in L1689B, TMC-1, and B1-b.

These reactions have been included in our treatment; however, results from Model 2 suggest that 1 per cent reactive desorption from grain ices produces the majority of acetic acid through the following grain surface reactions at 10 K:

$$\mathrm{JHOCO + JCH_3 \rightarrow CH_3COOH} \tag{2.17}$$

$$\mathrm{JOH^* + JCH_3CO \rightarrow CH_3COOH.} \tag{2.18}$$

Reaction 2.17 is a standard thermal reaction from Garrod et al. (2008), while reaction 2.18 is a suprathermal version of a standard thermal reaction from the same source. One of the gas phase reactions from Skouteris et al. (2018) contributes in the production of acetic acid at 10 K via the reaction

$$\mathrm{CH_3CHOH + O \rightarrow CH_3COOH + H.} \tag{2.19}$$

This gas-phase reaction contributes efficiently for a short period of time between 1.5×10^5 yr and 3×10^5 yr, but is less efficient than Reactions 2.17 and 2.18 at all other times in the model.

There may need to be further examination of Reaction 2.17, because the reaction of HOCO with CH_3 might require one of the reactants to be a suprathermal species to overcome an activation energy barrier (Bennett & Kaiser, 2007a). Surprisingly, in Model 2,however, the thermal Reaction 2.17 is more efficient than the same reaction involving suprathermal species. This effect could be due to the lack of HOCO* and CH3* at relevant times. The reactions lead to a maximum gas-phase abundance in Model 2 of 1.375×10^{-13} as shown in Fig. 2.2, compared with the peak abundance

from Model 1 of 1.86×10^{-16}. The higher calculated abundance is not sufficient for current telescopes to detect acetic acid towards TMC-1.

In comparison with methyl formate and dimethyl ether, there are a limited number of gas-phase acetic acid destruction reactions, all involving ions. Reactions taken from Skouteris et al. (2018) suggest that gas phase destruction reactions of acetic acid are mostly through ion-neutral reactions such as Reactions 2.20, 2.21, and 2.22:

$$H_3O^+ + CH_3COOH \rightarrow CH_3COOH_2^+ + H_2O, \tag{2.20}$$

$$H_3^+ + CH_3COOH \rightarrow CH_3COOH_2^+ + H_2, \tag{2.21}$$

$$H_3^+ + CH_3COOH \rightarrow CH_3CO^+ + H_2 + H_2O, \tag{2.22}$$

These reactions are distinct from the neutral-neutral reactions that destroy methyl formate more efficiently, such as the destruction reaction involving atomic C (Reaction 2.15), which acetic acid does not have in our network. Both Model 1 and Model 2 show production and destruction rates for methyl formate at least four orders of magnitude faster than the production and destruction routes for acetic acid.

2.3.3 Glycolaldehyde

Like acetic acid, glycolaldehyde has no reactions in the KIDA network. We have included thermal grain surface and ice mantle reactions from Garrod & Herbst (2006), Hudson et al. (2005), and Garrod et al. (2008), and gas-phase reactions from Skouteris

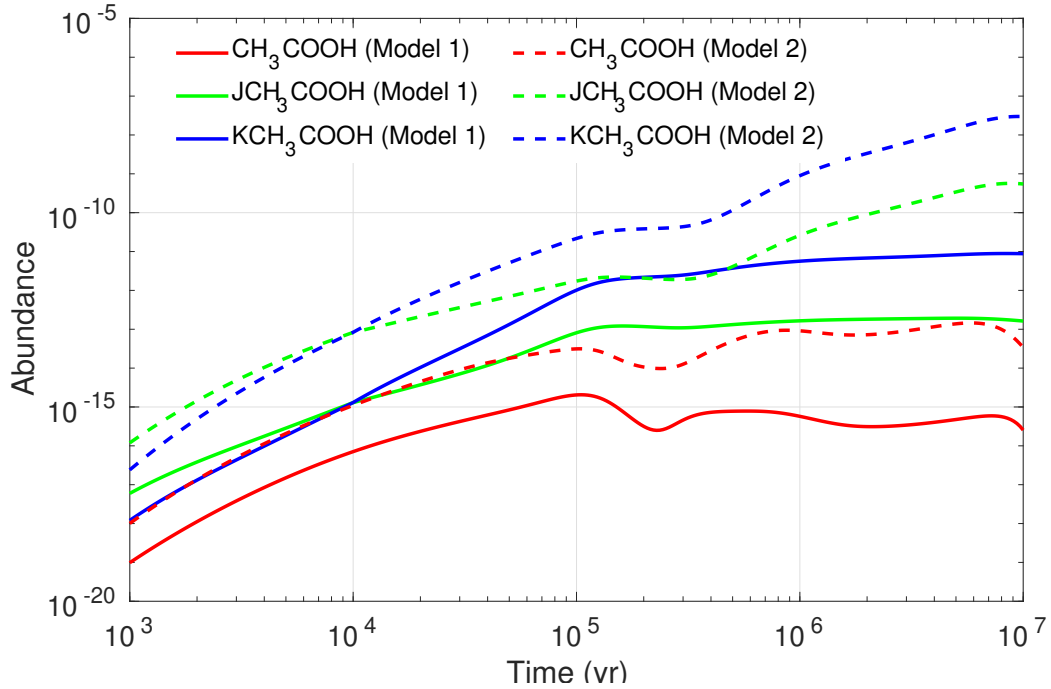

Figure 2.2: Abundance of acetic acid. Gas phase is in red, ice surface in green, and ice bulk in blue. Both models have the same physical and starting conditions, and are run at 10 K. The solid lines show the model without radiolysis, while the dashed lines show the model with radiolysis turned on.

et al. (2018). Previous research into the synthesis of glycolaldehyde suggests that most routes previously studied are not efficient enough to produce significant amounts in the ISM (Woods et al., 2012, 2013). Even with the addition of reactions from Skouteris et al. (2018), production of gas-phase glycolaldehyde is still lacking without radiolysis, as can be seen in Fig. 2.3. The inclusion of radiolysis greatly enhances the abundance of glycolaldehyde with the abundance peaking at about the same abundance as methyl formate, albeit at later times in the model. The peak abundance of gaseous glycolaldehyde is about 1.3×10^{-11} with radiolysis, increasing from the non-radiolysis abundance of about 5.0×10^{-16} . The main reactions that produce gas-phase glycolaldehyde are

$$\mathrm{JCH_2OH + JHCO^* \rightarrow HCOCH_2OH}, \tag{2.23}$$

and

$$\mathrm{JCH_2OH^* + JHCO \rightarrow HCOCH_2OH}. \tag{2.24}$$

Reactions 2.23 and 2.24 are grain-ice surface reactions that lead initially to grain surface glycolaldehyde followed by reactive desorption (Bennett & Kaiser, 2007b; Garrod et al., 2007). The faster reaction is Reaction 2.23 until about 5×10^6 yr, at which point Reaction 2.24 produces the majority of gaseous glycolaldehyde. This is due to the time it takes to generate CH_2OH and CH_2OH^*. The importance of the CH_2OH precursor is highlighted in Bennett & Kaiser (2007b), because the different reactions of CH_2OH and CH_3O with HCO determine if the product will be glycolaldehyde or methyl formate. For CH_2OH, Models 1 and 2 lead to a peak abundance of $\sim 10^{-9}$, while CH_3O has a peak abundance of $\sim 10^{-7}$. The resulting abundances of methyl formate and glycolaldehyde reflect the abundances of their precursors.

Like acetic acid, glycolaldehyde lacks neutral-neutral gas phase destruction mechanisms that methyl formate and dimethyl ether possess. The destruction rates of gas phase glycolaldehyde from Skouteris et al. (2018) included here are so slow that our model has adsorption of glycolaldehyde on to the grains as faster. Notable is the inclusion of the hydrogen atom addition reactions 2.25 and 2.26 for the destruction of grain-surface glycolaldehyde :

$$\mathrm{JHCOCH_2OH + JH \rightarrow JH_2COCH_2OH + JH \rightarrow J(CH_2OH)_2} \tag{2.25}$$

$$\mathrm{KHCOCH_2OH + KH \rightarrow KH_2COCH_2OH + KH \rightarrow K(CH_2OH)_2} \tag{2.26}$$

that result in the production of hydrogenated glycolaldehyde. Without these reactions, the amount of surface ice glycolaldehyde would be greater than the abundance of methyl formate in the ice. It should be mentioned at this stage that glycolaldehyde can be made efficiently on 10 K CO ice in a thermal laboratory experiment via a reaction sequence starting with CO and hydrogen, and thought to proceed via the dimerization of HCO followed by the formation of a C-C bond although the conditions are not the same as in the ISM (Fedoseev et al., 2015; Fuchs et al., 2009).

2.3.4 Dimethyl Ether

Dimethyl ether has been detected toward multiple cold sources, such as TMC-1, L1544, and B1-b, with reported abundances of $\approx 1 \times 10^{-8}$ in TMC-1, $\approx 2 \times 10^{-11}$ in L1544, and $\approx 5 \times 10^{-10}$ in B1-b (Soma et al., 2018; Vastel et al., 2014; Jiménez-Serra et al., 2016; Cernicharo et al., 2012). The formation of dimethyl ether has been

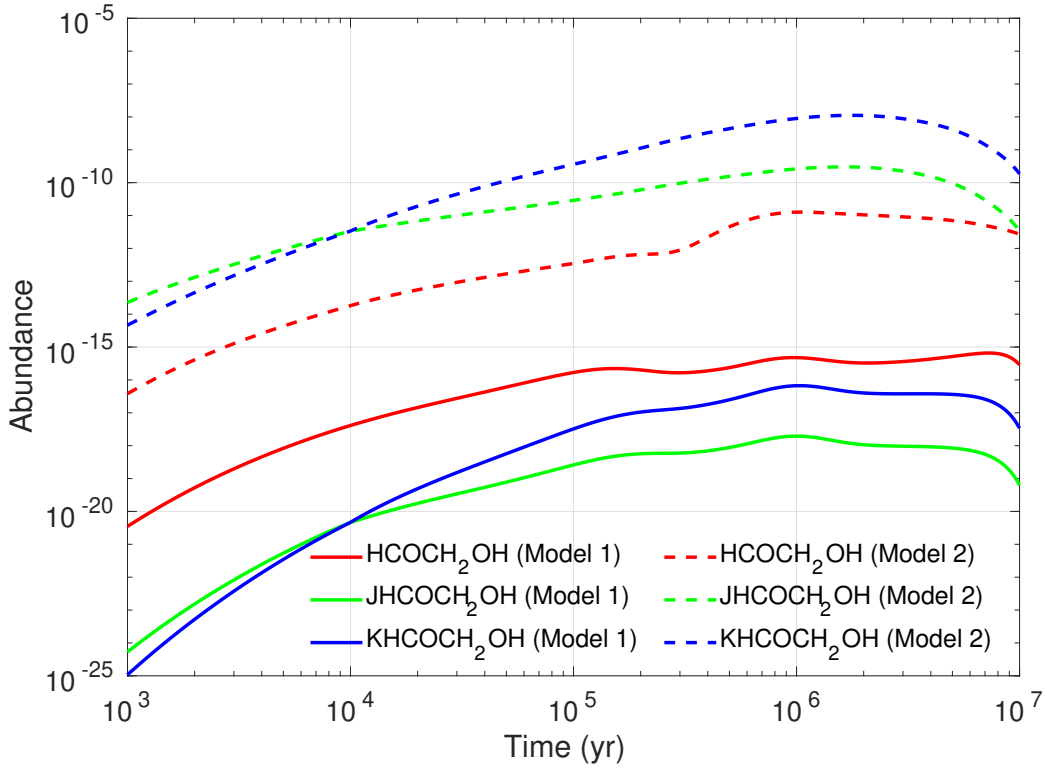

Figure 2.3: Abundance of glycolaldehyde. Gas phase is in red, ice surface in green, and ice bulk in blue. Both models have the same physical and starting conditions, and are run at 10 K. The solid line shows the model with radiolysis off, while the dashed line is the model with radiolysis turned on.

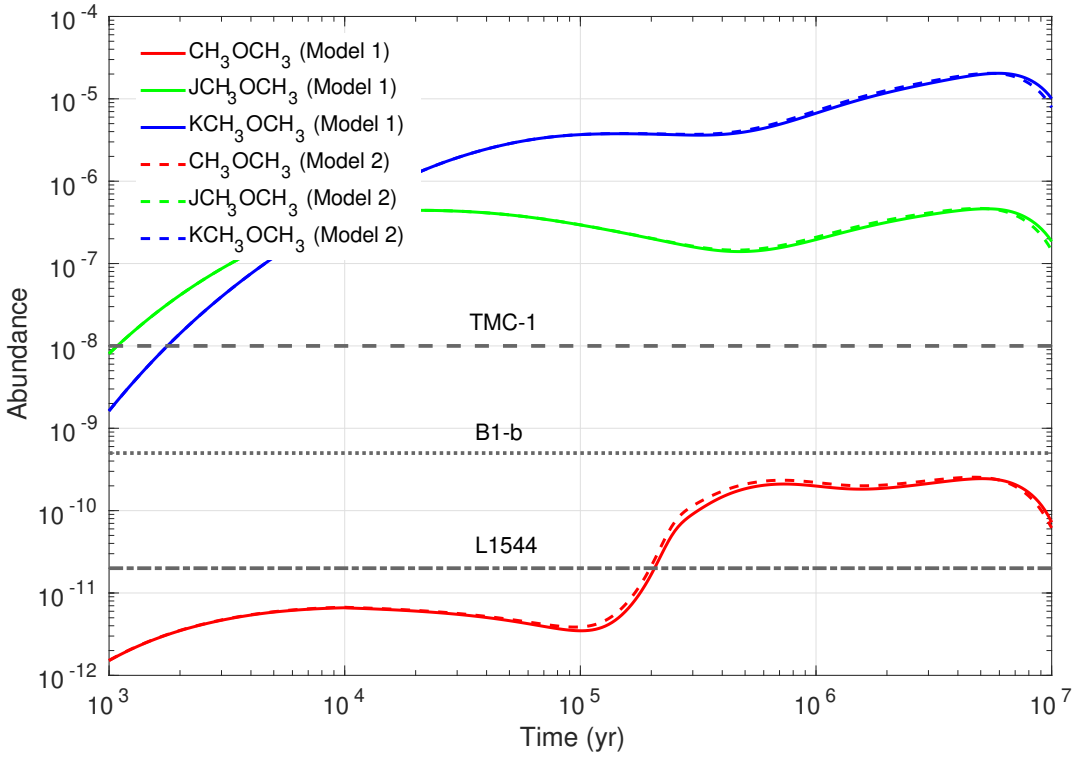

Figure 2.4: Abundance of dimethyl ether in the gas phase (red), ice surface (green), and ice bulk (blue). Both models have the same physical and starting conditions, and are run at 10 K. The solid line shows the model without radiolysis, while the dashed line is the model with radiolysis. Horizontal black lines refer to observed abundances in TMC-1, L1544, and B1-b.

closely linked to the formation of $C_2H_4O_2$ isomers, as they are thought to share similar formation routes and precursors. Dimethyl ether is unique in this chapter, however, as can be seen in Figure 2.4, which shows that radiolysis does not enhance the gas-phase abundance significantly compared with the other species examined here. The calculated abundances in the gas phase with respect to hydrogen peak at $\approx 2.5\times10^{-10}$ with radiolysis, and approximately 2.4×10^{-10} for the model without radiolysis. Both of these values provide a reasonable fit to observations. The small difference between M1 and M2 arises from the main production routes occurring thermally on dust grains without suprathermal reactants; e.g.,

$$JH + JCH_3OCH_2 \rightarrow CH_3OCH_3, \tag{2.27}$$

$$JCH_3 + JCH_3O \rightarrow CH_3OCH_3. \tag{2.28}$$

Despite the inclusion of suprathermal reactions such as the following:

$$JH^* + JCH_3OCH_2 \rightarrow CH_3OCH_3, \tag{2.29}$$

$$JH + JCH_3OCH_2^* \rightarrow CH_3OCH_3, \tag{2.30}$$

$$JCH_3^* + JCH_3O \rightarrow CH_3OCH_3, \tag{2.31}$$

$$JCH_3 + JCH_3O^* \rightarrow CH_3OCH_3, \tag{2.32}$$

none of these reactions dominates, unlike the case of the $C_2H_4O_2$ isomers, because of the efficiency of Reactions 2.27 and 2.28. Reaction 2.27 is still efficient at low temperatures because hydrogen on the grain surface is still mobile, and is more likely to move to encounter JCH_3OCH_2. In order to further explain the other reactions leading to dimethyl ether, a knowledge of the abundance of precursor molecules will be useful, as will direct comparison of rates between models and the reactions mentioned above. Fig. 2.5 shows the abundance of such relevant precursor molecules, while Fig. 2.6 shows the rates for the reactions mentioned above. Most of these in-

termediates are not significantly enhanced by radiolysis chemistry, and the dashed and solid lines appear as one. Clearly, the abundances of both JCH_3 and JCH_3O are sufficient at relevant times that thermal methods can produce dimethyl ether at the observed levels at 10 K. Had the switch for "is_crid" been "on", diffusion would have slightly increased for all species and helped to increase abundances by increasing rates of reaction. This switch is not turned on in the current model, but we are working on a more complex and accurate approach.

Although one would expect Reaction 2.29 to dominate due to the efficient speed of most other radiolysis reactions and the high availablilty of H^* from water ice, Fig. 2.6 shows that Reactions 2.27 and 2.28 dominate in models with and without radiolysis.

Interestingly, Reaction 30 is not included in Fig. 2.6 because of rates constantly below 10^{-40} cm^{-3} s^{-1}. This may be caused by the slow generation of $JCH_3OCH_2^*$. In general, however, since atomic hydrogen can tunnel efficiently under diffusion barriers, allowing for very efficient surface reactions even with other heavy species at low temperatures as long as there is no activation energy, thermal routes with complex molecules and thermal atomic hydrogen can compete with suprathermal reactions at low temperatures. One similar formation mechanism is that of methanol, where models can efficiently produce methanol on dust grains even at low temperatures through the rapid movement of thermal atomic hydrogen.

2.4 Astrochemical Implications

All three of the $C_2H_4O_2$ isomers studied in this chapter show significant increases in calculated gas-phase abundances when radiolysis chemistry is included in our model calculations at 10 K. Of the isomers, methyl formate has already been well observed

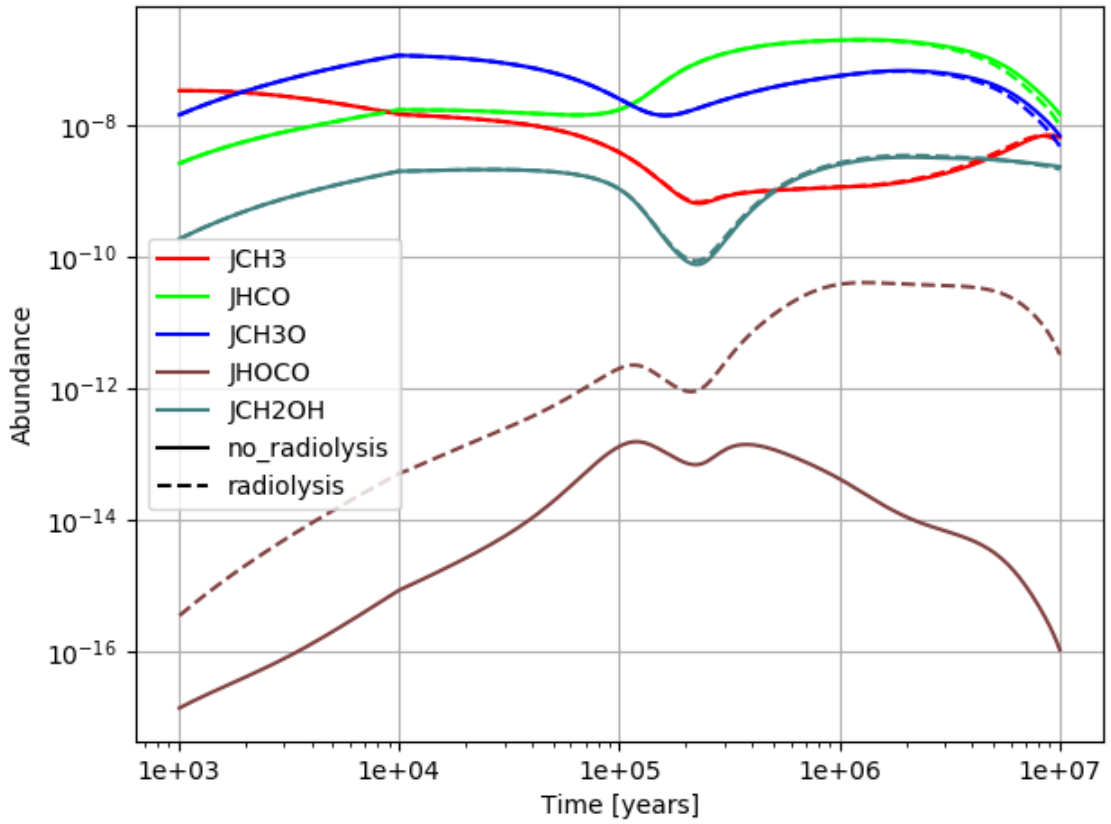

Figure 2.5: Abundances of selected precursor species on the ice surface at 10 K. The solid line refers to the model without radiolysis (Model 1), while the dashed line refers to the model with radiolysis (Model 2).

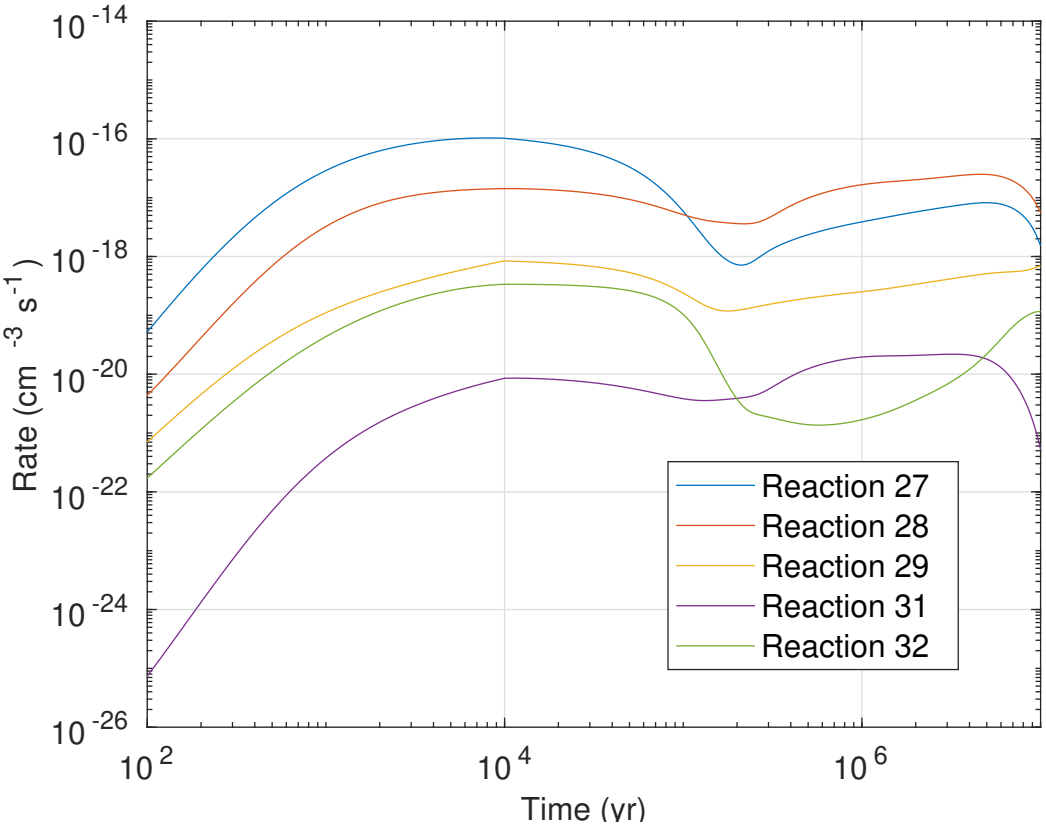

Figure 2.6: Rates of relevant CH_3OCH_3 production mechanisms. Reactions 27 and 28 are in Model 1 (solid lines) and 2 (dashed lines), reactions 29, 31, and 32 are only in Model 2.

within colder environments within the ISM, and has been the subject of a number of previous simulations. However, previous synthetic treatments have underproduced or barely produced sufficient methyl formate (Chang & Herbst, 2016; Balucani et al., 2015; Vasyunin & Herbst, 2013a). Shingledecker & Herbst (2018) first showed that radiolysis greatly improves the gas-phase abundance of multiple molecules, including methyl formate. In this work, we have added new destruction methods of methyl formate through radiolysis, and thermal production and destruction mechanisms, listed in supplementary material (available online) (K. Acharyya, private communication). The molecules examined in this work show that radiolysis should enhance the abundances of more species, potentially allowing their detection in dark clouds. One benefit of including radiolysis is to allow for fast reactions with immediate neighbors in the ice in which the suprathermal species can have enough energy to overcome most reaction barriers before being quenched. This process is in contrast with many surface radical-radical reactions at low temperatures, which generally have a low or no chemical barrier at all, but have high enough diffusion barriers to seriously hamper any reaction that is limited by thermal diffusion, both on the ice surface, and in the bulk of the ice.

Most of the reactions examined in this chapter occur between ice surface species that form products which are assumed to desorb given sufficient energy at 1 per cent of the products. The molecules that remain in or on the ice can lead to the production of more complex COMs, by generating suprathermal species, or reacting with smaller species to increase complexity. For example, methyl formate that does not desorb following a reaction can undergo radiolysis, generating both suprathermal and thermal CH_3O and HCO. Alternatively, HOCO, an intermediate species that is enhanced by radiolysis (Fig. 2.5), can thermally react with either H or CH_3 to

produce HCOOH or acetic acid, respectively.

The increase in abundance for the $C_2H_4O_2$ isomers shows that it is possible to build up abundances of complex molecules such as methyl formate, acetic acid, and glycolaldehyde at 10 K, both in the gas phase and in the ice mantle of the dust grains through radiolytic chemistry and thermal reactions.

Despite the role of dimethyl ether as a COM, a role shared with the three isomers studied, and its detection in similar regions with methyl formate, radiolysis does not significantly impact the calculated gas-phase abundance of this molecule. This difference arises from the efficiency of normal thermal pathways and the lack of efficient suprathermal precursors in the synthesis of dimethyl ether. This exception to the role of radiolysis in enhancing abundances of organic molecules is important to show that not all species are significantly affected positively by radiolysis chemistry. Indeed, there may be efficient thermal routes already in existence, or yet to be examined routes to even more complex molecules that do not rely solely on radiolysis, such as cyanopolyynes (Shingledecker et al., 2018).

Although gas phase reactions that generate acetic acid and glycolaldehyde have been included, they are mostly insignificant compared with the resulting rates of the suprathermal reactions. More gas phase quantum mechanical studies or experimental studies on reaction rates should be conducted on all species examined here, but acetic acid is still lacking in information compared with methyl formate, glycolaldehyde, and dimethyl ether. These studies should be done in order to potentially find new pathways, because we could be ignoring other granular or gas-phase routes to all of these molecules.

Unlike the situation for acetic acid and glycolaldehyde, a gas-phase synthesis for

dimethyl ether and methyl formate has been constructed by Balucani et al. (2015), based at least partially on measured and calculated rate coefficients involving neutral species. An earlier treatment was reported by Vasyunin & Herbst (2013a). One important reaction in the sequence is a radiative association between the methyl and methoxy radicals to form dimethyl ether, which has not been studied in the laboratory:

$$CH_3 + CH_3O \rightarrow CH_3OCH_3 + h\nu. \tag{2.33}$$

Calculations by Tennis et al. (2021) indicate that this reaction occurs at near the collisional value at 10 K. With this large rate coefficient, the gas-phase approach of Balucani et al. (2015) embedded in the OSU2009 network shows significant enhancements to the calculated abundances of dimethyl ether and methyl formate, and can account for the observation of the former in L1544.

There are certain aspects of the treatment of radiolysis that can possibly be improved. For example, the assumption that suprathermal species react with unit efficiencies should be examined more closely. In addition, there are other aspects of cosmic ray interactions that have yet to be implemented into `Nautilus`, such as a more advanced treatment of cosmic ray grain heating, and sputtering caused by cosmic rays, both of which should help remove species present in the surface layers and the bulk of the ice (Kalvāns & Kalnin, 2019). This is important because most species formed through radiolysis and other grain production routes remain adsorbed on the ice surface or trapped within the ice bulk, as shown in Figures 2.1, 2.2, 2.3, and 2.4.

Inclusion of low energy resonances below the minimum energy for suprathermal species has been suggested by C. Arumainayagam, private communication. Further studies are also needed in the areas of diffusion on and within the ice, because there appears to be some evidence that a diffusion-like process has been missed (Shin-

gledecker et al., 2020). Another problem concerns the desorption of bound species from the ice surface and bulk mantle. At 10 K, not even most volatile species will be thermally desorbed rapidly; hence the importance of photodesorption, reactive desorption, and sputtering caused by cosmic rays (Dartois et al., 2019). There are other treatments of reactive desorption that have a more nuanced approach than the base probability of desorption based on RRK theory (Garrod et al., 2007; Minissale et al., 2016) or our assumed probability of 1 per cent; we do not consider them in this chapter.

2.5 Conclusions

In this work, we have added to the use of the method of radiolytic chemistry via the generation of suprathermal species to determine the abundances of selected COMs in cold dark clouds, such as TMC-1. The base versions of `Nautilus-1.1` and the KIDA network have been expanded to allow for radiolysis chemistry in modeling the chemistry of the $C_2H_4O_2$ isomers methyl formate, glycolaldehyde, and acetic acid, as well as the important COM dimethyl ether. The results of the models discussed here show that radiolytic chemistry greatly increases the modeled abundance of these species except for dimethyl ether, so much so that it may be possible to detect glycolaldehyde in dark clouds. However, there is likely not enough gaseous acetic acid to be observed. Additionally, there are abundances of the $C_2H_4O_2$ isomers and dimethyl ether remaining within the ice. These remaining species could be used as building blocks for molecules of even greater complexity if activated by UV photons, as discussed by Jin & Garrod (2020) or by cosmic rays. If the complex molecules remain on the grain mantle, however, infrared detection will be difficult for a number of reasons,

although the advent of JWST might allow some more detections.

Chapter 3

Sputtering of interstellar dust grains

In the interstellar medium (ISM), the formation of complex organic molecules (COMs) is largely facilitated by surface reactions. However, in cold dark clouds, thermal desorption of COMs is inefficient because of the lack of thermal energy to overcome binding energies to the grain surface. Non-thermal desorption methods are therefore important explanations for the gas-phase detection of many COMs that are primarily formed on grains. Here we present a new non-thermal desorption process: cosmic ray sputtering of grain ice surfaces based on water, carbon dioxide, and a simple mixed ice. Our model applies estimated rates of sputtering to the 3-phase rate equation model `Nautilus-1.1`*, where this inclusion results in enhanced gas phase abundances for molecules produced by grain reactions such as methanol (CH_3OH) and methyl formate ($HCOOCH_3$). Notably, species with efficient gas phase destruction pathways exhibit less of an increase in models with sputtering compared to other molecules. These model results suggest that sputtering is an efficient, non-specific method of non-thermal desorption that should be considered as an important factor*

in future chemical models. [1]

3.1 Introduction

In cold dark clouds, recent detections of complex organic molecules including some $C_2H_4O_2$ isomers have led to an influx of studies examining chemical formation routes (Jiménez-Serra et al., 2016; Soma et al., 2018). Warmer sources have well-understood thermal production routes for species formed both in the gas phase and on grains, with efficient grain processes producing COMs, which then thermally desorb with the majority of ice from dust grains (Charnley et al., 1992). The production of the same COMs in cold dark clouds has been studied, yet continues to be an area of interest, if not fully understood (Vasyunin & Herbst, 2013b; Chang & Herbst, 2016; Balucani et al., 2015; Jin & Garrod, 2020). Desorption from grain mantles is a common problem in dark clouds, as most models still under-produce gas-phase abundances of COMs, though non-thermal desorption methods are consistently being developed and applied to models of cold dark clouds, with a particular emphasis on reactive desorption and photodesorption (Garrod et al., 2007; Öberg et al., 2009).

Cosmic rays are highly energetic ions travelling at significant portions of the speed of light, with H^+ being the most common ion (Cummings et al., 2016). Their role in interstellar grain chemistry has been increasingly examined, with radiolysis theory and experiments highlighting the importance of cosmic ray and grain interactions in generating chemical diversity through ionization and excitation of ices (Hudson et al., 2005; Abplanalp et al., 2015; Boyer et al., 2016; Shingledecker & Herbst, 2018). When cosmic rays collide with interstellar ices and dust grains, perhaps the most noticeable

[1] Originally published as Paulive et al. (2022)

effect is the heating of the aggregate, referred to as whole grain cosmic ray heating or simply cosmic ray heating (CRH), causing periods of enhanced thermal activity, such as desorption and possibly enhanced thermal diffusion (Hasegawa & Herbst, 1993; Kalvāns, 2018).

The energy deposited to the surface by cosmic rays does not just cause thermal heating, ionization, and excitation; sputtering is a direct outcome of cosmic ray interactions with grain ices. Sputtering is defined as the desorption of material resulting from high energy particle impacts. This is a separate process from the thermal desorption resulting from the heating of the grains, as the act of collision itself causes not just heating, but also the ejection of surface molecules. Multiple experiments have been recently done to examine the sputtering of high-energy cosmic rays ($\geq$ MeV) impacting interstellar ices, and have shown that sputtering is an efficient method of desorption from surfaces (Dartois et al., 2013, 2015b). Even more recently, chemical models including experimental sputtering data were utilized, demonstrating increased gas-phase abundances of various molecules in chemical kinetic models, although the experiments used heavier ions than the most common cosmic ray, H^+ (Dartois et al., 2018; Wakelam et al., 2021).

The many theories of sputtering predict that the interaction of cosmic rays and ice surfaces varies based on the energy and mass of the incoming particle, resulting in competition between sputtering caused by high energy ($\geq$ MeV) particles and less energetic particles in the keV range. The competing regimes are further divided by two mechanisms of energy transfer: electronic sputtering, where ineleastic collisions cause movement from coulombic interactions, and nuclear sputtering, where elastic collisions between nuclei cause physical recoil and desorption (Sigmund, 1969; Brown et al., 1978). Lower energy particles more efficiently deposit energy into surfaces

through elastic (nuclear) collisions, while for most cosmic ray energies, inelastic (electronic) collisions are the main source of energy transfer (Andersen & Bay, 1981; Johnson, 1990). Reasons for the discrepancy in effectiveness will be examined in a later section.

In this chapter, we examine sputtering theory by including sputtering into a rate-equation based 3-phase model under cold dark cloud conditions. Section 3.2 presents the theoretical treatment of sputtering used in the model along with all physical parameters and chemical networks utilized. Section 3.3 covers the results of the models for theories based on water, carbon dioxide, and a theoretical mixed ice. Section 3.4 discusses the implications sputtering has on interstellar environments with comparisons to astronomical observations, and Section 3.5 concludes our work.

3.2 Models

The chemical models reported in this chapter make use of the three-phase rate equation-based gas-grain program `Nautilus-1.1` (Wakelam et al., 2012; Ruaud et al., 2016). The three phases comprise the gas, the top layers of the grain ice (two monolayers in this instance) and the remaining ice on the dust grain mantle, called the bulk. This distinction is relevant to diffusion of ice species in the mantle, and a variety of adsorption and desorption methods utilized in `Nautilus-1.1`. These methods include photodesorption, reactive desorption, and thermal desorption, which allow for exchange of species between the ices upon the grain surfaces and the gaseous interstellar medium, are further described later in the section (Vasyunin & Herbst, 2013b). Sputtering, which removes particles from the ice surface and bulk, is slightly different from already included non-thermal desorption methods due to the frequency

Table 3.1: Initial abundances of elements with respect to total hydrogen nuclei

Species	Abundance
H_2	0.499 [a]
He	9.000×10^{-2} [a]
N	6.200×10^{-5} [a]
C^+	1.700×10^{-4} [b]
O	2.429×10^{-4} [c]
S^+	8.000×10^{-8} [d]
Na^+	2.000×10^{-9} [d]
Mg^+	7.000×10^{-9} [d]
Si^+	8.000×10^{-9} [d]
P^+	2.000×10^{-10} [d]
Cl^+	1.000×10^{-9} [d]
Fe^+	3.000×10^{-9} [d]
F	6.680×10^{-9} [e]

[a] (Wakelam & Herbst, 2008)
[b] (Jenkins, 2009)
[c] (Hincelin et al., 2011)
[d] (Graedel et al., 1982)
[e] (Neufeld et al., 2005)

of sputtering events, and the number of species removed from both the ice surface and bulk. These will be examined further in Section 3.2.2.

With the Nautilus code, we are able to run a series of chemical models with specific parameters in which the diverse effects of cosmic ray interactions in various combinations of activity or inactivity on sputtering are explored. Further details, which apply to all models, such as initial abundances, and constant physical conditions are shown in Table 3.1 and 3.2. These physical conditions, which are the same as in Ruaud et al. (2016), are comparable to those observed in cold, dark molecular clouds, which are the environments on which we focus.

To accurately gauge the impact of each new or updated process examined in this chapter, we have devised separate models with differing processes. These are shown in Table 3.3, which lists the name by which the specific model will be referenced in this

Table 3.2: Physical conditions utilized in models for this work, based on TMC-1 conditions

Parameter	TMC-1
n_{H} (cm^{-3})	10^4
n_{dust} (cm^{-3})	1.8×10^{-8}
T_{gas} (K)	10
T_{dust} (K)	10
N_{site} (cm^{-2})	1.5×10^{15}
ζ (s^{-1})	1.3×10^{-17}
A_{V}	10

chapter. The table also indicates the inclusion or absence of cosmic ray whole grain heating (CRH) and sputtering in the labelled models (Hasegawa & Herbst, 1993). Our models include some features not in the standard version of `Nautilus-1.1`. These additional options include a competitive tunneling mechanism between activation and diffusion barriers set to the faster option, and an option that prevents all species but H and H_2 from tunneling under activation energy barriers of surface reactions, set to "on" (Herbst & Millar, 2008; Shingledecker et al., 2019a). Nonthermal desorption mechanisms for surface species also have associated options. Photodesorption (Bertin et al., 2013) and cosmic ray induced photodesorption (Hasegawa & Herbst, 1993) are included, along with reactive desorption at 1 per cent probability (Garrod et al., 2007). These three switches are set to "on", with both the photodesorption yield, and the cosmic ray induced photodesorption yield set at 1×10^{-4}. All models have the same parameters for the features described above, except in the cases of sputtering and CRH.

Table 3.3: Model identifiers with a listing of the active sputtering rate and whether cosmic ray heating was included

Model	Sputtering	Note
1H	Off	Base Model
2HS	On - H_2O Ice	CRH
3S	On - H_2O Ice	No CRH
4HSC	On - CO_2 Ice	CRH
5SC	On - CO_2 Ice	No CRH
6HSM	On - Mixed Ice	CRH
7SM	On - Mixed Ice	No CRH

3.2.1 Network

The `Nautilus-1.1` reaction network used in this study has been expanded to include more complex chemical species that lead up to the $C_2H_4O_2$ isomers, methyl formate ($HCOOCH_3$), glycolaldehyde ($HCOCH_2OH$), and acetic acid (CH_3COOH), as described in Paulive et al. (2021). These molecules are among a class of species known as complex organic molecules (COMs), which range from 6-13 atoms and are partially saturated.The base network of gaseous reactions is taken from the KIDA network (Wakelam et al., 2012). The granular reaction network is from the `Nautilus-1.1` package, with additional thermal grain-surface reaction pathways leading to $C_2H_4O_2$ isomer precursors from Garrod & Herbst (2006). Used initially in hot core models, these reactions have been included here to provide likely thermal pathways to COMs, which may eventually leave the grain surface through cosmic ray interactions (Skouteris et al., 2018). Species with a prefix of "J" are those on the surface of the ice mantle, while species with a "K" lie within the bulk of the ice, which, after the simulation has completed running (10^7 yrs), contains close to 100 monolayers of ice. Desorption energies, E_D, are from a combination of Garrod & Herbst (2006); Garrod et al. (2008); Garrod (2013). The diffusion barriers (E_b) are $0.4 \times E_D$ for ice surface species and $0.8 \times E_D$ for bulk species. All ices in this chapter are considered

amorphous solids.

3.2.2 Sputtering Theory

As noted above, sputtering is the process of impacting a surface (or surface of a liquid) with high energy particles resulting in the ejection of particles from the surface into the surrounding space. By applying sputtering to grain surfaces in the interstellar medium, it is possible to estimate rate coefficients, used to calculate rates, based on cosmic ray grain interaction rates, stopping powers, and average energy loss due to collisions, all of which can be used in rate-equation based models. In these models, the overall rate of desorption ($\mathrm{R^{tot}}$) for some mantle species, i, is the sum of all desorption processes. Example desorption mechanisms include thermal desorption ($\mathrm{R^{Th}}$, photodesorption ($\mathrm{R^{Pho}}$), and reactive desorption ($\mathrm{R^{RD}}$). With the addition of sputtering in our models, the calculation of the rate of sputtering ($\mathrm{R^{s}}$) is necessary. The overall rate of desorption for species i is as follows:

$$\mathrm{R^{tot}} = -\frac{dN_i}{dt} = \mathrm{R^{Th}} + \mathrm{R^{Pho}} + \mathrm{R^{RD}} ... + \mathrm{R^{s}}. \tag{3.1}$$

Here $\frac{dN_i}{dt}$ is the rate of change of the gas-phase concentration of desorbing species i, with units of $\mathrm{cm^{-3}\ s^{-1}}$. The individual rate processes, R, are each given by first-order rate coefficients, k, multiplied by N_i, so that the total rate, $\mathrm{R^{tot}}$, can be written by

$$\mathrm{R^{tot}} = -\frac{dN_i}{dt} = N_i \left(k_{Th} + k_{Pho} + k_{RD} ... + k_s\right). \tag{3.2}$$

Here k_{Th}, k_{Pho}, k_{RD}, and k_{s} are the rate coefficients for thermal desorption, photodesorption, reactive desorption, and sputtering, respectively. We will examine how to

calculate k_s later in the section. It is important to note that our models assume all species are affected by sputtering at the same rate coefficient. When referring to the rate coefficient of sputtering off of water ice, carbon dioxide ice, or mixed ice, all ice mantle species in the model will take on the respective sputtering rate for the assumed ice composition. For example, when referring to water ice sputtering, the model implements this by setting the rate coefficient of all ice mantle species to be the calculated rate coefficient for water ice. Models with CO_2 ice sputtering set the rate coefficient of all species to be equal to that of CO_2 ice.

The units of concentration for species i can vary, so long as they are consistent throughout the model. The number of molecules on a grain, the fractional abundance to hydrogen or water, and the relative density are all common. For this model the concentration has the units of cm^{-3}.

Some basis for the assumption that all ice species in the model take on the respective sputtering rate is given in the next paragraph. The assumption is justified by two factors: first is the physical structure of amorphous solids. Clements et al. (2018) shows that the formation of interstellar ices at 10 K results in a highly porous structure, creating large "chunks" of ice that are interconnected to form the ice mantle. The ices themselves are observed to be approximately 70% water ice (Whittet et al., 1996), meaning that if there is a water ice molecule that is successfully removed from either the surface or the mantle, there is a probability that the water molecule will be removed with neighboring species, or if the ice is porous enough, a large "chunk" of ice will be desorbed alongside the sputtered molecule. Second is experimental evidence regarding sputtering yields. There are multiple studies on the effectiveness of sputtering multiple molecules and dimers from a chemisorbed metal surface (Gades & Urbassek, 1995). Recent experiments with swift heavy ions colliding with amorphous

ices and crystalline water ice also sputter large quantities of ice, about 20,000 water molecules per incident ion, although the high number of desorbed molecules is not attributed to the porosity of the ice (Dartois et al., 2013, 2015a, 2018). These two factors suggest that sputtering has the possibility of desorbing multiple ice species per incident cosmic ray because water, the main component of the ice, will either be desorbed alongside whatever else it is next to, or in the same cluster as the water molecules that are sputtered.

We can approximate a first-order sputtering rate coefficient, k_s, in units of cosmic ray particles per second, starting with a cosmic ray flux for the interstellar medium ϕ_{ism} (cosmic ray particles s^{-1} cm^{-2}) and a cross section for the cosmic ray interacting with a molecule on the grain surface σ (cm^2):

$$k_s = \sigma \phi_{ism}. \tag{3.3}$$

We obtain a value for the cosmic ray flux by integrating the Spitzer-Tomasko energy function $j(E)$ (Spitzer & Tomasko, 1968) over the cosmic ray energy distribution from 0.3 MeV (3×10^{-4} GeV) to 100 GeV given by the equation:

$$j(E) = \frac{0.90}{(0.85 + E_G)^{2.6}} \frac{1}{(1 + 0.01/E_G)}. \tag{3.4}$$

Here E_G is the energy of cosmic rays in GeV. The distribution is graphed in Figure 3.1. Assuming that cosmic rays are isotropic and then integrating over the energy distribution results in an interstellar cosmic ray flux ϕ_{st} of 8.6 particles cm^{-2} s^{-1}. An additional term, ζ, based on the cosmic ray ionization rate of $\approx 1.36 \times 10^{-17}$ s^{-1} allows for easy scaling of the cosmic ray flux depending on the ionization rate in

varying areas of the ISM, similar to the scaling factor included in Shingledecker & Herbst (2018), where the overall flux term is as follows:

$$\phi_{ism} = \phi_{st} \frac{\zeta}{1.36 \times 10^{-17}}. \tag{3.5}$$

Obtaining an exact sputtering cross section that will work with our averaged model is difficult, as the sputtering cross section is dependent on the stopping power of the target ice, as well as the mass and energy of the incident cosmic ray (Townsend, 1993; Andersen & Bay, 1981). Although there are experimentally determined sputtering cross sections, they are difficult to incorporate into our model for a number of reasons. First, `Nautilus-1.1` does not take into account specific cosmic ray nuclei. Secondly, many experimental and theoretical cross sections are not specific to sputtering, instead measuring all manners of destruction, called a destruction cross section. This results in "double counting" other included desorption processes and radiolysis effects if this total destruction cross section were to be used for calculating sputtering rates.

A total cross section σ_t is split into two general categories for collisions: a nuclear cross section σ_n, for elastic collisions, and an electronic (inelastic) cross section σ_e. The electronic cross section can be further split into ionizing σ_{ion} and excitation σ_{exc} cross sections. The different partial cross sections are shown in the following equation:

$$\sigma_t = \sigma_n + \sigma_e = \sigma_n + \sigma_{\text{ion}} + \sigma_{\text{exc}}. \tag{3.6}$$

These cross sections all contribute to physical effects such as sputtering and whole grain heating. The fraction of each cross section that contributes to each resulting interaction type is not well defined.

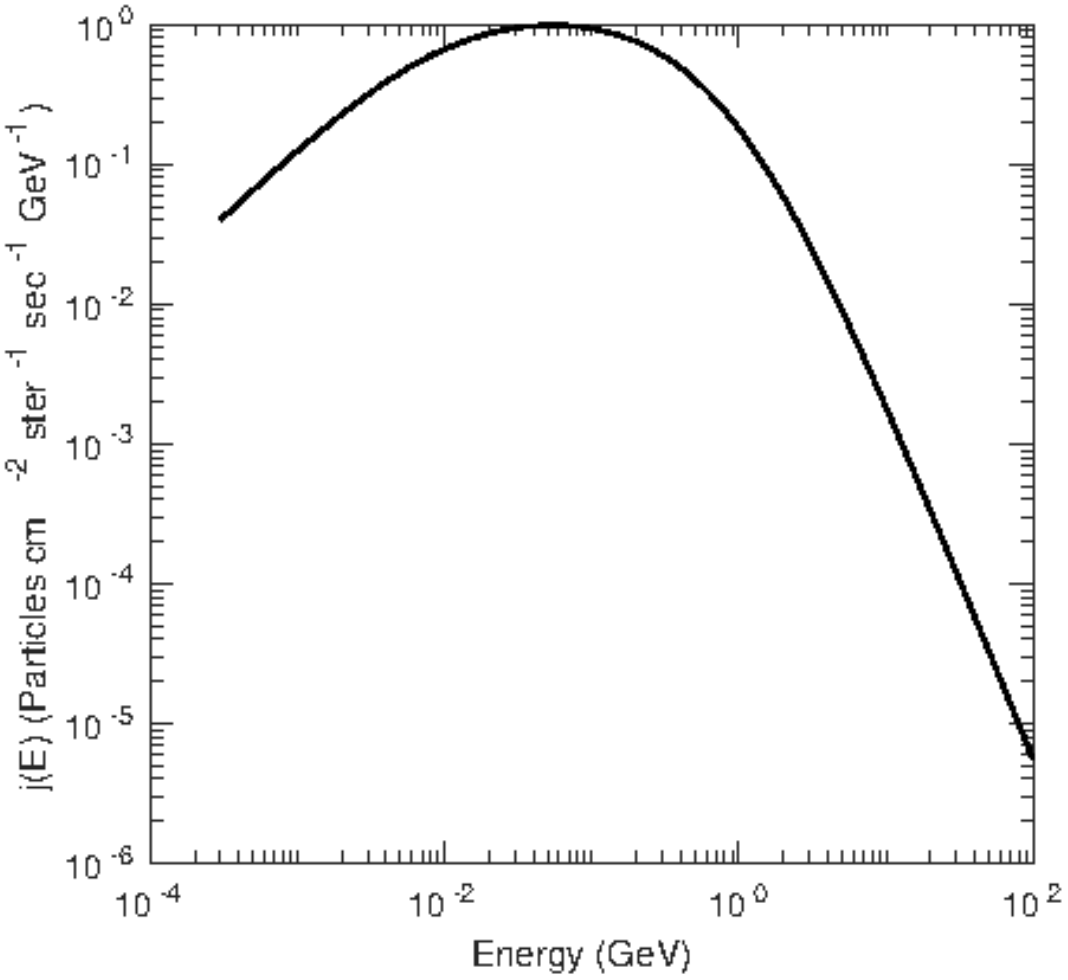

Figure 3.1: Cosmic ray energy distribution function, from Spitzer & Tomasko (1968). The cosmic ray flux in particles cm^{-2} s^{-1} is obtained by integrating j(E) over the cosmic ray energy distribution, from 3×10^{-4} GeV to 100 GeV. This results in an overall cosmic ray flux of 8.6 particles cm^{-2} s^{-1}.

In a similar manner to splitting the total cross section into more focused cross sections to describe different processes, it is helpful to divide E_{total}, the total energy loss, into more specific terms:

$$E_{\text{total}} = N_{\text{ion}}\bar{E}_{\text{ion}} + N_{\text{exc}}\bar{E}_{\text{exc}} + N_{\text{ion}}\bar{E}_s + \nu_{\text{n}}(E_{\text{total}}) \tag{3.7}$$

where N_{ion} and N_{exc} are the numbers of ionizations and excitations, respectively, while the average energies lost to ionization and excitation are $\bar{E}_{\text{ion}}$ and $\bar{E}_{\text{exc}}$. $\bar{E}_s$ is the energy lost to sub-excitation secondary electrons, or free electrons resulting from ionization that are too low in energy to cause further ionizations or excitations. These secondary electrons eventually lose their energy to the surface as vibrational or rotational energy, and these directly contribute to the motions of species on the ice surface, which can result in sputtering. The sum of the contributions of all contributing electronic effects on a single molecule can be referred to as the average electronic energy loss per ion-pair, or W_{e}, with units of eV. W_{e} for a single water molecule is approximately 30 eV (Johnson & Brown, 1982).

The remaining term, $\nu_{\text{n}}(E_{\text{total}})$, where ν_{n} is the fraction of E_{total} lost by nuclear effects, is the energy lost due to nuclear elastic collisions, and is related to the nuclear stopping power cross section, in units of eV cm^2, which contributes to multiple methods for sputtering. The quantity $\nu(E_{\text{total}})$, divided by the number of nuclear collisions per incident ion, is the average energy lost per nuclear collision, or W_{n} (Johnson, 1990). W_{n} can be estimated by multiplying the energy of displacement, or the energy required to remove a species from the energy well of the surface, E_{dis}, by 2.5 (Sigmund, 1969). Depending on the path of the cascade collisions, and how deep the ice particle in question is located within the bulk of the ice, E_{dis} can range from the desorption

energy, $E_{\rm b}$, for surface species,to $5E_{\rm b}$ for species embedded in the crystal structure. We approximate $E_{\rm dis}$ for our physisorbed ice as $2E_{\rm b}$. This results in a $W_{\rm n}$ for water ice of approximately 2.45 eV, from an $E_{\rm b}$ of 0.49 eV (Garrod et al., 2008).

The cross sections σ_n and σ_e are approximated from the nuclear and electronic stopping power cross sections $S_{\rm n}$, and $S_{\rm e}$. Figure 3.2 shows a graph of nuclear and electronic stopping powers for hydrogen and iron ions impacting water ice, as approximated using the values for liquid water and calculated by the `SR-NIEL` web tool (Boschini et al., 2014). Stopping powers are dependent on the mass and energy of the incident ion and the target material. Figure 3.2 shows a three order of magnitude difference between electronic stopping powers and nuclear stopping powers for incident hydrogen ions, and an increasing difference in stopping power with energy for incident iron ions. This suggests that the majority of energy deposited into grain ices by cosmic rays comes from electronic interactions, compared with nuclear interactions. Figure 3.2 also shows that the stopping power of iron ions impacting water is significantly higher than hydrogen for both nuclear and electronic collisions. We will not further examine iron cosmic rays in this work however, as they are significantly less abundant compared with hydrogen cosmic rays (Cummings et al., 2016; Blasi, 2013). In order to account for the differences in terms and physical causation for sputtering, we will continue to examine nuclear and electronic sputtering separately.

Nuclear (Elastic) Sputtering

Nuclear sputtering is caused via collisions, most notably in the keV region in which elastic collisions occur within the ice leading to rebounds and eventually sputtering (Johnson, 1990). This energy range is below that of cosmic rays that bombard dust particles. Throughout the cosmic ray energy distribution used in this chapter

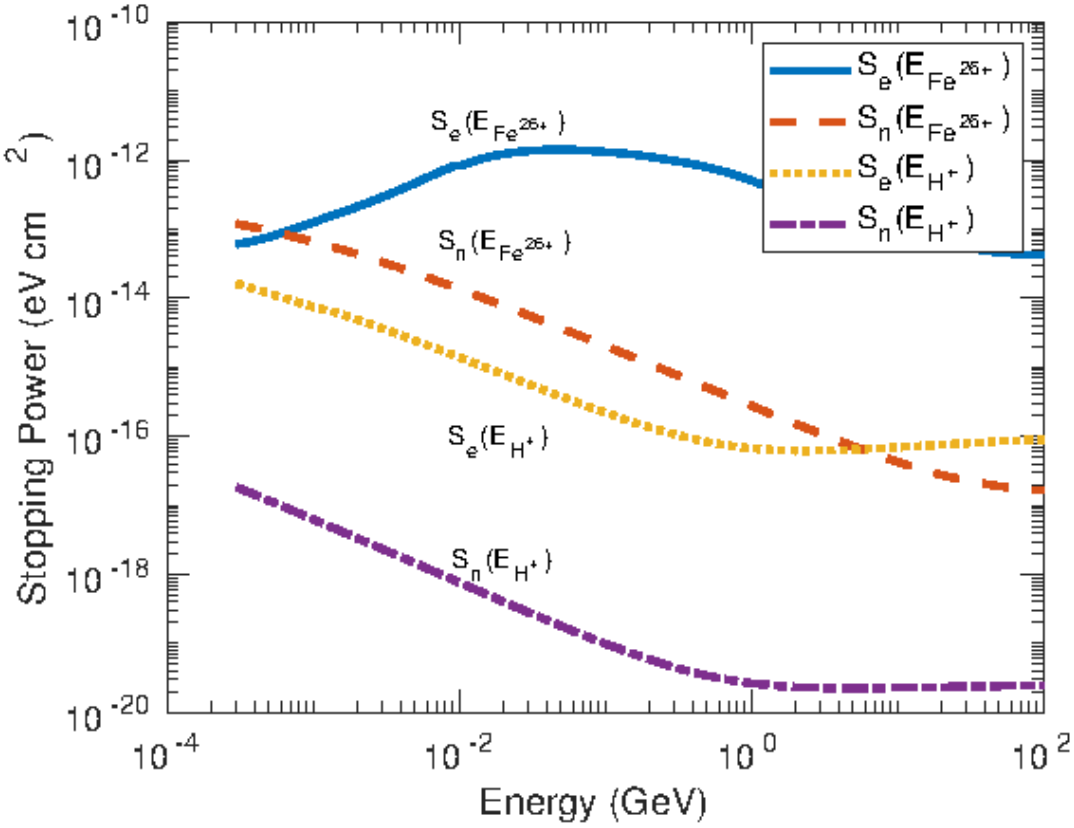

Figure 3.2: Electronic and nuclear stopping powers of H^+ and Fe^{26+} ions impacting liquid water. H^+ electronic stopping powers are yellow dots, nuclear are purple dot-dashed. Iron incident ion electronic stopping powers are solid blue, nuclear are orange dashed. Energy ranges from 3×10^{-4} GeV to 100 GeV. At these energies, S_e of hydrogen is consistently $> 10^2$ than the S_n. Liquid water is used as an approximation for amorphous solid water, which is not included in the `SR-NIEL` web tool. Calculated using `SR-NIEL` web tools http://www.sr-niel.org/index.php/.

(3×10^{-4} GeV to 100 GeV), nuclear stopping powers are approximately three orders of magnitude lower than electronic stopping powers for water ice. For use in our models, which do not account for differing cosmic ray ions and energies, we calculate a weighted average stopping power ($\bar{S}$) by the formula

$$\bar{S} = \frac{\sum S(E) j(E)}{\sum j(E)}, \tag{3.8}$$

where $S(E)$ is the range of stopping powers over a range of energies (separated into nuclear and elastic stopping powers), and $j(E)$ is the Spitzer-Tomasko cosmic ray energy function. Our calculation results in an average nuclear stopping power for H^+ impacting water ice of 3.489×10^{-18} eV cm^2. To convert our nuclear stopping power to a nuclear cross section, we simply divide S_n by W_n, resulting in an average nuclear sputtering cross section of 1.424×10^{-18} cm^2. The rate coefficient for nuclear sputtering can now be expressed as:

$$k_{ns} = \sigma_n \phi_{ISM} \approx \frac{S_n}{W_n} \phi_{ST} \frac{\zeta}{1.36 \times 10^{-17}}. \tag{3.9}$$

which contains the assumption that only one particle will be ejected per incident ion, which may not be the case. A suitable yield term has been derived by Sigmund (1969) and modified by Johnson (1990) resulting in the following expression for the nuclear scattering yield Y_ns:

$$Y_{ns} \approx \frac{3\alpha S_n}{2\pi^2 \bar{\sigma}_\mathrm{diff} U}. \tag{3.10}$$

This is an equation for cascade sputtering of a planar surface, where α is an ex-

Table 3.4: Parameters for nuclear sputtering calculations on amorphous solid water.

Parameter	Value	Reference
S_n (eV cm^2)	3.489×10^{-18}	This work
W_n	2.45 eV	This work, (Sigmund, 1969)
$\bar{\sigma}_{\rm diff}$ (cm^2)	3.6×10^{-16}	(Johnson, 1990)
U (eV)	0.49	(Garrod & Herbst, 2006)
α	0.6	(Andersen & Bay, 1981)
Y_{ns}	1.8×10^{-3} H_2O per H^+	This work
σ_n (cm^2)	1.424×10^{-18}	This work

perimentally determined fraction of the nuclear stopping power that is involved in cascade collisions that are close to the surface, $S_{\rm n}$ is the nuclear stopping power, $\bar{\sigma_{\rm diff}}$ is the average diffusion cross section, and U is the average binding energy in eV. For water ices being impacted by H^+ ions, Equation (3.10) yields an average result of of 1.8×10^{-3} particles per cosmic ray proton, with the parameters shown in Table 3.4.

The final form of the rate coefficient for nuclear sputtering is

$$k_{ns} = Y_{ns}\sigma_n\phi_{ISM}, \tag{3.11}$$

which, fully expanded, is as follows:

$$k_{ns}(s^{-1}) = \left(\frac{3\alpha S_n}{2\pi^2\bar{\sigma}_{\rm diff}U}\right)\left(\frac{S_n}{W_n}\right)\left(\phi_{ST}\frac{\zeta}{1.36\times10^{-17}}\right). \tag{3.12}$$

Electronic (Inelastic) Sputtering

Our methodology for determining the electronic sputtering rate coefficient ($k_{\rm es}$) is very similar to that for nuclear sputtering, with some nuclear terms replaced by electronic terms. We start with estimating electronic cross sections from electronic stopping powers. Similarly to the nuclear stopping power, we find an average elec-

tronic stopping power, weighted by the same cosmic ray energy distribution as nuclear sputtering, shown in Equation (3.8). This results in an average electronic stopping power of 1.131×10^{-15} eV per particle for the bombardment of water ice by H^+.

To convert electronic stopping powers to electronic cross sections, we simply divide the average stopping power by the average energy lost to the surface by ion-pair generation (W_e) and by the fraction of electronic energy lost through repulsive decay (f_e) (Brown et al., 1982; Schou, 1980). As far as we know, there is no comprehensive table of f_e terms, and these must be either estimated, or calculated for individual species. The product of $W_e \times f_e$ is also referred to as the average energy lost to thermal relaxation, or $\overline{\Delta E}$ (in eV) (Rook et al., 1985). The process results in an electronic cross section of 2.09×10^{-16} cm^2, using a W_e of 27 eV Shingledecker & Herbst (2018) and an f_e of 0.2 from Johnson & Brown (1982). All of these values are for amorphous water ice.

W_e is well known for a variety of species (Fueki & Magee, 1963) and can also be used to estimate cross sections from stopping powers for radiolysis reactions, as outlined in Shingledecker & Herbst (2018). Related to W_e, W_s, the average energy lost to sub-excitation electrons, may be a good estimate for $\overline{\Delta E}$, the average energy lost to thermal excitation, assuming most of the energy of the sub-excitation electrons is lost to the surface as heat. Therefore, if f_e is unknown, we can estimate the inefficiencies in energy transfer by using W_s. The terms are organized in Table 3.5, along with parameters needed for calculating electronic yields (Y_{es}),via the equation (Johnson, 1990)

$$Y_{es} \approx C_e \times (f_e^2)[(n_B^{-1/3})(n_B \times \bar{S}_e)/U]^2. \tag{3.13}$$

Table 3.5: Parameters for calculating electronic sputtering terms on amorphous solid water.

Parameter	Value	Reference
$\overline{S}_e$ (eV cm^2)	1.131×10^{-15}	This work
W$_e$ (eV)	27	(Shingledecker & Herbst, 2018)
f_e (Unitless)	0.20	(Johnson & Brown, 1982)
σ_{es} (cm^2)	2.09×10^{-16}	This work
$C_e \times (f_e^2)$ (Unitless)	8×10^{-4}	(Brown et al., 1980)
n$_B$ (cm^{-3})	3.3×10^{22}	(Brown et al., 1980)
U (eV)	0.49	Garrod & Herbst (2006)
Y_{es}	0.0045 H_2O per H^+	This work

Here C_e is an experimental unitless constant, while n_B (particles cm^{-3}) is used to approximate the average thickness of a monolayer of a surface species. The determined electronic sputtering yield is 0.0045 H_2O molecules per incident H^+ ion.

The final form of the rate coefficient for electronic sputtering is

$$k_{es} = Y_{es}\sigma_{es}\phi_{ISM}, \tag{3.14}$$

which, when fully expanded, takes the form:

$$k_{es}(s^{-1}) = \left(C_e \times f_e^2 \left[\frac{(n_B^{-1/3})(n_B \times \bar{S}_e)}{U} \right]^2 \right) \left(\frac{\overline{S}_e}{W_e f_e} \right) \left(\frac{\phi_{st}\zeta}{1.36 \times 10^{-17}} \right) \tag{3.15}$$

Carbon Dioxide and Mixed Ice Sputtering

For calculating the sputtering parameters for H^+ impacting CO_2 ice, chosen as a common ice constituent that isn't water, we will only calculate the electronic sputtering terms, as nuclear sputtering is significantly less effective, as shown in the earlier

Table 3.6: Parameters for CO_2 sputtering cross section and yield calculations

Parameter	Value	Reference
$\overline{S}_e$ (cm^2 eV)	2.329×10^{-15}	This work
W_e (eV)	34.2	(Johnson & Brown, 1982)
f_e (Unitless)	0.19	(Johnson & Brown, 1982)
$\sigma_{\rm es}$ (cm^2)	3.58×10^{-16}	This work
$C_e \times f_e^2$ (Unitless)	1×10^{-3}	(Brown et al., 1982)
$n_{\rm B}$ (cm^{-3})	2.3×10^{-22}	(Johnson, 1990)
U (eV)	0.22	(Garrod & Herbst, 2006)
Y_{es}	0.073 CO_2 per H^+	This work

calculations for water ice. The process is the same for water ice, outlined in the previous section, with constants and important terms used displayed in Table 3.6. Using Equation 3.8 for the range of $S(E)$ CO_2 values results in an average electronic carbon dioxide stopping power of 2.329×10^{-15} eV cm^2. Dividing $\overline{S}_e$ by a W_e of 34.2 eV and the f_e of 0.19 (Johnson & Brown, 1982), we obtain the electronic sputtering cross section for CO_2 of 3.58×10^{-16} cm^2. Applying CO_2 values in Table 3.6 to Equation 3.13 returns a sputtering yield of 0.073 carbon dioxide molecules per incident hydrogen ion. The higher yield for carbon dioxide ice compared to water ice is due to carbon dioxide ices' cross section being greater than water ice, and a significantly lower binding energy of carbon dioxide ice.

Our mixed ice model for sputtering simply adjusts the rate coefficient for sputtering based on the fractional amounts of water and CO_2 ice within the model, which leads to the following formula for any species of ice, N_i:

$$k_{es}^{\rm mix} = \left(k_{es(\rm H_2O)} \frac{N_{\rm H_2O}}{N_{\rm H_2O} + N_{\rm CO_2}}\right) N_i + \left(k_{es(\rm CO_2)} \frac{N_{\rm CO_2}}{N_{\rm H_2O} + N_{\rm CO_2}}\right) N_i. \quad (3.16)$$

This treatment of a mixed ice is simplistic, as we do not account for mixed ice yields,

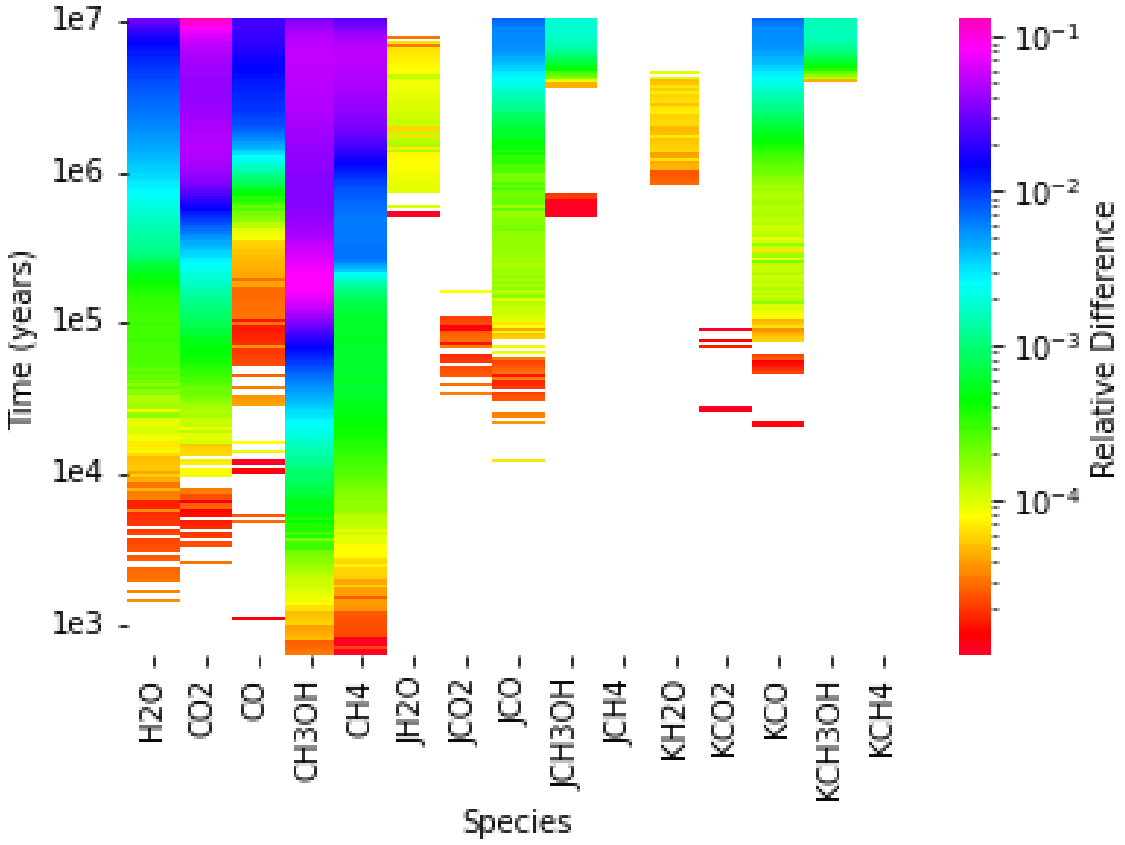

Figure 3.3: Heatmaps comparing models 1H and 2HS; each heatmap has model time on the y axis, with various species on the x axis. Species with a "J" designation represent surface ices, or a "K" for bulk ices. The different colours on the heatmap represent relative differences in abundance between models. Note the different colour bar scales and ranges

binding energies, or stopping powers, all of which will vary from a single species ice.

3.3 Results and Analysis

We utilize a series of low temperature models with various combinations of cosmic ray sputtering, cosmic ray whole grain heating, and cosmic ray induced diffusion described in Table 3.3. We model the physical conditions based on the cold molecular

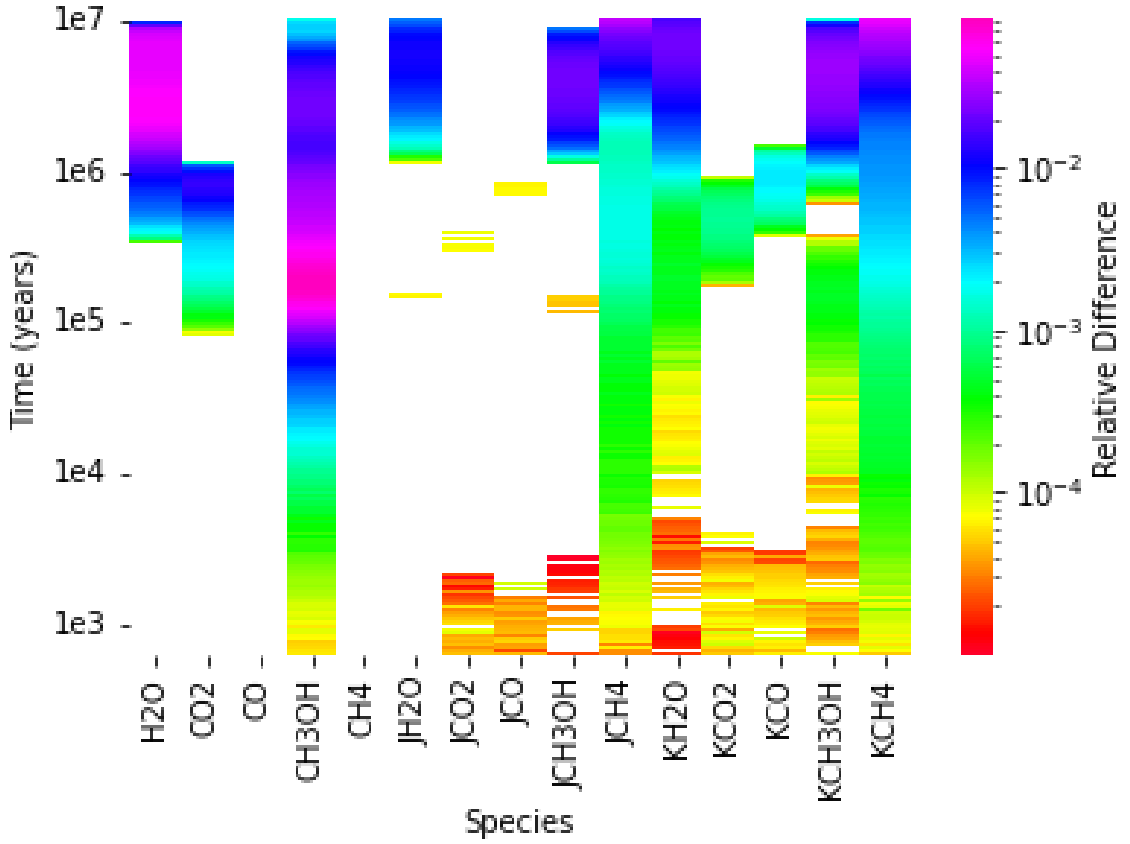

Figure 3.4: Heatmaps comparing models 1H and 3S; each heatmap has model time on the y axis, with various species on the x axis. Species with a ”J” designation represent surface ices or a ”K” for bulk ices. The different colours on the heatmap represent relative differences in abundance between species in the compared models. Note the different colour bar scales and ranges

core TMC-1, where the initial abundances are compiled in Table 3.1, and relevant physical conditions are displayed in Table 2.2. The standard "reference" model is designated 1H, a basic model with the same chemical network as in Paulive et al. (2021), without radiolysis chemistry. Models with an "H" after the number have cosmic ray whole grain heating, an "S" if sputtering is on, based on the theory in Section 3.2.2 for water ice, a "C" for sputtering based on CO_2 ice, and an "M" for the mixed ice models. The chemical networks for all models examined for these and all other models in this chapter are the same. All models that have CRH allow for periods of time where the temperature of the grain ices is temporarily increased to simulate the heating from cosmic rays, followed by cooling back to ambient temperatures as volatile species, such as CO, are thermally desorbed, as shown in Hasegawa & Herbst (1993). The rate coefficient for thermal desorption is the vibrational frequency of a species, $v_\circ$, multiplied by the negative exponent of the binding energy in kelvin, divided by the ambient dust temperature, resulting in a rate coefficient of

$$k_{\rm td} = v_\circ \exp\left(-\frac{E_{\rm b}}{T_{\rm dust}}\right). \tag{3.17}$$

This is the same equation used to calculate the CRH rate coefficient, however, the ambient dust temperature is changed to the increased temperature used for CRH, in this case 70 K. This increased temperature results in an increase in desorption rate of e^7 s^{-1} compared to the thermal desorption rate at the dark cloud ambient dust temperature of approximately 10 K.

3.3.1 Water Ice Models

As an introduction, we examine the differences in the time-dependent results between the fiducial model (1H) with models 2HS and 3S. These non-fiducial models both include sputtering, while 2HS contains cosmic ray heating in addition to sputtering.

Figures 3.3 and 3.4 show multiple heatmaps of a suite of common interstellar molecules found in TMC-1. The colour gradient on the heatmap shows the relative difference in molecular abundance between a species for a model with respect to the base model 1H, and the model to which it is being compared. The relative difference between two numbers X and Y can be defined by the ratio (Y-X)/X, where X applies to base model species and Y refers to other models such as 2HS and 3S. If Y is much larger than X, the relative difference approaches Y/X.

In Figure 3.4, the relative difference ranges from 10^{-1} to 10^{-4}, where a relative difference of 1 represents a species with an abundance of Y that is double the abundance X in the base sputtering model. Likewise, a relative difference of 10^{3} would mean an abundance in model 2HS or 3S 1000 times the base model abundance, while a relative difference of 10^{-4} would be only signify an abundance 1.0001 times the abundance in model 1H. The white space within a heatmap signifies that there is no change in abundance between the two models at the given time.

Specifically, for Figure 3.3, these species are mostly abundant gas phase species within cold dark clouds , and we do not see differential large changes in their abundances, as they are generally efficiently produced in the gas phase, and while they could have efficient grain production pathways, the gas phase routes still dominate, or they are adequately desorbed from the grain surface with thermal and non-thermal methods. Looking at gas-phase CO, we see that there is an approximate 1% increase toward the

end of the model, as CO is often depleted onto grain surfaces at later times. With the addition of sputtering, we increase the amount of desorbed CO, resulting in slightly higher gas phase abundances.

There are similar results for the comparison between 1H and 3S, shown in Figure 3.4, with minor differences: there is less of an increase in abundance in general, which is expected, because, unlike model 2HS, model 3S lacks cosmic ray whole grain heating. The lack of heating causes a lower desorption rate, which leads to the lower gas-phase abundance. In addition, the greater abundances in model 3S compared with 1H indicate that compared to whole grain heating already implemented in Nautilus, which temporarily heats the entirety of grain ices to 70 K, sputtering is generally more effective for desorbing low abundance species from the grain surface, and the bulk ice. This is due to sputtering allowing desorption directly from the bulk of the ice more readily than thermal evaporation, and thermal evaporation following CRH, as there is less of a chance that the ejected species can get trapped by the upper layers of ice from physical changes in the ice following ion bombardment.

Another contributing factor for the difference in abundances of models with solely CRH or sputtering is the relatively short time of increased thermal temperature from whole grain heating, which is on the order of 10^{-5} seconds, or the approximate time CO needs to thermally desorb from an ice surface (Hasegawa & Herbst, 1993). During the duration of increased temperature, not all species are able to efficiently desorb at 70 K, but the more volatile CO is mostly desorbed from a surface in the time period of 10^{-5} seconds (Hasegawa & Herbst, 1993). CO, and other species that are able to significantly contribute to desorption at 70, then cool the surface to the ambient 10 K. There is no equivalent duration or limitation on what species are effectively removed by sputtering, save for the cosmic ray-grain encounter rate.

In Figure 3.5 we show the modeled fractional abundance against time using the models 1H, 2HS, and 3S for a variety of COMs detected toward TMC-1. The models are represented by dashed lines, solid lines, and dotted dashed-lines for models 2HS, 1H, and 3S respectively. The molecules examined are methanol (CH_3OH), acetaldehyde (CH_3CHO), methyl formate ($HCOOCH_3$), glycolaldehyde ($HCOCH_2OH$), and dimethyl ether (CH_3OCH_3. All fractional abundances mentioned in this chapter are with respect to H_2. The molecules, which will be discussed later, have binding energies that prevent them from being efficiently desorbed either at the nominal 10 K, or 70 K in models with CRH. There are little to no differences in the abundances of methanol, acetaldehyde, and dimethyl ether among models 1H, 2HS, and 3S at most times. However, there is an increase in abundance by more than a factor of 2, for methyl formate at 5×10^5 yr between model 1H and models 2HS and 3S. There is also an increase in gas-phase glycolaldehyde by less than a factor of 2 at the same time.

3.3.2 Carbon Dioxide Ice Models

Table 3.6 shows relevant parameters used in calculating yields based on carbon dioxide sputtering. We examine the same suite of molecules as in the previous section, shown in Figures B.1 and 3.6. Figure B.1 show a sample of common interstellar ices and simple molecules found within the ice. Notably, the addition of sputtering does not significantly alter the bulk or surface abundances of the species. This suggests that sputtering does not remove enough material to leave the grain barren of ice when coupled with previously examined thermal, chemical, and photo-desorption methods for these common species at 10 K.

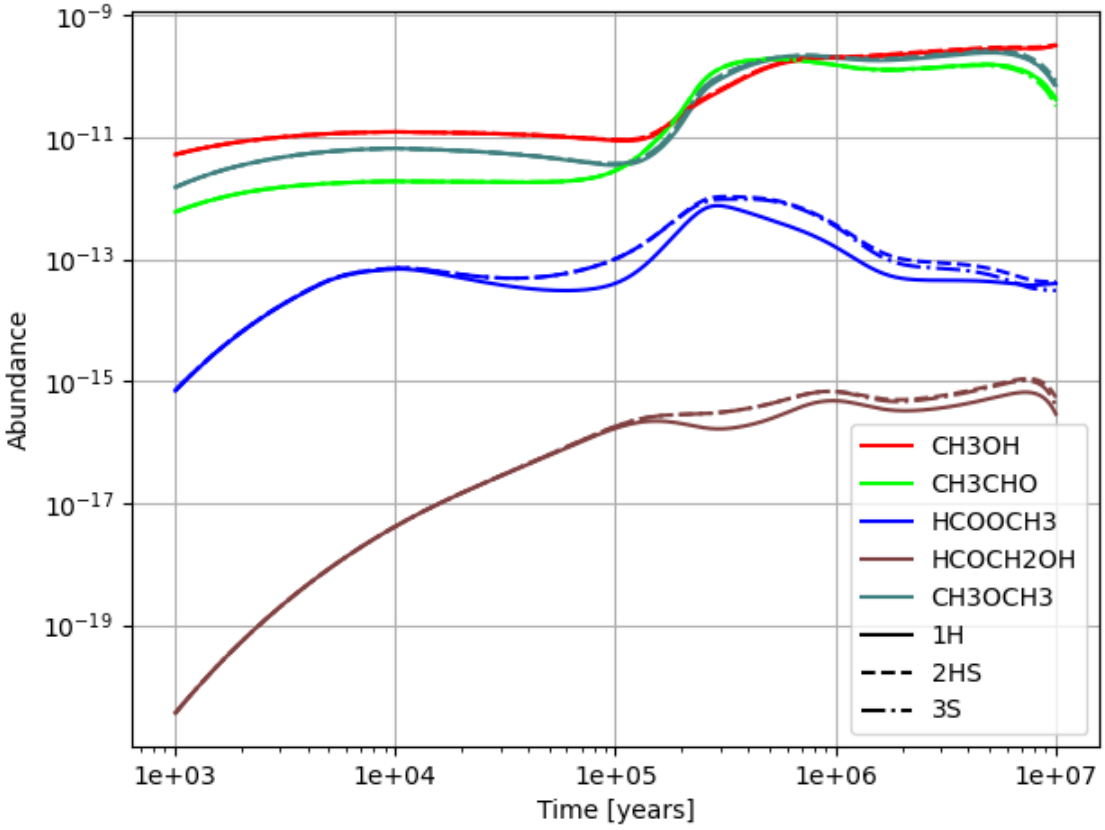

Figure 3.5: Modeled fractional abundance of relevant COMs under cold dark cloud conditions at 10 K. Models 2HS and 3S have water ice sputtering rates of 2.55×10^{-18} cm^{-3} s^{-1} at 5×10^5 yr. The dashed line is model 2HS, the solid line is model 1H, the dotted-dashed line is model 3S. All COMs examined for this graph are gas-phase. Both sputtering models show increases in abundances for methyl formate and glycoaldehyde.

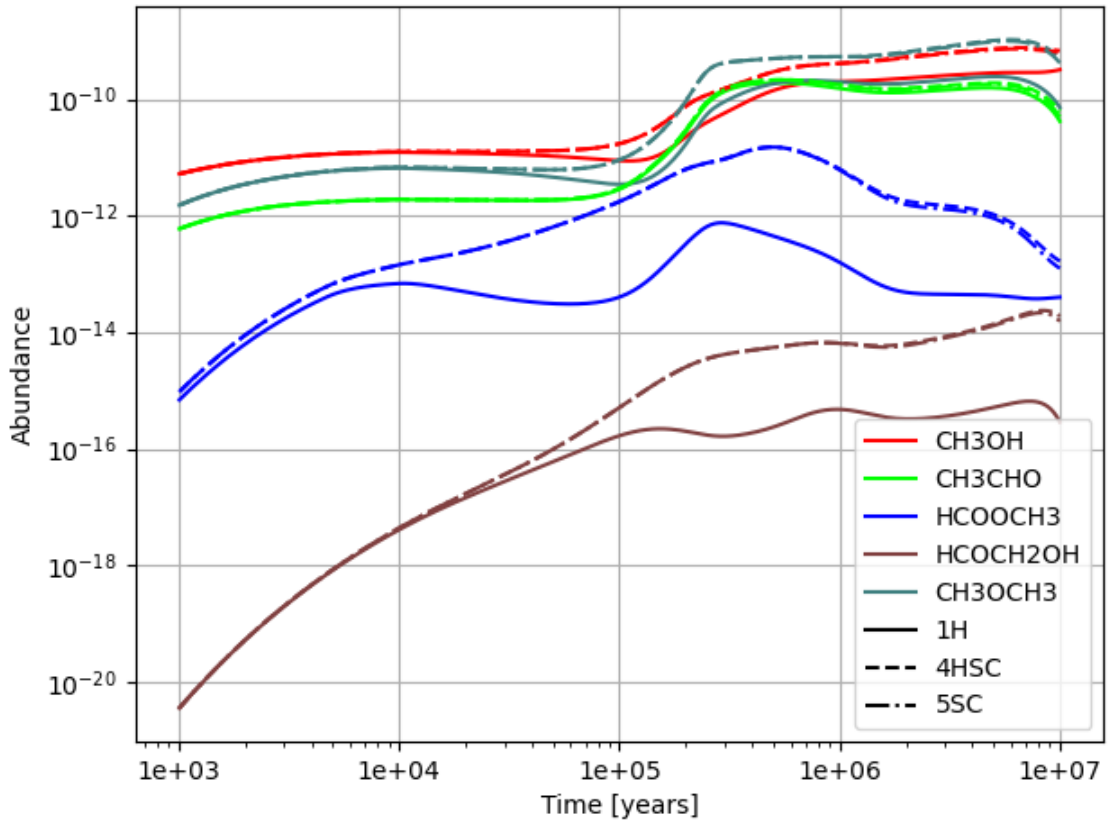

Figure 3.6: Gas-phase fractional abundances of select COMs with respect to hydrogen. Models 4HSC and 5SC have carbon dioxide ice sputtering rates of 1.48×10^{-16} cm^{-3} s^{-1} at 5×10^5 yr. Different colors represent different species. The fiducial model (1H) has a solid line, the model with carbon dioxide sputtering and heating (4HSC) a dashed line, and the model with just sputtering is has a dotted and dashed line (5SC). All molecules presented here show increases of varying degrees in gas-phase abundances, with acetaldehyde (CH_3CHO) showing less of an increase (a factor of 1.12) compared with other COMs when comparing abundnances between the models with sputtering and the fiducial model.

In contrast, Figure 3.6 shows significant increases in gas-phase abundances of the species presented in the figure for both models that include sputtering. Slight differences, especially at later times in the model, become apparent, with model 4HSC (Both sputtering and cosmic ray heating) slightly outproducing glycolaldehyde ($HCOCH_2OH$) and methyl formate ($HCOOCH_3$) compared to model 5SC (sputtering, no CRH).

Overall, we find significant differences between sputtering at carbon dioxide rates and water rates, partially due to higher yields and larger cross sections, leading to faster sputtering and greater amounts of desorption. Figure 3.6 shows increases of varying magnitude for COMs, where acetaldehyde has the lowest increase in magnitude by a factor of 1.12, while methyl formate and glycolaldehyde see increases by factors of 33 and 24, respectively. These increases contrast with our water sputtering models that only show increases in methyl formate and glycolaldehyde by an approximate factor of 2. For the other two examined COMs, methanol and dimethyl ether, we see increases by factors of 2.1 and 2.7, respectively, at the time 5×10^5 yr.

3.3.3 Mixed Ice Models

The models containing the mixed ice sputtering rates (Equation 3.16) are labelled 6HSM and 7SM, where both include mixed ice sputtering rates while only 6HSM has whole grain cosmic ray heating. Figures 3.7 and B.2 shows similar curves to the carbon dioxide ice sputtering results, with slight variation in most common and simple ice species, albeit to a lesser extent than the carbon dioxide sputtering models. Similar to previous results, the mixed ice has desorption rates that vary based on the ratio of carbon dioxide to water ice which results in gas-phase abundances between those of pure water ice and pure carbon dioxide ice sputtering. Figure 3.8 shows

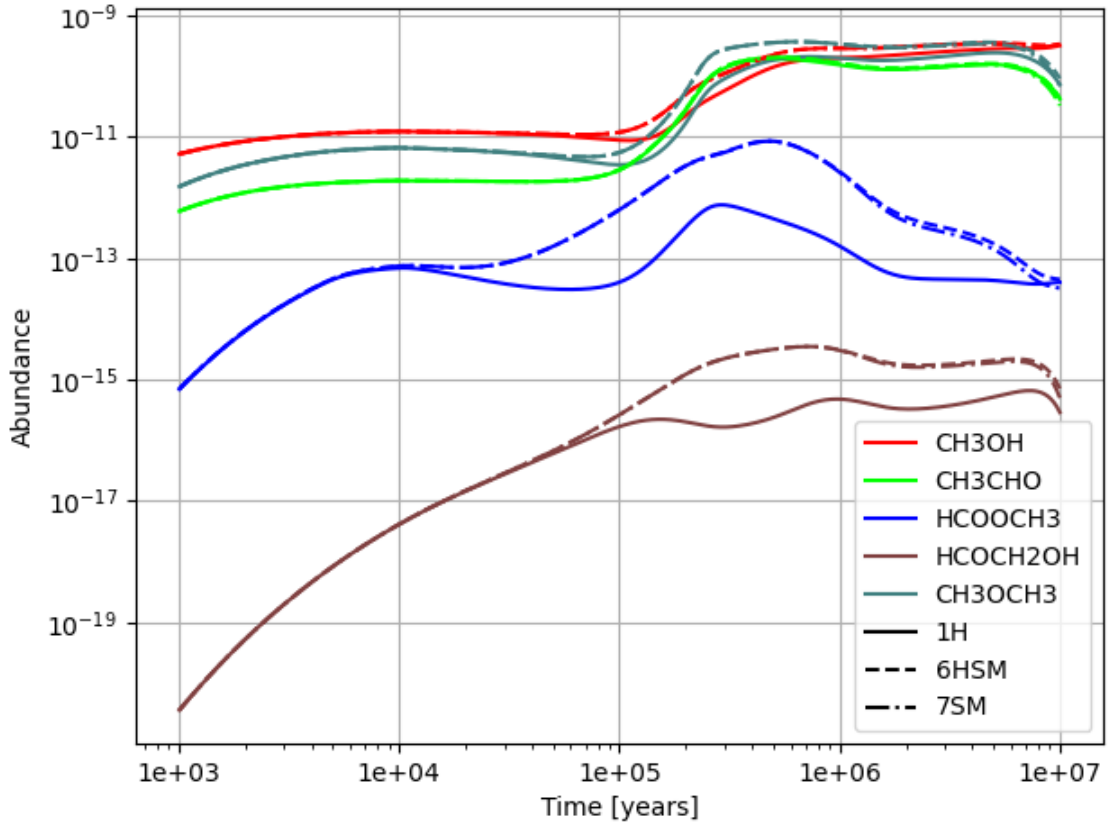

Figure 3.7: Gas-phase fractional abundances of select COMs with respect to hydrogen. Models 6HSM and 7SM have mixed water and carbon dioxide ice sputtering rates of 7.02×10^{-17} cm^{-3} s^{-1} for water and 8.21×10^{-17} cm^{3} s^{-1} for carbon dioxide at 5×10^{5} yr. Different colors represent different species, the fiducial model (1H) is a solid line, the model with carbon dioxide sputtering and heating (6HSM) is dashed, the model with pure sputtering is dotted and dashed (7SM). All molecules presented here show increases of varying degrees in gas-phase abundances, with the acetaldehyde (CH_3CHO) showing less of an increase compared to other COMs.

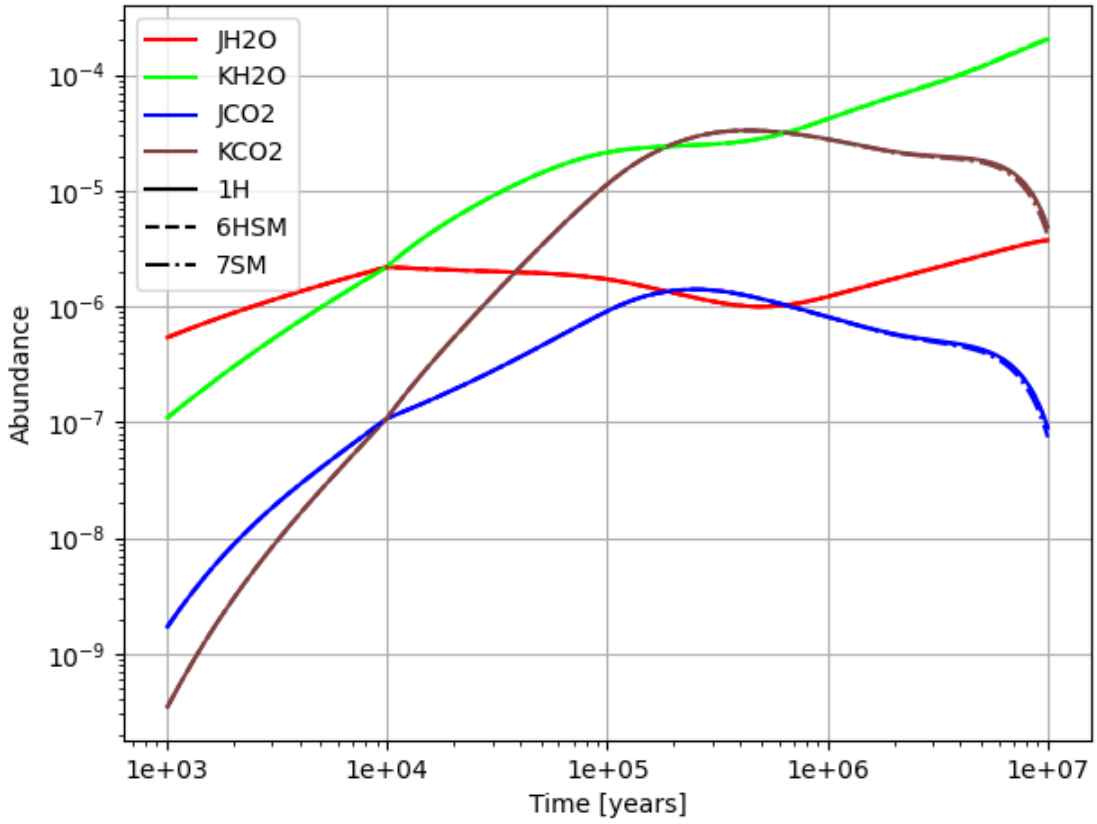

Figure 3.8: Grain surface and mantle abundances of water ice and carbon dioxide ice, for models 1H, 6HSM, and 7SM. Other models used in this work differ in water and carbon dioxide fractional abundance by 10% at most. The models from 1×10^3 yr and 1×10^6 yr have differences by factors of 0.0001, or approximately 0.01%.

the difference in abundance of mantle and surface water ice and carbon dioxide ice in models 1H, 6HSM, and 7SM. The differences between ice abundances in the models is approximately 0.01% for most times. There are no new notable results that have not been discussed in the two previous sections, apart from slightly different peak abundances for the examined COMs, shown in Figure 3.7; these results will be further discussed in the next section, where we compared modeled abundances to observations.

3.4 Astrochemical Implications

Table 3.7: List of observed column densities and estimated fractional abundances for examined COMs in TMC-1 methanol peak (MP) and cyanopolyyine peak (CP). Column densities are in cm^{-2}, while fractional abundances are with respect to hydrogen, and unitless.

TMC-1				
Molecule	Column Density (CP)	Abundance (CP)	Column Density (MP)	Abundance (MP)
Methanol (CH_3OH)	$(1.7 \pm 0.3) \times 10^{13}$	$(1.7 \pm 0.3) \times 10^{-9}$	$(4.0 \pm 1.4) \times 10^{13}$	$(4.0 \pm 1.4) \times 10^{-9}$
Acetaldehyde (CH_3CHO)	$(3.5 \pm 0.2) \times 10^{12}$	$(3.5 \pm 0.2) \times 10^{-10}$	$(3.4 \pm 0.4) \times 10^{12}$	$(3.4 \pm 0.4) \times 10^{-10}$
Methyl Formate ($HCOOCH_3$)	$(1.1 \pm 0.2) \times 10^{12}$	$(1.1 \pm 0.2) \times 10^{-10}$	$(1.9 \pm 0.2) \times 10^{12}$	$(1.9 \pm 0.2) \times 10^{-10}$
Dimethyl Ether (CH_3OCH_3)	$(2.5 \pm 0.7) \times 10^{12}$	$(2.5 \pm 0.7) \times 10^{-10}$	$(2.1 \pm 0.7) \times 10^{12}$	$(2.1 \pm 0.7) \times 10^{-10}$

Estimated hydrogen column density is 10^{22} cm^{-2}. All column densities are from Soma et al. (2018), except for methyl formate and dimethyl ether at the cyanopolyyine peak (Agundez et al., 2021) and acetaldehyde at the cyanopolyyine peak (Cernicharo et al., 2020).

Table 3.8: List of modeled peak fractional abundances for select COMs, distinguished by model.

Molecule	1H	2HS	3S	4HSC	5SC	6HSM	7SM	8HSC10
Methanol	2.8×10^{-10}	3.0×10^{-10}	2.9×10^{-10}	7.6×10^{-10}	7.3×10^{-10}	3.5×10^{-10}	3.4×10^{-10}	7.8×10^{-9}
Acetaldehyde	1.9×10^{-10}	1.9×10^{-10}	1.9×10^{-10}	2.1×10^{-10}	2.1×10^{-10}	2.0×10^{-10}	2.0×10^{-10}	7.1×10^{-10}
Methyl Formate	7.5×10^{-13}	1.1×10^{-12}	9.5×10^{-13}	1.5×10^{-11}	1.5×10^{-11}	8.5×10^{-12}	8.5×10^{-12}	1.7×10^{-10}
Dimethyl Ether	2.4×10^{-10}	2.7×10^{-10}	2.6×10^{-10}	1.0×10^{-9}	1.0×10^{-9}	3.7×10^{-10}	3.7×10^{-10}	2.1×10^{-8}

Comparing the results of the various models to astronomical observations, we find mixed results: most models without sputtering do not produce enough gas-phase molecules, and while sputtering does adequately increase the gas-phase abundance to observed abundances in some cases, though the faster sputtering models are not enough to adequately reproduce abunandances for other molecules. Soma et al. (2018) reported column densities of methanol, dimethyl ether, and acetaldehyde at the cyanopolyyne peak (referred to as TMC-1 CP) as approximately 1.7×10^{13}, 4.6×10^{12} and 2.0×10^{12} cm^{-2}, respectively. They also report methanol peak (TMC-1 MP) column densities of methanol, acetaldehyde, methyl formate, and dimethyl ether as 4.0×10^{13}, 3.4×10^{12}, 1.9×10^{12}, and 2.1×10^{12} cm^{-2}, respectively. Agundez et al. (2021) provides column densities for methyl formate and dimethyl ether toward TMC-1 CP of 1.1×10^{12} and 2.5×10^{12} cm^{-2}, respectively, while Cernicharo et al. (2020) provides an updated column density for cyanopolyyine peak acetaldehyde of 3.5×10^{12} cm^{-2} Dividing these column densities by an approximate molecular hydrogen column density of 10^{22} cm^{-2} in TMC-1 yields fractional abundances of the examined molecules. The observed values used here are organized in Table 3.7, while peak modeled abundances are in Table 3.8.

This results in an observed fractional abundance for methanol of 1.7×10^{-9} toward TMC-1 CP, and an abundance of 4.0×10^{-9} at TMC-1 MP. Compared with the peak abundances of methanol in model 1H of approximately 2.8×10^{-10}, we significantly under-produce methanol in TMC-1 by an approximate order of magnitude, at least in the gas phase. Our sputtering models have a peak gaseous abundance of 3.0×10^{-10} in model 2HS, and 7.6×10^{-10} in model 4HSC, both at times from 5×10^5 until 7×10^6 yr. Our mixed ice model is not as effective as the carbon dioxide ice, with a peak abundance of 3.5×10^{-10}. These results agree with the generally accepted

methanol production method of hydrogenation of carbon on grain surfaces, because the inclusion of sputtering desorbs methanol already made, yet stuck within the grain ices, to better match observed abundances (Watanabe & Kouchi, 2002; Fuchs et al., 2009). The models suggest that faster sputtering is needed to reproduce the observed abundances in TMC-1 MP because the mixed ice and water ice sputtering rate models still under-produce methanol by factors of 11.5 and 13, respectively, when comparing peak abundances. In contrast, CO_2 sputtering seems to produce and desorb enough CH_3OH to match peak abundances in TMC-1 CP within a factor of 2.5 lower than the observed abundance, despite still under-producing methanol for TMC-1 MP by a factor of 5.3.

Acetaldehyde is an order of magnitude less abundant compared to methanol at both peaks, with peak observed abundances of 3.5×10^{-10} at TMC-1 CP (Cernicharo et al., 2020) , and 3.4×10^{-10} toward the methanol peak. Our modeled abundances for acetaldehyde are 1.9×10^{-10} for the standard heating model of 1H. For models including sputtering, the abundances are as follows: model 2HS has a peak abundance of 1.9×10^{-10}, model 4HSC peaks at 2.1×10^{-10} and model 6HSM peaks at about 2.0×10^{-10}, with the faster carbon dioxide ice sputtering and heating better matching the observed abundances of the CP. While the base model is within a factor of 1.9 to the peak abundances toward TMC-1 CP, this model also under-produces such abundances for TMC-1 MP by a factor of 1.8; sputtering partially accounts for the difference for TMC-1 MP, but is less than the observed abundance by a factor of 1.6. The calculated peak abundances occur at approximately 5×10^5 yrs, with another peak of similar abundances occur at approximately 6×10^6 yrs in all models examined in this chapter, and are shown in Figures 3.5, 3.6, and 3.7.

The observations for methyl formate have the fractional abundance at 1.9×10^{-10},

toward the TMC-1 MP. Model 1H calculates the peak fractional abundance as 7.5×10^{-13}, significantly lower than the observed amount by over two orders of magnitude. The models with sputtering come closer to replicating the observed abundance, but still under-produce methyl formate in the gas phase by an approximate order of magnitude, with model 4HSC just reaching 1.5×10^{-11}. The mixed-ice and water models produce less methyl formate, producing peak amounts of 8.5×10^{-12} and 1.1×10^{-12}, respectively. All models predict the peak of methyl formate to be at a similar time of 5×10^5 yrs, much like the other molecules highlighted in this section. Recent observations by Agundez et al. (2021) have detected methyl formate toward TMC-1 CP, with a column density of $(1.1 \pm 0.2) \times 10^{12}$ cm^{-2}, and a fractional abundance of 1.1×10^{-10}. The results comparing the models to these observed amounts match the discrepancies between the models and the observed abundances in TMC-1 MP. Methyl formate has also been examined in cold dark clouds using radiolysis models, such as in Shingledecker et al. (2018), where gas-phase methyl formate production was found to be greatly enhanced with the inclusion of radiolysis chemistry and suprathermal reactions. It may be possible to combine the enhanced grain ice abundances of ices in general, and efficiently desorb them using sputtering, as a future possibility.

Dimethyl ether is reported to have an upper limit to the fractional abundance of 4.6×10^{-10} toward the cyanopolyyine peak, and an observed fractional abundance of 2.1×10^{-10} toward the methanol peak (Soma et al., 2018). In the same publication for methyl formate detection toward the cyanopolyyine peak, Agundez et al. (2021) report a column density of $(2.5 \pm 0.7) \times 10^{12}$ cm^{-2}, for a fractional abundance of $(2.5 \pm 0.7) \times 10^{-10}$. All models reach peak abundance at approximately 6×10^6 yrs. Model 4HSC produces the most dimethyl ether, reaching just above 1×10^{-9}, while 2HS and 6HSM have peak abundances at 2.7 and 3.7×10^{-10} respectively. However,

at a time of 5×10^5 yrs, which is similar to other peak times that match observations of molecules discussed earlier in the section, the modeled abundances are lower by a factor of approximately 2 than later in the model. 1H produces 2.0×10^{-10}, with 4HSC producing approximately 5×10^{-10} dimethyl ether. Models 2HS and 6HSM produce abundances of 2.2×10^{-10} and 3.6×10^{-10} respectively at 10^5 yrs. Models 4HSC and 5SC produce dimethyl ether within a factor of 4 toward both peaks of TMC-1, at peak abundances, with the other models all producing dimethyl ether within a factor of 1 at peak abundances. The carbon dioxide ice models more closely match observations at times around 5×10^5 years, within a factor of 2 for the cyanopolyyine peak, and more than 2 for the methanol peak.

Overall, the model that best fits the observed abundances for COMs in TMC-1 is either 4HSC or 5SC, despite under-producing methanol values for the MP by a factor of five. We came closer to replicating methanol values for the CP, only under-producing them by a factor of 2. For acetaldeyhde, all models match the observations for the CP, approximately 2×10^{-10}.For methyl formate at the MP, the carbon dioxide ice models under-produce methyl formate by a factor of 10, with other models under-producing methyl formate by a larger factor. At TMC-1 CP, models 4HSC and 5SC also under-produce methyl formate by an order of magnitude. Finally, the upper limit of observed dimethyl ether toward the CP are less than peak amounts in models 4HSC and 5SC by a factor of 2. The peaks of other models are below the upper limit of dimethyl ether observed in the CP, while slightly overproducing dimethyl ether compared with the observed abundance in the MP by a factor of 2. The models with sputtering rates based on carbon dioxide ices consistently under-produce the observed molecules examined in this chapter, and their calculated abundances seem to best replicate the abundances found toward the TMC-1 CP.

These COMs can be compared with observed abundances for other environments in the ISM: the cold dense core B1-b, the dense core L483, the prestellar core L1689B, and the molecular cloud Barnard 5, as listed in Appendix B, Tables B.1, B.2, B.3, and B.4. These environments have slightly different initial abundances and conditions compared with TMC-1, though the model parameters remain the same. Comparing modeled abundances with the observed abundances, we see that our variety of models does not adequately replicate methanol abundances in most environments. The observed methanol abundances range from 1.2×10^{-9} in L1989B, to 4.5×10^{-8} toward Barnard 5. However, the abundances of the other molecules examined are relatively well matched at peak, or near-peak abundances.

To compare methanol fractional abundances to the approximate observed levels in all sources would require the rate coefficient for sputtering to be increased by approximately a factor of ten. We have run a supplementary model (8HSC10) with such an increase, and have included the figures presenting the fractional abundances for ten times the sputtering rate in Appendix B, Figure B.3. Notable in this model is that the abundance of dimethyl ether is greatly increased, to a greater fractional abundance than that of methanol, which is not observed in any of the sources mentioned previously. However, at this enhanced rate of sputtering, peak modeled methanol abundances match observed abundances well. This suggests that while sputtering rates greater than the ones presented here may be physical, there need to be further studies into modeling the production and destruction of the molecules highlighted here, especially methanol and dimethyl ether, and further examinations of sputtering.

3.5 Conclusions

We present in this chapter a way of both estimating and implementing theoretical sputtering parameters into a rate-equation based model of cold dark clouds. We show that sputtering is an effective way of desorbing multiple species off of grain surfaces, even at slow sputtering rates. While there are experimental results that can be included in models, it is more difficult to obtain experimental data that match the mixture of amorphous ices that populate grain surfaces in the ISM. Fortunately, there are theoretical treatments of sputtering ices that seem to be reasonably effective. While further experimental work will need to be done to provide a basis for the sputtering of mixed ices by lighter ions, both current theory and experimental results suggest that sputtering is important as a method of non-thermal desorption in astrochemical models, similar to reactive desorption and photodesorption. Even when coupled with cosmic ray heating, a widely used "thermal" method of temporarily increasing thermal desorption, many species are not excessively depleted from within the ice, nor excessively ejected into the gas phase. In addition, in cases where there are efficient gas destruction pathways, sputtering does not overcome multiple efficient gas phase destruction routes. To adequately match abundances using sputtering alone, the rate coefficient for sputtering will need to be increased by a factor of approximately 10, however, this causes overproduction of multiple molecules including dimethyl ether and acetaldehyde. Further examination of gas and grain destruction pathways is warranted, should sputtering become commonplace in models.

Chapter 4

Radiolysis and Sputtering of Naphthalene and Precursors

4.1 Introduction

Polycyclic aromatic hydrocarbons, or PAHs, are a class of molecules characterized by multiple ring structures stabilized by aromatic resonance. PAHs are thought to be ubiquitous throughout the interstellar medium (ISM), however, the chemistry behind their production has long been contested (Tielens, 2008). There are two main proposed mechanisms for the production of PAHs; the top-down approach, where large PAHs are formed in warm environments in the ISM, eventually ejected, and are broken down to smaller PAHs, like naphthalene ($C_{10}H_8$), through chemical reactions and photo-processes (Berné et al., 2015). The bottom-up approach takes the opposite route: rings are formed over time through expansion of carbon chain chemistry, initially from atomic carbon (Jones et al., 2011; Woods et al., 2002).

Recent detections of benzonitrile (c-C_6H_5CN), 1-cyanonaphthalene ($C_{10}H_7CN$), 2-cyanonaphthalene ($C_{10}CNH_7$), and indene (c-C_9H_8) toward the cold dark cloud TMC-1 are major steps in understanding the aromatic chemistry in the formation and destruction of PAHs in the ISM (McGuire et al., 2018, 2021; Burkhardt et al., 2021), as these molecules are chemically related to benzene (c-C_6H_6) and naphthalene. While

benzene and benzonitrile are not PAHs (they are single ring structures), they are thought to contribute to the formation of PAHs, possibly through benzene radicals that have had hydrogens removed (Krasnokutski et al., 2017; Kaiser et al., 2003; Hewage et al., 2012). Unfortunately, modeling efforts have fallen short to replicate the observed abundances of both benzonitrile and cyanonaphthalenes, where the modeled abundance for benzonitrile is about a fourth of the observed value, and observations are multiple orders of magnitude more than both modeled cyanonaphthalene isomers. (McGuire et al., 2018, 2021). Currently, chemical networks utilized in models show that benzene is produced primarily in the gas phase, with very few surface reactions, utilizing the "bottom-up approach" according to both the KIDA and UMIST chemical networks (Wakelam et al., 2012). The two gas-phase reactions that primarily produce benzene in McGuire et al. (2018) are the electron recombination reaction of protenated benzene cation forming beznene and a hydrogen atom,

$$C_6H_7{}^+ + e^- \rightarrow C_6H_6 + H, \tag{4.1}$$

and the reaction of ethyl radical (C_2H) with 1,3-butadiene ($CH_2CHCHCH_2$), forming benzene and a hydrogen atom,

$$C_2H + CH_2CHCHCH_2 \rightarrow C_6H_6 + H. \tag{4.2}$$

These formation routes to benzene then lead to the sole production route of benzonitrile included in McGuire et al. (2018) where benzene reacts with cyano radical (CN),

$$CN + C_6H_6 \rightarrow C_6H_5CN + H. \tag{4.3}$$

However, as previously mentioned, this pathway under-produces benzonitrile by a factor of 0.25 and is lacking chemical reactions that may occur on the grain surface, which may be enough to enhance the abundance of benzene or benzonitrile sufficiently to reduce the deficit in modeled production. One such example of a grain reaction is the irradiation of three acetylene (C_2H_2) ices, leading to benzene (Zhou et al., 2014).

One way that energetic ices can be produced in the ISM is through cosmic rays; high energy nuclei, generally protons, travelling at significant fractions of the speed of light (Blasi, 2013). When these particles collide with gas and ice in the ISM, there are massive energy transfers, broadly split into two categories, based on the type of collision: elastic collisions, also called nuclear collisions, and inelastic collisions, or electronic collisions (Spinks & Woods, 1990; Johnson, 1990). Electronic collisions contribute to radiolysis chemistry, chemical reactions occuring from ionizations and excitations along the path of the comsic ray. Both electronic and nuclear collisions contribute to sputtering, when particles are ejected from a surface as a result of the high energy collisions, of which there are experiments and models based on experiments of heavy ions impacting amorphous and crystalline water ices (Dartois et al., 2015b, 2018; Wakelam et al., 2021).

There are potentially other energetic chemical pathways on surfaces that have yet to be studied that can lead to the production of the molecules mentioned earlier, particularly through suprathermal nitrogen chemistry. Alternatively, recent works such as Ioppolo et al. (2021) show that there are nitrogen-bearing COM surface formation pathways that are efficient at 10 K and that are not reliant on energetic chemistry.

Despite these results, surface radiolysis chemistry and suprathermal reactions, first included in rate-equation based models in Shingledecker & Herbst (2018), improved the modeled abundance of a suite of oxygen-bearing COMs (Shingledecker et al., 2018; Paulive et al., 2021). By applying radiolysis to nitrogen species on the surface, such as HCN, HNC, and H_2CN it is possible to also increase the gas-phase abundances of these detected species.

Further inadequacies of the current chemical networks for chemical modeling are becoming more apparent with the detection of other molecules, thought to be precursors to PAHs, toward TMC-1. For example, a non-functionalized hydrocarbon cycle, benzyne (o-C_6H_4) was observed toward TMC-1 in Cernicharo et al. (2021b). Also toward TMC-1, vinyl acetylene (CH_2CHC_2H) and HC_4N were observed (Cernicharo et al., 2021a). Agúndez et al. (2021) discovered propargyl radical (CH_2CCH) also toward TMC-1, proposed to be able to self react in the gas-phase to form benzene (Caster et al., 2021). Cyanovinyl acetylene (C_4H_3CN) was also recently discovered toward TMC-1 (Lee et al., 2021). Many included modeling efforts in these papers failed to replicate observed abundances, or were gas-phase only models.

This chapter will focus on updating the KIDA-based chemical network to account for these recent discoveries, through gas-phase reactions, grain surface reactions, sputtering, and radiolysis, with the purpose to better replicate observed abundances. Throughout the chapter, the same set of molecules will be examined, as precursor species for "bottom up" production of PAHs: acetylene, vinyl acetylene, propargyl radical, benzene, naphthalene, and their cyano counterparts: cyanovinyl acetylene, cyanopropargyl radical, benzonitrile, and 1-cyanonaphthalene.

4.2 Models and Methods

The chemical model used in this chapter is the three-phase rate equation-based program `Nautilus-1.1` (Wakelam et al., 2012). The three phases are composed of the gas, the top two monolayers of the modeled grain ices, called the surface, and the remaining ice on the dust grain mantle, called the bulk. This distinction between surface and bulk is relevant to how the model handles desorption methods, which include, but are not limited to, thermal desorption, reactive desorption, and photodesorption (Vasyunin & Herbst, 2013a). This version of `Nautilus-1.1` also includes radiolysis chemistry and sputtering; processes initiated by cosmic rays colliding with surface and bulk ices that enhance grain surface chemistry (Paulive et al., 2022; Shingledecker & Herbst, 2018). The theory behind radiolysis and sputtering in relation to this chapter will be discussed later, but further explination can also be found in Chapters 2 and 3.

Initial abundances and physical conditions that will be used throughout the various models are shown in Table 4.2 and 4.3. Both the inital abundances and physical conditions are comparable to those observed in cold, dark molecular clouds, such as TMC-1. Binding energies of molecules examined in this work are shown in Table 4.1, used in the determination of desorption and thermal hopping rates. Binding energies are representative of a species on amorphous solid water, of which there are various orientations for most of the highlighted molecules. This results in one species potentially having multiple binding energies depending on the orientation of the species. The binding energies used in the model are averages of the various measured orientations of the species, either through experiment or other models.

Nonthermal desorption mechanisms for surface species have associated options in

Species	Binding Energy (K)

Table 4.1: Table of examined species' binding energies, in kelvin

`Nautilus-1.1`. Photodesorption (Bertin et al., 2013) and cosmic ray induced photodesorption (Hasegawa & Herbst, 1993) are included, along with reactive desorption at 1 per cent probability (Garrod et al., 2007). These three switches are set to "on", with both the photodesorption yield, and the cosmic ray induced photodesorption yield set at 1×10^{-4}. All models have the same parameters for the features described above.

4.2.1 Network

The network used in this chapter is the same in all models presented in the chapter, unless otherwise specified. The base network is the KIDA 2014 network with the modifications used in McGuire et al. (2021). While vinyl acetylene and propargyl radical are included in the KIDA network, benzyne is not currently in the network. Both vinyl acetylene and propargyl radical are vastly underproduced in current models based on the KIDA network, shown later in the chapter. We have added additional reactions providing new chemical pathways from detected precursor complex organic molecules (COMs) such as vinyl acetylene and propargyl radical to benzene and benzonitrile.

New gas-phase reactions to the model include reactions discussed in Cernicharo et al. (2021a) to vinyl acetylene, and in Agúndez et al. (2021) to propargyl radical. In addition to expanding the chemical network with respect to prescursor COMs, we explore new reactions involving precursor COMs, benzene, and benzonitrile to naphthalene,

1-cyanonaphthalene and 2-cyanonaphthalene via suprathermal reactions created by radiolysis. By expanding the chemical network to include more grain reactions, as well as novel gas reactions, this work aims to examine the efficiency of alternative routes leading to PAH formation, while accounting for observations of relevant precursor molecules that current models are under-producing.

While expanding the current network, there are problems with the current state of networks that will soon need to be addressed. First, while there are multiple studies on gas phase processes leading to the molecules studied in this chapter, there are few experimental studies for similar routes on interstellar ices. There are multiple cases of gas reactions not proceeding on grain surfaces (Enrique-Romero et al., 2016, 2021; Rimola et al., 2018), so further evidence is needed to gain a clearer picture of grain chemistry. Works without experimental evidence can direct experimental efforts, however. For example, if there are speculative reactions that are particularly efficient, experimental validation or theoretical treatments of the potential energy surface can confirm or refute the inclusion of the reaction.

Second is the state of isomers within the network. As more and more complex molecules are discovered, the number of possible isomers increase. There are already problems in this vein: C_4H_3CN isomers are not specified in the model, despite the detection of three isomers toward TMC-1 (Lee et al., 2021). Additionally, $C_6H_7^+$ in the network is considered linear, though $C_6H_5^+$ is cyclic (Wakelam et al., 2012). Although this does not cause problems currently, isomers need to be taken into account as astrochemistry continues into organic chemistry.

Third, finally, is that estimated reaction rates in the gas phase may need to be re-evaluated. Further discussion is in Section 4.3.

Table 4.2: Initial abundances of elements with respect to total hydrogen nuclei

Species	Abundance
H_2	0.499 [a]
He	9.000×10^{-2} [a]
N	6.200×10^{-5} [a]
C^+	1.700×10^{-4} [b]
O	1.429×10^{-4} [c]
S^+	8.000×10^{-8} [d]
Na^+	2.000×10^{-9} [d]
Mg^+	7.000×10^{-9} [d]
Si^+	8.000×10^{-9} [d]
P^+	2.000×10^{-10} [d]
Cl^+	1.000×10^{-9} [d]
Fe^+	3.000×10^{-9} [d]
F	6.680×10^{-9} [e]

[a] (Wakelam & Herbst, 2008)
[b] (Jenkins, 2009)
[c] (Hincelin et al., 2011)
[d] (Graedel et al., 1982)
[e] (Neufeld et al., 2005)

In addition to the thermal gas and grain reactions, the network also makes use of radiolysis chemistry and sputtering. Models with radiolysis, sputtering, and the expanded network will be referred to as Model RS, or the radiolysis-sputtering model. The model with the network from McGuire et al. (2021) will be called "Base" or the base model. There is also a gas-phase only model, also referred to as the gas model. The radiolysis reactions are similar to the ones used in Paulive et al. (2021), with expanded nitrogen chemistry. Sputtering is the same as in Paulive et al. (2022). The theory behind sputtering and radiolysis will be expanded upon in the next sections.

Table 4.3: Physical conditions utilized in models for this work, based on TMC-1 conditions

Parameter	TMC-1
n_{H} (cm^{-3})	10^4
n_{dust} (cm^{-3})	1.8×10^{-8}
T_{gas} (K)	10
T_{dust} (K)	10
N_{site} (cm^{-2})	1.5×10^{15}
ζ (s^{-1})	1.36×10^{-17}
A_{V}	10

4.2.2 Cosmic Ray - Ice Interactions

As mentioned earlier, cosmic rays are high energy nuclei, mostly consisting of protons. (Blasi, 2013). When these particles collide with gas and ice in the ISM, there are massive energy transfers, broadly split into two categories, based on the type of collision: elastic collisions, also called nuclear collisions, and inelastic collisions, or electronic collisions. Gas phase collisions resulting in ionizations are commonly used in models, even back to the earliest rate-equation based models (Herbst & Klemperer, 1973). The results of surface interactions will be the focus of this section, radiolysis chemistry, and sputtering. There are other effects, such as whole grain heating, that are also commonly used, however, we will not address them in detail in this chapter (Hasegawa & Herbst, 1993; Kalvāns & Kalnin, 2020b).

In order to include radiolysis and sputtering in our models, rate constants for each process need to be calculated. Basic chemical kinetics states that we can approximate a first-order rate coefficient, k, in units of s^{-1}, from the product of a flux, ϕ (particles s^{-1} cm^{-2}), and a cross section, σ (cm^2):

$$k = \sigma\phi. \tag{4.4}$$

For comsic rays, we can calculate a flux by integrating the cosmic ray energy function $j(E)$ obtained by Spitzer & Tomasko (1968),

$$j(E) = \frac{0.90}{(0.85 + E_G)^{2.6}} \frac{1}{(1 + 0.01/E_G)}. \tag{4.5}$$

over the cosmic ray energy distribution, from the minimum of 0.3 MeV (3×10^{-4} GeV) to the maximum of 100 GeV, represented in the above equation as E_G, in GeV. This results in a flux of 8.6 cosmic ray particles cm^{-2} s^{-1}. We can also include a scaling factor, ζ, as in Shingledecker & Herbst (2018), so that the cosmic ray flux can be easily scaled to the cosmic ray ionization rate for the area of the ISM. For TMC-1, the cosmic ray ionization rate is 1.36×10^{-17}, which is what we scale the flux to. This results in a general cosmic ray flux for any region of the ISM based on the ionization rate:

$$\phi = 8.6 \left(\frac{\zeta}{1.36 \times 10^{-17}} \right). \tag{4.6}$$

To obtain cross sections for individual processes that we include as effects of comsic ray ice collisions, we will need to split up the total cross section (σ_{tot}) into specific cross sections. We can define the total cross section into two collision types, nuclear collisions (σ_n) and electronic collisions (σ_e) that will be further subdivided in their respective sections:

$$\sigma_{\text{tot}} = \sigma_n + \sigma_e \tag{4.7}$$

All cross sections used in this paper have units of cm^2.

Nuclear (Elastic) Collisions

One category of collisions that cosmic ray bombardment causes are nuclear collisions, so named as the collisional effects come from nuclei interacting (Johnson, 1990). This type of collision does not cause the ionizations and excitations that make up radiolysis, so in our models, nuclear collisions contribute only to sputtering, however, that is not to say that sputtering makes up the whole of nuclear collisions. A full explanation of the implementation of sputtering can be found in Paulive et al. (2022), along with more discussion on dividing up the effects of nuclear collisions.

We obtain the nuclear cross section by taking the weighted average of the nuclear stopping power cross section ($S_n(E)$), a measure of energy loss, in eV cm^2. We obtain the nuclear stopping power cross section of H^+ bombarding liquid water because as far as the authors know, there is no data on stopping power for amorphous solid water. The nuclear stopping power cross section varies not just for incoming ion and target, but also the energy of the incoming ion. Inclusion in the model will require an average nuclear stopping power cross section ($\bar{S}_n$) because the model does not keep track of the ion that is the cosmic ray or the individual energy of the ion. The average is then obtained using the following equation:

$$\bar{S}_n = \frac{\sum S_n(E) j(E)}{j(E)}, \tag{4.8}$$

where $j(E)$ is the previously mentioned Spitzer-Tomasko cosmic ray energy function. We can obtain a nuclear sputtering cross section (σ_{ns}) by then dividing the $\bar{S}_n$ by the average energy loss to nuclear collisions (W_n) (Sigmund, 1969). We estimate W_n to be 2.45 eV, further discussed in Paulive et al. (2022). This results in a σ_{ns} of 1.424×10^{-18} cm^2.

Table 4.4: Parameters for nuclear sputtering calculations on amorphous solid water.

Parameter	Value	Reference
S_n (eV cm^2)	3.489×10^{-18}	(Paulive et al., 2022)
W_n	2.45 eV	(Sigmund, 1969; Paulive et al., 2022)
$\bar{\sigma}_{\text{diff}}$ (cm^2)	3.6×10^{-16}	(Johnson, 1990)
U (eV)	0.49	(Garrod & Herbst, 2006)
α	0.6	(Andersen & Bay, 1981)
Y_{ns}	1.8×10^{-3} H_2O per H^+	(Paulive et al., 2022)
σ_n (cm^2)	1.424×10^{-18}	(Paulive et al., 2022)

This would be enough to calculate a suitable rate constant assuming one particle is removed from the surface for every nuclear collision made, however this is not the case, both in theory and experiment (Sigmund, 1969; Brown et al., 1978; Brown & Johnson, 1986; Dartois et al., 2019). We calculate a sputtering yield (Y_{ns}) using a method from Johnson (1990),

$$Y_{ns} \approx \frac{3\alpha S_n}{2\pi^2 \bar{\sigma}_{\text{diff}} U}. \tag{4.9}$$

where α is an experimentally determined fraction of the nuclear stopping power that is involved in cascade collisions that are close to the surface. S_{n} is the nuclear stopping power, $\bar{\sigma_{\text{diff}}}$ is the average diffusion cross section, and U is the average binding energy in eV. For amorphous solid water being impacted by H^+ ions, Equation (4.9) yields an average result of of 1.8×10^{-3} particles per cosmic ray proton, with the parameters organized in Table 4.4. The final form of the nuclear sputtering rate constant is then $k_{ns} = Y_{ns}\sigma_{ns}\phi$, with $k_{ns} = 2.2 \times 10^{-20}$ particles per second.

Table 4.5: Parameters for calculating electronic sputtering terms on amorphous solid water.

Parameter	Value	Reference
$\bar{S}_e$ (eV cm^2)	1.131×10^{-15}	(Paulive et al., 2022)
W_e (eV)	27	(Shingledecker & Herbst, 2018)
f_e (Unitless)	0.20	(Johnson & Brown, 1982)
$C_e \times (f_e^2)$ (Unitless)	8×10^{-4}	(Brown et al., 1980)
n_B (cm^{-3})	3.3×10^{22}	(Brown et al., 1980)
U (eV)	0.49	Garrod & Herbst (2006)
Y_{es}	0.0045 H_2O per H^+	(Paulive et al., 2022)
σ_{es} (cm^2)	2.09×10^{-16}	(Paulive et al., 2022)

Electronic (Inelastic) Collisions - Sputtering

Similar to the nuclear cross section, we further subdivide the electronic cross section (σ_e) as follows:

$$\sigma_e = \sigma_{\text{ion}} + \sigma_{\text{exc}}, \tag{4.10}$$

where σ_{ion} is the ionization cross section, and σ_{exc} is the excitation cross section. Both cross sections contribute to sputtering, and both are considered a part of radiolysis. We shall start with electronic sputtering, which is similar to nuclear sputtering, though some terms are for electronic collisions instead of nuclear collisions.

The rate constant is calculated in the same way as nuclear sputtering, by multiplying the cosmic ray flux, the electronic sputtering yield (Y_{es}), and the electronic sputtering cross section (σ_{es}). To calculate Y_{es}, we use the following equation from (Johnson, 1990):

$$Y_{es} \approx C_e \times (f_e^2)[(n_B^{-1/3})(n_B \times \bar{S}_e)/U]^2. \tag{4.11}$$

Table 4.6: Parameters for CO_2 sputtering cross section and yield calculations

Parameter	Value	Reference
$\bar{S}_e$ (cm^2 eV)	2.329×10^{-15}	This work
W_e (eV)	34.2	(Johnson & Brown, 1982)
f_e (Unitless)	0.19	(Johnson & Brown, 1982)
$\sigma_{\rm es}$ (cm^2)	3.58×10^{-16}	This work
$C_e \times f_e^2$ (Unitless)	1×10^{-3}	(Brown et al., 1982)
$n_{\rm B}$ (cm^{-3})	2.3×10^{-22}	(Johnson, 1990)
U (eV)	0.22	(Garrod & Herbst, 2006)
Y_{es}	0.073 CO_2 per H^+	This work

Here C_e is an experimental unitless constant, while n_B (particles cm^{-3}) is used to approximate the average thickness of a monolayer of a surface species. f_e is the unitless fraction of electronic energy lost to the surface through repulsive decay. $\bar{S}_e$ is the average electronic stopping power cross section, calculated using Equation 4.8 in the same way as $\bar{S}_n$, by taking the weighted average over the cosmic ray energy distribution from 3×10^{-4} GeV to 100 GeV. $\bar{S}_e$ has a value for H^+ ions impacting amorphous solid water of $1.131 \times 10^{-}15$ eV cm^2. This is 3 orders of magnitude higher than the rate constant for nuclear sputtering. All of these parameters are organized in Table 4.5.

After obtaining a yield, we can continue to calculate the electronic sputtering cross section, σ_{es}, by dividing $\bar{S}_e$ by the product of W_e and f_e, where W_e is the average energy lost to the surface due to electronic collisions. W_e is a broad term, and simply dividing $\bar{S}_e$ by W_e would overestimate the energy that goes into sputtering (Brown et al., 1980; Johnson & Brown, 1982). Therefore, we include f_e, the fraction of energy lost to the surface by repulsive decay caused by electronic collisions. This results in an σ_{es} of $2.09 \times 10^{-}16$ cm^2, also reported in Table 4.5. Multiplying the calculated electronic sputtering yield, electronic sputtering cross section, and the cosmic ray flux together, $k_{es} = Y_{es}\sigma_{es}\phi$, results in an electronic sputtering rate

constant of $k_{es} = 8.1 \times 10^{-18}$ particles per second.

In Table 4.6, we list the same parameters used to calculate electronic sputtering rates for amorphous solid water, but with values for condensed gas phase CO_2. In our models, the sputtering rates are based on the values for a mixed ice of water and CO_2, where the rate constant is dependent on the ratio of water ice to CO_2 ice:

$$k_{es}^{\text{mix}} = \left(k_{es(\text{H}_2\text{O})} \frac{N_{\text{H}_2\text{O}}}{N_{\text{H}_2\text{O}} + N_{\text{CO}_2}} \right) N_i + \left(k_{es(\text{CO}_2)} \frac{N_{\text{CO}_2}}{N_{\text{H}_2\text{O}} + N_{\text{CO}_2}} \right) N_i. \tag{4.12}$$

The above equation only takes into account electronic cross sections for sputtering. The discrepancy in nuclear sputtering and electronic sputtering rate constants is due to the amount of energy transferred at cosmic ray energies; electronic collisions are much more efficient at depositing energy at the surface due to the high speed and charged nature of the cosmic ray allowing for electromagnetic interactions. In sharp contrast is the nuclear cross section, which relies on the nuclei of the cosmic ray and target actually colliding, significantly smaller than the area of electromagnetic interactions that cause electronic collisions.

Electronic Collisions - Radiolysis

The other process to come out of electronic collisions is radiolysis. More thorough exploration of radiolysis and suprathermal chemistry can be found in Shingledecker & Herbst (2018) and Paulive et al. (2021), though a brief explanation follows. Radiolysis consists of the chemical effects that occur as a result of electronic collisions, specifically ionization and electronic excitation of the target species. Suprathermal species in this case are non-specific electronically excited species, instead of being in a specific excited state, which is more suitable to molecular dynamic and ab initio simulations.

We denote suprathermal species by an asterisk "*" after the species name.

Ionization and excitation of the target due to radiolysis is further split into two different types, depending on if suprathermal species are generated or not, with A representing a target species, and B and C representing product species:

$$\mathrm{A} \rightsquigarrow \mathrm{A}^+ + \mathrm{e}^- \tag{4.13}$$

$$\mathrm{A} \rightsquigarrow \mathrm{A}^+ + \mathrm{e}^- \rightarrow \mathrm{A}^* \rightarrow \mathrm{B}^* + \mathrm{C}^* \tag{4.14}$$

$$\mathrm{A} \rightsquigarrow \mathrm{A}^* \rightarrow \mathrm{B} + \mathrm{C} \tag{4.15}$$

$$\mathrm{A} \rightsquigarrow \mathrm{A}^* \tag{4.16}$$

The squiggly arrow represents bombardment by a cosmic ray. Reaction 4.13 is assumed to immediately recombine with the ionized electron on or within the grain ice, resulting in a neutral A. This process is not included in the model because there is no overall change in the ice. Reaction 4.14 is the other result of ionization, resulting in suprathermal products B* and C*. This will be referred to as a Type 1 radiolysis reaction. Excitation reaction 4.15 results in thermal B and C after A* dissociates; this is called a Type 2 reaction, while Reaction 4.16 results in suprathermal A*, called Type 3.

Calculating the rate constants is slightly different for radiolysis chemistry compared to sputtering. While the theory is still based on obtaining a cross section for ionization

Species	Type I	Type II	Type III
HCN	3.704	1.008	1.008
HNC	3.704	5.365	5.365
H_2CN	3.704	6.252	6.252
H_2CCN	3.704	5.365	5.365
CH_3CN	3.704	5.832	5.832
C_6H_6	3.704	3.454	3.454
$C_{10}H_8$	3.704	6.280	6.280

Table 4.7: List of G values for additional radiolysis reactions by type, with units of ionizations or excitations per 100 eV. New radiolysis reactions are displayed in Tables C.1 and C.2. G values are calculated via the Shingledecker-Herbst method, described in Shingledecker & Herbst (2018), and this work.

and excitation individually to multiply a flux, Shingledecker & Herbst (2018) convert the cross section into a G value, or the average number of ionized or excited species per 100 eV of energy transfer to the surface, using the equation below

$$\bar{\sigma} \approx \frac{\bar{S}_e}{W_e} = \left(\frac{G}{100}\right) \bar{S}_e \tag{4.17}$$

Thus the rate constant, k_r takes the form below:

$$k_r = \left(\frac{G}{100}\right) \bar{S}_e \phi. \tag{4.18}$$

Calculated G values using the proccess in Shingledecker & Herbst (2018) for each individual radiolysis outcome for new species not included in Shingledecker et al. (2018) or Paulive et al. (2021) are presented in Table 4.7. These radiolysis reactions are to provide additional sources of surpathermal N and CN; previously, the only other species to create suprathermal N were NO, NO_2, and NH_3, while suprathermal CN was not in the model. Benzene and naphthalene are added as additional destruction routes, while benzonitrile and cyanonaphthalene will be addressed in future work.

4.3 Results and Analysis

Within this section, we will address new and old reactions producing and destroying the list of aromatic and aromatic-adjacent species. The molecules focused on are benzene, benzonitrile, naphthalene, 1-cyanonaphthalene, 2-cyanonaphthalene, vinyl acetylene, cyanovinyl acetylene, propargyl radical, cyanopropyne, and the 1-cyanopropargyl radical.

4.3.1 Benzene and Benzonitrile

The primary routes to benzene that have already been explored that are relevent to interstellar conditions are gas-phase production routes that had been mentioned in the introduction. Reactions 4.1 and 4.2 are both efficient in the gas phase, yet still lead to an underproduction of benzonitrile. There are multiple possible reasons for the underproduction of benzonitrile in the gas-phase.

One of note is the electron recombination reaction with $C_6H_7^+$ (Eq. 4.1). While one set of products are C_6H_6 and H, the current KIDA network has another set of products, with a 50% branching ratio:

$$C_6H_7^+ + e^- \rightarrow C_6H_2 + 2H_2 + H. \tag{4.19}$$

This reaction was first estimated in Herbst & van Dishoeck (2009) to have a rate constant of 3×10^{-6} cm^3 s^{-1}. However, Hamberg et al. (2011) show that the pathway leading to C_6H_2 is a minor product at best, and that a six-membered ring structure is "retained almost entirely in both cases", though they could not conclusively determine the branching ratio between C_6H_6 + H and C_6H_5 + H_2. As a result, we remove

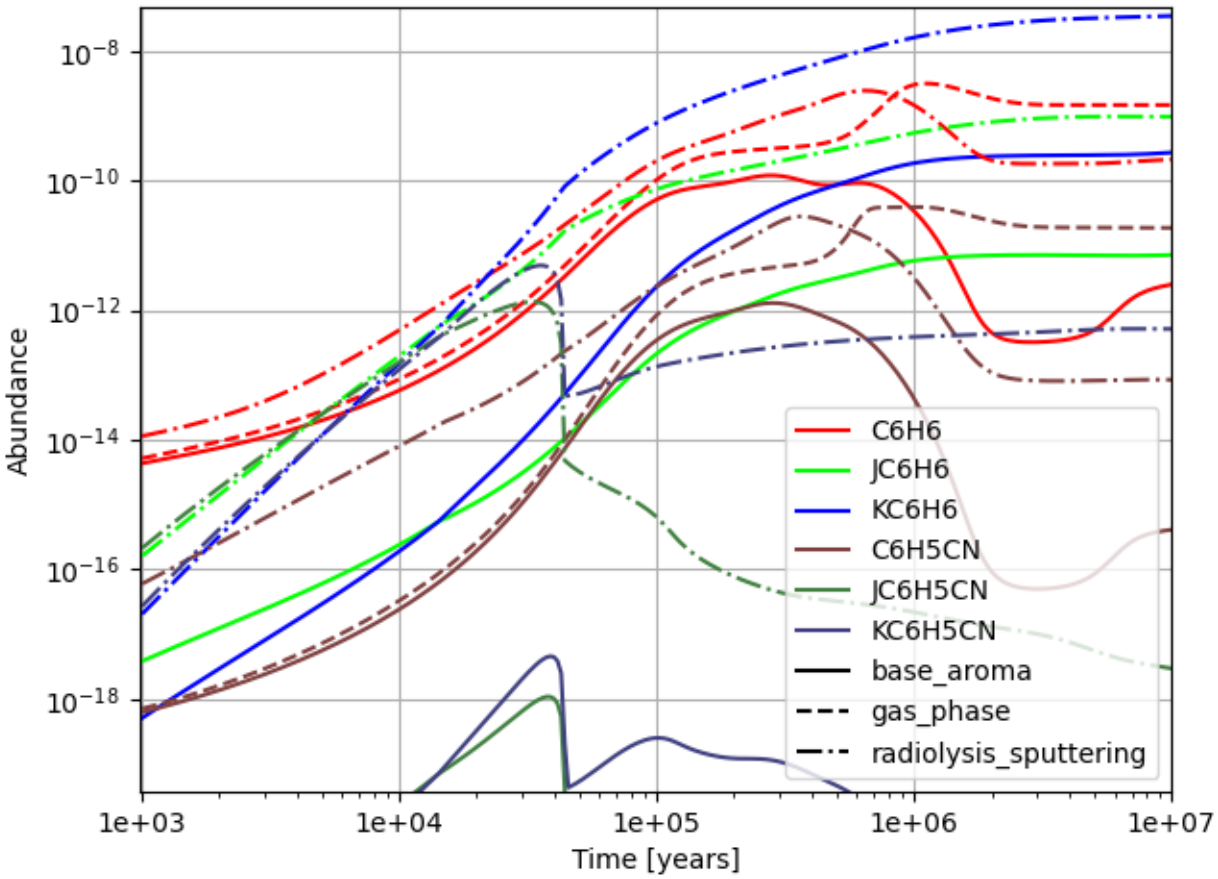

Figure 4.1: Fractional abundances of benzene and benzonitrile with respect to hydrogen in the gas phase, ice surface, and ice bulk, each with a different color. The base model is represented through a solid line, the gas-phase only model is represented with a dashed line, and the model with radiolysis and sputtering is a dotted-dashed line.

Reaction 4.19 from the network, and replace it with the reaction below:

$$C_6H_7^+ + e^- \rightarrow C_6H_5 + H_2. \tag{4.20}$$

Reaction 4.20 has an uncertain branching ratio with Reaction 4.1, according to Hamberg et al. (2011), unfortunately, keeping a 50% branching ratio does not noticeably increase the abundance of benzene or benzonitrile. We also update the rate constant from the previous constant of

$$k(T) = 5.0 \times 10^{-7} \left(\frac{T}{300}\right)^{-0.5}, \tag{4.21}$$

to the value measured by Bouwman et al. (2012), and corroberated by Hamberg et al. (2011)

$$k(T) = 2.4 \times 10^{-6} \left(\frac{T}{300}\right)^{-0.83}, \tag{4.22}$$

While McGuire et al. (2018) does get close to matching the observed abundance, there is a noticeable absence of grain ice chemistry regarding benzene and benzonitrile formation. Thus, we include two sets of reactions leading to benzene and benzonitrile on the surface. The first are suprathermal reactions that have been studied, and shown to occur via experiment and theoretical models. They are a series of reactions starting with electronically excited acetylene ices that lead to benzene (Zhou et al., 2010, 2014; Abplanalp & Kaiser, 2020):

$$C_2H_2^* + C_2H_2 + C_2H_2 \rightarrow C_4H_4^{*\dagger} + C_2H_2 \rightarrow C_6H_6 \tag{4.23}$$

Zhou et al. (2010) irradiated pure acetylene ices and produced vinyl acetylene, methylenecyclopropene, and benzene. Ab intio calculations from the same work suggested that if the first electronically excited state, $^3B_2$ acetylene, reacts with a ground state acetylene, an excited *trans*-CHCHCHCH intermediate would form. The KIDA network currently only has one C_4H_4 isomer, vinyl acetylene, so we assume that vinyl acetylene is the only other side product of the reaction, though the experimental evidence points to vinyl acetylene and benzene being the primary products of the irradiation of acetylene ices at 10 K. From this, we also include the reactions

$$C_2H_2^* + C_2H_2 \rightarrow CH_2CHC_2H, \tag{4.24}$$

$$CH_2CHC_2H^* + C_2H_2 \rightarrow C_6H_6, \tag{4.25}$$

$$CH_2CHC_2H + C_2H_2^* \rightarrow C_6H_6, \tag{4.26}$$

and their cyano-group bearing equivalents, leading directly to benzonitrile:

$$C_2H_2^* + HC_3N \rightarrow C_4H_3CN, \tag{4.27}$$

$$C_2H_2 + HC_3N^* \rightarrow C_4H_3CN, \tag{4.28}$$

$$C_4H_3HCN^* + C_2H_2 \rightarrow C_6H_5CN, \tag{4.29}$$

$$C_4H_3HCN + C_2H_2^* \rightarrow C_6H_5CN, \tag{4.30}$$

$$C_2H_2^* + C_2H_2 + HC_3N \rightarrow C_6H_5CN, \tag{4.31}$$

$$C_2H_2 + C_2H_2 + HC_3N^* \rightarrow C_6H_5CN, \tag{4.32}$$

Where species with a superscript asterisk represent an electronically excited suprathermal species. Jose et al. (2021) theoretically modeled both the reaction potential energy surface between cyanoacetylene and acetylene in mixed clusters of acetylene and cyanoacetylene and molecular dynamics simulations of the same clusters. The clusters are various combinations of acetylene and cyanoacetylene ices, ranging from one acetylene molecule and three or four cyanoacetylene molecules, to three acetylene molecules and three cyanoacetylene molecules. They determined that the reaction of two acetylene molecules and cyanoacetylene would build to complex molecules when ionized, with one product being benzonitrile. The reaction leading to benzonitrile was calculated to be exothermic and barrierless. There are multiple other products produced during molecular dynamics simulations of the clusters, with C_4H_4, C_5H_3N, C_7H_5N and $C_{10}H_6N_2$ isomers all detected in varying percentages depending on the initial ratio of acetylene to cyanoacetylene.

With the additional grain reactions added to the network and the correction of the products of the $C_6H_7^+$ electron recombination reaction, Figure 4.1 shows an approximate order of magnitude increase in the amount of benzene and benzonitrile with radiolysis, sputtering, and changes to the network (the dashed-dotted line) when

compared to the base model (the solid line). We also provide a gas-phase only model (dashed line) with the changes to the network for further comparison. In the model with radiolysis and sputtering, benzene has a modeled abundance of 1×10^{-9}, while benzonitrile is at approximately 1×10^{-11} at 2×10^{5} yr. The benzonitrile abundance is approximately the same as in McGuire et al. (2018), and under-produced compared to the observed abundance of 4×10^{-11} in TMC-1 by a factor of 4, though the model peaks in benzonitrile at 5×10^{5} years, with a fractional abundance of 3×10^{-11}. This peak abundance is less than the observed amount a factor of 1.3. This suggests that benzene is produced primarily through efficient gas-phase reactions, and is also efficiently destroyed in the gas phase, though efficient desorption and production from grains can slightly increase gas-phase abundances.

Examining the production and destruction reactions in the radiolysis and sputtering model, benzonitrile is primarily produced at times before 10^{5} yr by Reaction 4.31, then gets outproduced by Reaction 4.3 after 10^{5} yr. These results are to be expected, as gas phase reactions are generally more efficient than grain reactions, due to most surface species inability to desorb from the grain surfaces. Even with reactive desorption, cosmic ray heating, and sputtering, there is not a high enough concentration of benzonitrile on the grain surface to outproduce the efficient destruction reactions. The abundances of benzonitrile on the grain surface and bulk are not of a similar ratio compared to benzene, despite sharing similar production routes. This low grain abundance, coupled with the ratio of gas-phase benzene in the model to benzene ice, suggests that there are thermal pathways to benzonitrile on the grain surface that are not yet included in the model. A possible route would be through the hydrogenation of ortho-benzyne (o-C_6H_4), though surface hydrogenation reactions have yet to be studied (Cernicharo et al., 2021b).

As for destruction pathways in the model for benzonitrile, the most efficient are all ion-neutral destruction mechanisms, where benzonitrile quickly reacts with a common cation, such as C^+, HCO^+, or H_3^+. In the case of the radiolysis and sputtering model, reactions with C^+ dominate until around 10^5 yr, until enough H_3^+ is generated to overtake the reaction with carbon cation. On the grains, the most efficient destruction pathways for benzene are with suprathermal CN to form benzonitrile, a new reaction. Benzonitrile on the other hand, is destroyed very efficiently on surfaces by reacting with atomic hydrogen, to form C_6H_5 and HCN, according to the model. This reaction has only been studied under thermal combustion conditions in the gas phase, but may be an efficient pathway at low temperatures on surfaces (Lifshit, Cohen, Braun-Unkhoff & Frank, Lifshit et al.). The primary destruction mechanism for benzonitrile is two orders of magnitude faster than its production starting at 1×10^5 yr, and it will be difficult to find thermal reactions that are able to compete with the speed of atomic hydrogen on grain surfaces at 10 K.

The gas-phase only model further suggests that with the current network gas-phase production and destruction mechanisms dominate for both benzene and benzonitrile. Gas-phase benzene and benzonitrile abundances only see a difference by at most factor of 2.5 between the gas-phase only model and the radiolysis/sputtering model, providing further evidence that grain products in the current network are not necessary, and that gas-phase production can still be enhanced, when extra precursors are not captured on grain surfaces. Further investigations on thermal reactions involving these species on grain surfaces, particularly benzonitrile, will be needed to confirm the idea that gas phase production routes are the most efficient.

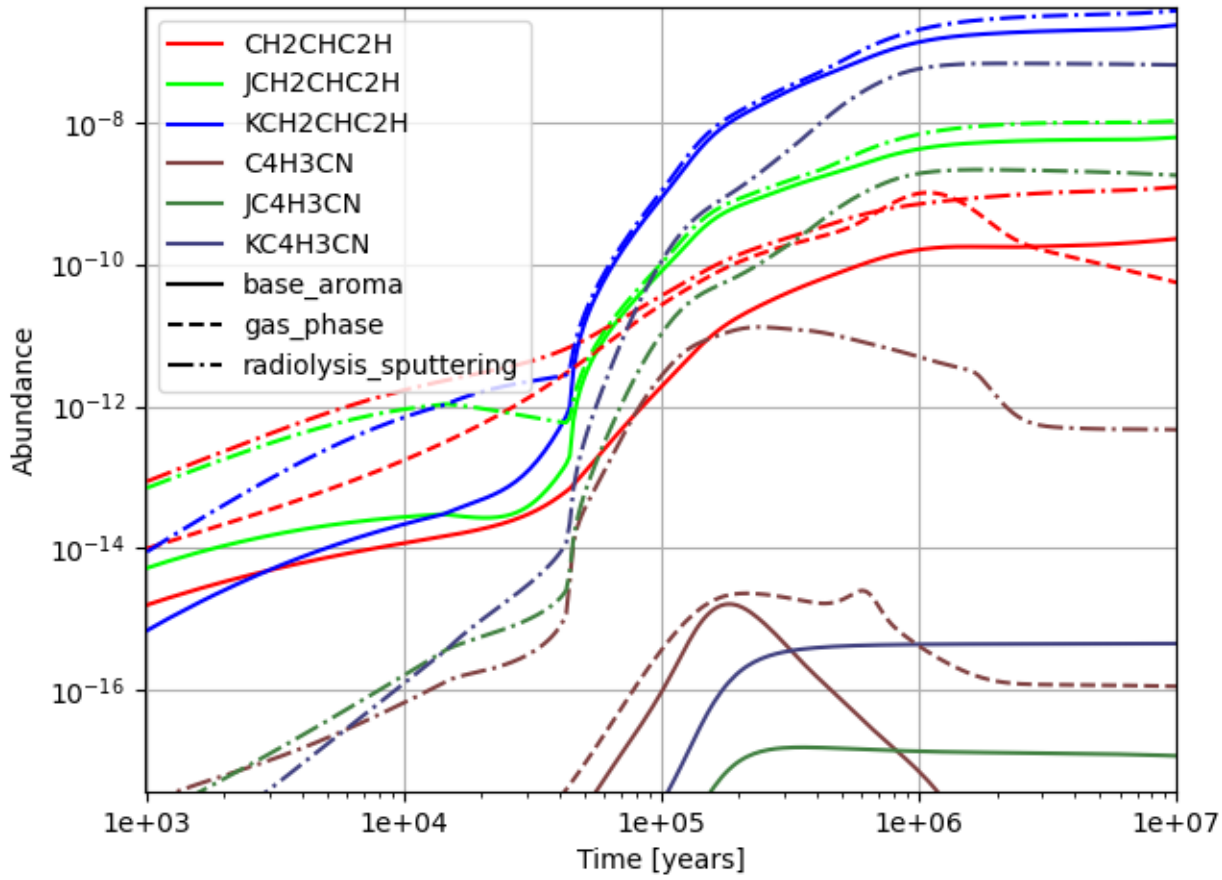

Figure 4.2: Fractional abundances of vinyl acetylene and C_4H_3CN isomers with respect to hydrogen in the gas phase, ice surface, and ice bulk, each with a different color. The base model is represented through a solid line, the gas-phase only model is represented with a dashed line, and the model with radiolysis and sputtering is a dotted-dashed line.

4.3.2 Vinyl acetylene and C_4H_3CN Isomers

For vinyl acetylene production methods, we take the KIDA network of reactions and include reactions mentioned by Cernicharo et al. (2021a) in their discovery paper. Reactions included are:

$$C_2 + C_2H_6 \rightarrow CH_2CHC_2H + H_2 \tag{4.33}$$

$$CH + CH_3CCH \rightarrow CH_2CHC_2H + H \tag{4.34}$$

$$CH + CH_2CCH_2 \rightarrow CH_2CHC_2H + H \tag{4.35}$$

$$C_2H + C_2H_4 \rightarrow CH_2CHC_2H + H \tag{4.36}$$

Reactions 4.33, 4.34, 4.35, and 4.36 all are predicted to be efficient at 10 K in the gas phase (Canosa et al., 2007; Daugey et al., 2005; Bouwman et al., 2012). They also test the production of C_5H_3N via reaction 4.37, acting as a general indicator of the multiple possible isomers detected in TMC-1 (Lee et al., 2021). We refer to those isomers as C_4H_3CN within the model. Reaction 4.37 is exothermic, but the reactions CN + acetylene, and CN + ethene have small activation energies of 1-3 kcal/mol, or 500-1500 K (Yang et al., 1992).

$$CN + CH_2CHC_2H \rightarrow C_4H_3CN + H \tag{4.37}$$

This barrier, although small, probably rules out Reaction 4.37 as an efficient producer of C_4H_3CN isomers at 10 K in the gas phase. However, this barrier can be overcome by suprathermal species on the surface, so we include 4.37 as a suprathermal grain equation:

$$CN^* + CH_2CHC_2H \rightarrow C_4H_3CN + H \tag{4.38}$$

where suprathermal CN is generated through new radiolysis reactions, tabulated in Table C.2 .

There is another alternative route to the production of C_4H_3CN, and possibly other isomers, by hydrogen addition, similar to how methanol is produced. A general reaction is below, however, the reaction between hydrogen radical and cyanoacetylene has an activation energy of approximately 1 kcal/mol, though the most energetically favorable product is H_2C_3N (Parker et al., 2004). Additionally, this reaction was studied under gas-phase conditions, and not surface ice conditions, which may effect the energetics of the reaction:

$$HC_nN + H^* \rightarrow H_2C_nN. \tag{4.39}$$

While this type of reaction seems like an efficient way to produce CNCHCCH, CNCH2CCH, and C_4H_3CN from 4 and 5 carbon cyanopolyyines, the network does not contain protenated cyanopolyyines (H_2C_nN), and their reactions are not well studied, so we omit these reactions, and the subsequent hydrogenation. As an alternative, we include in the model cyanopolyyines reacting with suprathermal H_2 as a concerted step, suggested by (Lee et al., 2021), but the actual mechanism for hydrogenation is still

elusive.

With all of the included reactions, vinyl acetylene has a calculated abundance of 1.3×10^{-10}, shown in Figure 4.2, alongside C_4H_3CN isomers, which have a modeled gas-phase abundance of 1.2×10^{-11}. Both abundances are from the Model RS. For vinyl acetylene, this abundance is an increase by a factor of 7 from the base model. The observed abundance of vinyl acetylene is 1.2×10^{-9}, about an order of magnitude from the modeled abundance (Cernicharo et al., 2021a). At times later in the model, vinyl acetylene reaches the observed abundance. The major production routes of vinyl acetylene are ejection by sputtering, reactive desorption between atomic hydrogen and C_4H_3, the gas-phase reaction between CH and CH_2CCH_2, and finally dissociative recombination with $C_4H_5^+$. Destruction pathways seem to be lacking, as major destruction routes are through adsorbing onto grains and gas-phase cosmic ray induced photodissociation leading to C and CH_3CCH. There are no current destruction routes in the gas-phase leading to more complex molecules. While reactions 4.25 and 4.29 may proceed under energetic conditions on the grain surface, as far as we are aware, they have barriers to reactions in the gas phase, and thus will not proceed at 10 K.

For C_4H_3CN isomers, we see an increase in approximately 4 orders of magnitude, as the new reactions radiolysis and sputtering result in a modeled abundance of 1.2×10^{-11}, a factor of 1.56 less than the observed abundance of vinylcyanoacetylene (VCA, CH2CHC2CN), with an observed abundance of 1.87×10^{-11} (Lee et al., 2021). Also discovered in Lee et al. (2021) are *trans*-(E)-cyanovinylacetylene, and *trans*-(Z)-cyanovinylacetylene, with observed abundances of 2.9×10^{-11} and an upper limit abundance of 2×10^{-11}. These two molecules have worse agreement with the modeled isomers than VCA, so while there is room for better agreement between

these detected isomers, the model with radiolysis and sputtering closely replicates abundances, suggesting that the main methods of producing C_4H_3CN are on the grain. The most efficient method at later times is the concerted hydrogen abstraction between surface HC_5N and surface H_2. This is slightly unusual, as the cyanopolyyine family is generally efficiently formed in the gas phase, and not thought to contribute significantly toward grain chemistry due to multiple barriers. Efficient destruction routes in the gas are through ion-neutral reactions with H_3^+, HCO^+, C^+, and H^+. In a similar manner to the benzonitrile, the C_4H_3CN isomers in the base model are more abundant in the gas phase compared to on the grain surface suggesting incomplete grain production, as COMs generally have the highest abundance in the ice bulk at 10^5 years, followed by ice surface, and the lowest abundance in the gas phase. In the radiolysis-sputtering model, this is returned to normal ratios, with bulk ice being the most abundant, then the surface ice, and lowest the gas-phase.

4.3.3 Propargyl radical, cyanopropyne, and 1-cyanopropargyl radical

All of the reactions discussed in the detection paper of propargyl radical are already in the KIDA network, with numerous gas and grain production and destruction routes. Propargyl radical is mostly formed through

$$C + C_2H_4 \rightarrow H + CH_2CCH \tag{4.40}$$

and electron recombination reactions with $C_3H_4^+$, $C_3H_5^+$, and $C_5H_5^+$. Destruction reactions of propargyl radical include reactions with atomic hydrogen, atomic oxygen,

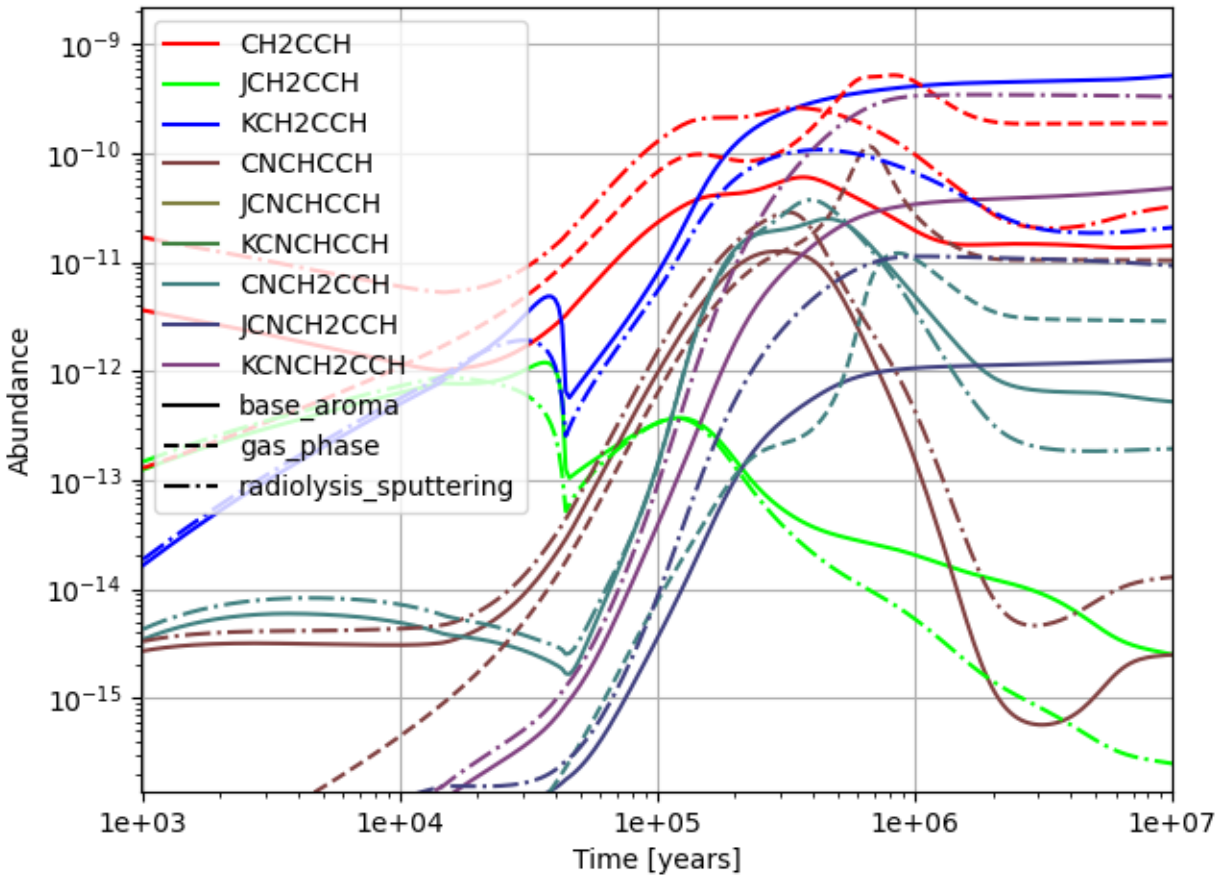

Figure 4.3: Fractional abundances of propargyl radical, cyanopropyne, and 1-cyanopropargyl with respect to hydrogen in the gas phase, ice surface, and ice bulk, each with a different color. The base model is represented through a solid line, the gas-phase only model is represented with a dashed line, and the model with radiolysis and sputtering is a dotted-dashed line.

and atomic nitrogen, all in the gas phase. However, Agúndez et al. (2021) claims the reactions with atomic oxygen and nitrogen do not proceed at 10 K due to barriers in similar systems. We find support of barriers for the reactions with atomic oxygen, but not for atomic nitrogen (Adusei et al., 1996; Michael & Lee, 1977). We therefore remove the oxygen reactions with propargyl radical from the network in the gas-phase model and the radiolysis-sputtering model.

In the base KIDA network, propargyl radical has a gas phase abundance of 4.3×10^{-11}, displayed in Figure 4.3, alongside gas and surface ice abundances of cyanopropyne ($CNCH_2CCH$) and 1-cyanopropargyl radical (CNCHCCH). However, this is approximately 2.5 orders of magnitude too low for the observed abundance of 8.7×10^{-9} (Agúndez et al., 2021). The effects of the changed network in the radiolysis-sputtering model results in a gas-phase abundance of 2.1×10^{-10}, an increase from the base network by a factor of 5, but still not enough to adequately replicate observed abundances, which still have a difference by more than an order of magnitude. The gas phase model does slightly better at 8×10^5 years with an abundance of 5.3×10^{-10}, but it still underproduces both compared to observations, and the gas model used in Agúndez et al. (2021).

Removing the destruction reactions with atomic nitrogen in addition to the destruction reactions with atomic oxygen increases the peak modeled abundance in model RS to 4.5×10^{-9}. However, if we also remove the reactions between atomic oxygen and CH_3CCH:

$$O + CH_3CCH \rightarrow OH + CH2CCH \tag{4.41}$$

$$O + CH_3CCH \rightarrow CO + C_2H_4 \tag{4.42}$$

the modeled abundance of propargyl radical decreases, because Reaction 4.41 produces propargyl radical. Removing these reactions with oxygen, according to the model utilized in Agúndez et al. (2021), should still increase the amount of CH_2CCH, but does not in our models. Further examination of these reactions at low temperatures will be needed to confirm activation energy barriers, or even efficiency at low temperatures.

While the RS model does efficiently increase gas-phase abundances of CH_2CCH, it is mostly through sputtering, as radiolysis chemistry is not particularly efficient at making CH_2CCH on the grain surface, and is more efficiently produced through gas-phase reactions.

We see similar results for cyanopropyne and 1-cyanopropargyl radical. 1-cyanopropargyl radical is primarily produced through a gas-phase reaction between atomic carbon and CH_2CHCN. Added surface suprathermal reactions between HC_4N and H^* are not particularly efficient, and contribute little to gas-phase abundances. In Figure 4.3, grain bulk and grain surface abundances are too low to be in the frame, even with additional suprathermal reactions. Cyanopropyne is primarily produced through a gas phase reaction between CN and CH3CCH. The reaction between HC_4N and H_2^* is similarly slow compared to the reaction with suprathermal atomic hydrogen, possibly due to a low abundance of HC_4N on the grain surface. Both species have yet to be detected toward TMC-1 as far as the authors know.

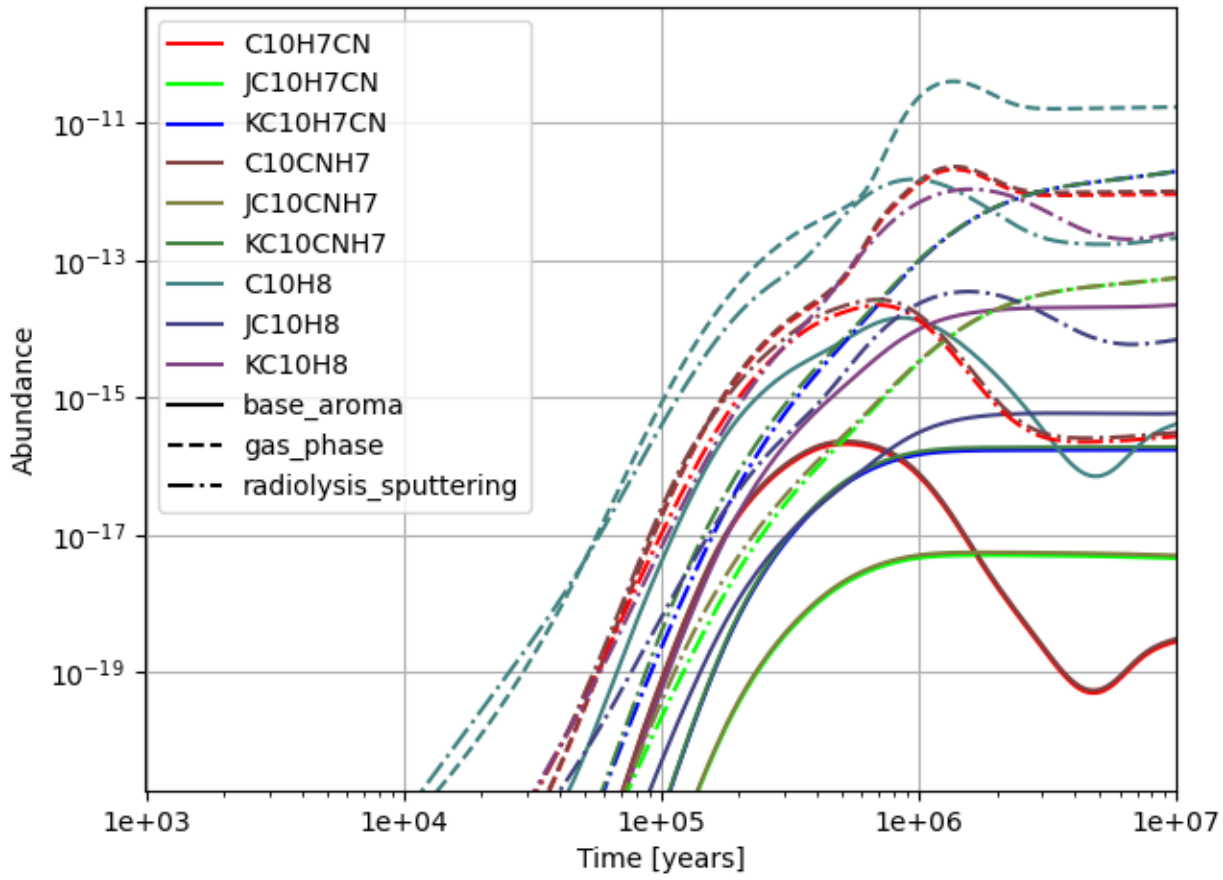

Figure 4.4: Fractional abundances of naphthalene, 1-cyanonaphthalene, and 2-cyanonaphthalene with respect to hydrogen in the gas phase, ice surface, and ice bulk, each with a different color. The base model is represented through a solid line, the gas-phase only model is represented with a dashed line, and the model with radiolysis and sputtering is a dotted-dashed line.

4.3.4 Naphthalene, 1-cyanonaphthalene, and 2-cyanonaphthalene

Naphthalene is not included in the base KIDA network, and was added as a part of (McGuire et al., 2021), alongside the two detected cyanonaphthalene isomers. From the same paper, there are proposed reaction routes to naphthalene and both isomers of cyanonaphthalene:

$$C_6H_5 + CH_2CHC_2H \rightarrow C_{10}H_8 \tag{4.43}$$

$$C_6H_5 + CH_2CHCHCH_2 \rightarrow C_{10}H_{10} + H \tag{4.44}$$

Both reactions are barrierless and exothermic. Following the reaction between phenyl radical and 1,3-butadiene to form dihydronaphthalene ($C_{10}H_{10}$) are two hydrogen abstraction reactions to convert dihydronaphthalene to naphthalene. These hydrogen abstractions are also barrierless. To make both cyanonaphthalene isomers, we have included the following

$$C_{10}H_8 + CN \rightarrow C_{10}CNH_7 + H \tag{4.45}$$

$$C_{10}H_8 + CN \rightarrow C_{10}H_7CN + H \tag{4.46}$$

Both of these reactions are assumed to have equal branching ratios. With just these reactions, adsorption, and desorption on grain surfaces, we get the same results as McGuire et al. (2021), with modeled abundances of naphthalene and both cyanonaphthalene isomers at 2×10^{-17} with respect to hydrogen at 2×10^5 yr. The cyanonaphthalene amounts are more than 6 orders of magnitude less than the observed amount.

In order to remedy this underproduction, we look to grain reactions. Apart from the additional grain reactions that lead to more benzene and therefore more phenyl radical that have been discussed in earlier sections, we add a suite of suprathermal

reactions, specifically:

$$C_{10}H_8 + CN^* \rightarrow C_{10}CNH_7 + H \tag{4.47}$$

$$C_{10}H_8 + CN^* \rightarrow C_{10}H_7CN + H \tag{4.48}$$

Both reactions are assumed to have equal branching ratios, along with the other two of the grain reactions leading to both isomers of cyanonaphthalene:

$$C_6H_5 + C_4H_3CN \rightarrow C_{10}CNH_7 + H, \tag{4.49}$$

$$C_6H_5 + C_4H_3CN \rightarrow C_{10}CNH_7 + H. \tag{4.50}$$

The addition of these reactions leads to the dotted-dashed line in Figure 4.4, producing slightly less than a 2 order of magnitude increase. This brings the abundance of the cyanonaphthalene isomers to 1×10^{-15}, but is still less than the observed amount by 5 orders of magnitude. The complexity of cyanonaphthalene and naphthalene lend itself to more possible pathways to be examined , as there are more ways to add up to 10 carbon compared to simpler molecules like benzene. These models suggest that there are viable energetic grain routes, but thermal routes on the surface also need to be explored. Similarly, there is probably room for expansion in the gas phase as well, as having one possible route is probably not the singular way these molecules are produced in the ISM. Notably, in the gas only model, 1-cyanonaphthalene and 2-cyanonaphthalene have the highest peak abundance of 2×10^{-12}, two orders of mag-

nitude less than the observed amount, suggesting that current gas-phase production routes are the most efficient, unless there are thermal grain production routes that are also efficient. For model RS, while under-producing both cyanonaphthalene isomers compared to the gas-phase only model, we show that sputtering is an efficient way of removing both cyanonaphthalene isomers from the grain ices.

4.4 Astrochemical Implications

In all groups of molecules examined, there are increases in gas abundances in models with expanded chemical networks, radiolysis chemistry, and sputtering. Sputtering is still an efficient non-thermal, non-specific desorption method, though it is more efficient for species that have large abundances within the ice. In this manner, both thermal ice reactions and suprathermal reactions enhance sputtering efficiency. Radiolysis chemistry and suprathermal reactions are still efficient as well, though the most efficient reactions involve abundant ices. Radiolysis and suprathermal pathways are, in general, no replacement for thermal grain reactions, though there may be exceptions; the fast quenching of suprathermal species and comsic ray ionization rate result in suprathermal reactions that cannot outcompete efficient thermal reactions at building up ices. Following this, we report results of the models, and compare them to observed abundances more succinctly than the discussions in prior sections.

For benzonitrile, we see an increase by a factor of 5 between the Model Base and Model Gas, while the increase is an order of magnitude in Model RS, with a calculated gas-phase abundance of 1×10^{-11} at a time of 2×10^{5}. This is approximately the same as in McGuire et al. (2018), as the addition of new reactions from C_6H_5 and C6H6 to more complex molecules such as naphthalene counteract the increases from sputtering

and radiolysis. Suprathermal reactions and sputtering contribute to approaching the observed abundance with a modeled gas-phase abundance 2.8×10^{-11} at 3.5×10^{5} yr. This is less than the observed amount of benzonitrile, 4×10^{-11}, by a factor of 1.4. To increase the gas-phase abundance, apart from sputtering, radiolysis chemistry provides a grain pathway for the production of both benzene and benzonitrile. Further studies are needed to confirm thermal grain pathways, as suprathermal chemistry and sputtering are not efficient enough to fully account for observed levels of benzonitrile. In addition to the enhancements through grain chemistry, re-examination of estimated dissociative recombination reaction, Reaction 4.19, shows that the products of C_6H_2 + $2H_2$ + H should instead be C_6H_5 + H.

In the case of vinyl acetylene, at 2×10^{5} yr, the base model, gas model, and Model RS have gas-phase abundances of 1.8×10^{-11}, 1.1×10^{-10}, and 1.4×10^{-10}, respectively. Model RS is more abundant than the base model and gas model by factors of 7.8 and 1.3, respectively. The observed abundance, from Cernicharo et al. (2021b) is 1.2×10^{-9}, about an order of magnitude more than Model RS. However, Model RS peaks in vinyl acetylene at times later than 10^{6} yr, matching the observed value. The most efficient production methods are through the grain reaction of H and C_4H_3. Sputtering efficiently and significantly contributes to desorbing grain produced vinyl acetylene. Gas reactions between CH and CH_2CCH_2 are also contribute to production.

C_4H_3CN isomers at 2×10^{5} yr have modeled gas abundances of 1.5×10^{-15}, 2.3×10^{-15}, and 1.2×10^{-11}, for models Base, Gas, and RS. The detected abundance for VCA and *trans*-(E)-cyanovinylacetylene in TMC-1 are 1.87×10^{-11} and 2.9×10^{-11}, respectively (Lee et al., 2021). *trans*-(Z)-cyanovinylacetylene has an upper limit to the relative abundance of 2×10^{-11}. For VCA, Model RS replicates observed abundances

within a factor of 1.6, and 2.5 for *trans*-(E)-cyanovinylacetylene. Model RS produces 4 orders of magnitude more C_4H_3CN isomers than the gas phase model and the base model. This enhancement suggests that irradiated grain chemistry may be the primary source of C_4H_3CN isomers, through the hydrogenation of HC_5N and reaction of vinyl acetylene with suprathermal CN. Future work can be done to identify the potential pathways and abundances of the three isomers presented here.

Propargyl radical has been detected in TMC-1 with a fractional abundance of 8.7×10^{-9} (Agúndez et al., 2021). In the models Base, Gas, and RS, propargyl radical has abundances of 4.4×10^{-11}, 8.9×10^{-11}, and 3.3×10^{-10}, respectively. Model RS comes closest to the observed abundance, but is still under-producing propargyl radical by over an order of magnitude. Peak abundances of propargyl radical in model RS at 5.5×10^5 yr are 1.5×10^{-9}, but still less than observed amounts by a factor of 5.8. Even with the additional formation reactions discussed in Agúndez et al. (2021) included in the gas-phase only model, we are unable to replicate their results. Removing the destruction reactions with atomic oxygen give the results presented here. However, also removing the destruction pathways with atomic nitrogen increases peak abundances in the gas-phase model to just under 10^{-9}, and in Model RS to 4.5×10^{-9}. Without atomic nitrogen and oxygen destruction reactions, model RS only under-produces propargyl radical by 2. We are unsure of the differences that cause our gas-phase model to under-produce propargyl radical compared to the results of Agúndez et al. (2021), as their model is gas-phase only as well.

1-cyanonaphthalene and 2-cyanonaphthalene are both observed in TMC-1 with fractional abundances of 7.35×10^{-11} and 7.05×10^{-11}, respectively. The base model produces 1-cyanonaphthalene and 2-cyanonaphthalene with an abundance of 2×10^{-17}. The gas phase model produces 1-cyanonaphthalene with an abundance of 2.2×10^{-15},

and 2-cyanonaphthalene with an abundance of 2.3×10^{-15}. Model RS produce abundances of 10^{-15}, and 1.6×10^{-15} for 1-cyanonaphthalene and 2-cyanonaphthalene, respectfully. Peak values occur in the gas-phase model at a time of 1.3×10^{6}, with abundances of 2.25×10^{-12} for both abundances, still over an order of magnitude under the observed amounts.

4.5 Conclusions

Of the suite of molecules examined in the paper that have been detected toward TMC-1, many abundances are unable to be replicated by three phase gas-grain astrochemical models, as many PAHs and PAH precursors are dependent on mostly gas-phase chemistry. Benzene is relatively unique, because there are grain pathways that have been studied, but are dependant on irradiation to overcome chemical barriers. While this work shows models that take into account chemical effects of radiation which can enhance modeled gas-phase abundances, radiolysis enhanced chemistry is not enough to match modeled abundances to observed amounts. Similarly, sputtering enhances gas abundances, especially for species that are unable to be thermally desorbed, yet have efficient grain pathways to build up large abundances within the grain ices. Of the molecules highlighted in this work, benzonitrile now has a slightly better agreement between models and observations, but at later times can match peak abundances. Vinyl acetylene also has slightly better agreement at the expected time of TMC-1, but at later times match peak abundances. C_4H_3CN isomers are slightly under-produced, but match closest to VCA, and are below the upper limit for *trans*-(Z)-cyanovinylacetylene. In contrast, propargyl radical, 1-cyanonaphthalene, and 2-cyanonaphthalene are still under-produced in models with radiolysis and sputtering

by multiple orders of magnitude.

Future directions should focus on experimental or *ab-initio* methods for grain pathways, as many have yet to be studied, and are estimated. Furthermore, there is a need for further experimental verification of low temperature reactions, as many branching ratios and rate coefficients are still estimated in the chemical networks.

Chapter 5

Conclusions

5.1 Major Conclusions

5.1.1 Chapter 2

We show that radiolysis chemistry can be expanded to more complex species. Prior to this work, the two most complex molecules destroyed by radiolysis were CH_3OH and CH_3COCH_3, with a list of 13 other molecules destroyed through radiolysis, all five atoms or fewer. We expanded radiolysis destruction reactions to include $C_2H_4O_2$ isomers and dimethyl ether. Despite the addition of the radiolysis destruction reactions, the inclusion of radiolysis chemistry increased both grain ice and gas phase abundances of acetic acid, glycolaldehyde, and methyl formate. Glycolaldehyde is also modeled to be at potentially observable abundances in TMC-1. We also showed that not all complex molecules are efficiently formed through radiolysis chemistry, depending on a number of factors:

1. Radiolysis chemistry affects gas-phase abundances for molecules that have large abundances on the ice surface, compared to molecules that are not as abundant on the ice surface.

2. Gas-phase destruction reactions can mitigate increased production of species

produced and desorbed through radiolysis chemistry.

3. There are still large abundances of molecules trapped in the ice, despite the increased desorption through the combination of radiolysis chemistry and reactive desorption.

5.1.2 Chapter 3

We present the physics for sputtering of condensed gases and solids. There are multiple regimes for sputtering, depending on the primary's energy. At energies below cosmic rays ($< 3 \times 10^{-4}$ GeV), sputtering as a result of nuclear collision regimes dominate, with increases as the primary's atomic number increases. We find that this type of sputtering at cosmic ray energies is at least 3 orders of magnitude less than sputtering originating from electronic collisions, despite the majority of energy deposited contributing to events other than sputtering. Nuclear sputtering is generally dependent on the transfer of recoil throughout the surface, and is generally hard to predict theoretically for amorphous, mixed ices, as the recoil is not uniform. For electronic sputtering, we calculated a rate constant through the cosmic ray flux, a cross section derived from electronic stopping power, and a yield, or the number of molecules per electronic collision. The grains are small enough that any cosmic ray colliding with the grain will have enough energy to penetrate the entire grain. Electronic sputtering values were calculated for three different ices: amorphous solid water, amorphous carbon dioxide, and a mixed ice combining values from both water and CO_2 depending on the modeled abundance of each ice. These ices were chosen because they are thought to make up the majority of interstellar ices on dust grains. These values were then applied to all other surface and grain species in the model, as

there is a high probability that water or carbon dioxide will be adjacent to another species, and the structure of the grains allows for one molecule to be sputtered and carry other molecules with it. We then turn our attention to chemical models with and without sputtering, with the following results:

1. Common ices are sputtered at mostly consistent rates, but are not removed at a rate faster than their accretion.

2. Theoretical sputtering treatments for an "average" cosmic ray primary (something with a slightly higher atomic number than a proton) are orders of magnitude less efficient than experimental sputtering caused by lower energy, higher atomic number ions

3. Theoretical sputtering of light ions is still efficient enough to cause orders of magnitude differences in modeled gas-phase abundances, while not significantly altering grain ice abundances.

5.1.3 Chapter 4

Finally, in chapter 4, we include sputtering and radiolysis that have been discussed in recent chapters to a broad discussion on modeling two detected PAHs, 1-cyanonaphthalene and 2-cyanonaphthalene, and a suite of molecules that have potential pathways to form benzene, and from benzene form PAHs. Many of these molecules have had recent detections in TMC-1, such as acetylene, vinyl acetylene, propargyl radical, benzene, naphthalene, and their cyano counterparts: cyanovinyl acetylene, cyanopropargyl radical, benzonitrile, 1-cyanonaphthalene, and 2-cyanonaphthalene. In general, the conclusions we draw are:

1. For species that have multiple thermal gas-phase and grain surface reactions, sputtering and radiolysis do enhance abundances.

2. Sputtering and radiolysis are not efficient enough to take the place of efficient thermal gas and grain reactions in some cases, particularly species without efficient thermal grain production routes.

For the specific molecules examined in this chapter that have been detected in TMC-1:

1. We can closely match observed abundances of benzonitrile in models with radiolysis chemistry and sputtering, when models without these processes under-produce.

2. Vinyl acetylene observed abundances are closely matched by models with radiolysis and sputtering.

3. C_4H_3CN isomers are slightly under-produced, but the isomer that the model best matches the abundances of is vinylcyanoacetylene. Additional work will be needed to separate the different isomers in the network.

4. Propargyl radical is still under-produced in radiolysis and sputtering by more than an order of magnitude, which is an improvement over the base model, which under-produces propargyl radical by more than two orders of magnitude. There are questions about activation energy barriers leading to the destruction of propargyl radical by reaction with atomic nitrogen in the gas phase, but removing them in models still results in under-produced propargyl radical.

5. 1-cyanonaphthalene and 2-cyanonaphthalene are also under-produced by orders of magnitude. While radiolysis and sputtering enhance modeled abundances by

orders of magnitude, due to the complexity of naphthalene, it is probable that we are missing additional thermal and excited state pathways, both on grain surfaces, and in the gas phase.

5.2 Future Work

5.2.1 Radiolysis

General improvements to radiolysis are still able to be done, not all surface species in the network are affected by radiolysis, however, not all species have the data available to estimate values needed to calculate radiolysis rates. Included in prior chapters but fully discussed was the inclusion of radiolysis of nitrogen bearing species. While this improves the abundance of cyano-bearing species, more work can be done in the formation of amino acids and other similar classes of molecules. Ioppolo et al. (2021) proposed a non-energetic method to glycine in cold clouds, but other nitrogen bearing compounds may benefit from energetic chemistry. Recently, excited (^{1}D) oxygen insertion reactions have been studied with respect to interstellar chemistry (Carder et al. (Submitted)). There may be similar insertion reactions for excited carbon and nitrogen that can be generated through radiolysis. Similar to nitrogen chemistry, there are many unanswered questions about sulfur in the interstellar medium, particularly about depletion onto grains, and gaseous forms. Perhaps radiolysis chemistry can be applied to grain sulfur bearing compounds. Additionally, the assumption that grain ices do not contain ions warrants further research. While grains themselves are observed to be negative, the presence of ions in the ice can be possible depending on the number of free electrons on the grain surface. While we assume that the electrons

ionized from cosmic ray collisions immediately recombine with cations, some species may remain ionic.

5.2.2 Sputtering

Similar to radiolysis chemistry, there are many improvements to sputtering. While currently applied to all species in the model, rate coefficients are based on water, carbon dioxide, or a combination of both. Bragg's law can be included to calculate stopping powers for each species based on its constituent elements, but converting those to cross sections for individual species would require individual energy loss due to heat based on the species, and even then, that assumes that mixed astrochemical ices would be sputtered in the same way as uniform ices. Another aspect needs further examination is higher atomic number sputtering. As previously stated, sputtering experiments of high Z ions into water ice are orders of magnitude more efficient at sputtering compared to the theoretical results of hydrogen, both for electronic sputtering regimes and nuclear sputtering. Future work may, instead of averaging all cosmic rays into one cosmic ray-grain interaction rate, separate the rate into ions above and below some atomic number. While the treatment of the high Z interactions may be less physical when applied to rate-equation based models, there may still be valuable contributions from such considerations. Additionally, this type of collision would be well suited to molecular dynamics or Monte Carlo simulations, to examine this on the microscopic level.

5.2.3 General Surface Improvements

For improvements in the model that are not specific to sputtering and radiolysis, there are multiple areas of research that are ongoing. Kalvāns (2018) and Kalvāns & Kalnin (2020b) discuss more complex treatments of cosmic ray grain heating and cooling, compared to the current treatment in `Nautilus` (Hasegawa & Herbst, 1993). In `Nautilus`, as part of an unfinished paper, is an implementation of the heating regimes found in Kalvāns (2018) that generally enhance cosmic ray heating, more frequently to lower temperatures, as a result of hydrogen cosmic rays, combined with the greater temperature increase of heavier, but less frequent, high Z cosmic rays. Evaporative cooling treatments could also be considered for common inclusion into models when coupled with cosmic ray whole grain heating (Kalvāns & Kalnin, 2020b,a).

Another effect of cosmic rays that is well documented in planetary sciences is physically changing the structure of solids due to high energy irradiation (Behrisch & Eckstein, 2007; Ghesquière et al., 2018). This has understood effects from ices on planetary bodies, like Pluto and Titan (Feniou et al., 2020; Zhou et al., 2010), to effects on nuclear fuel and reactor design (Groopman et al., 2021). Interstellar ices, on the other hand, are just starting to also account for physical processing of ices, and the role of pores within the interstellar ice (Christianson & Garrod, 2021). Kalvāns & Silsbee (2022) discusses the possibility of desorption and ice altering from interstellar grain collisions. The possibilities around continuously changing physical condition of ices could open new pathways within the bulk of the ice, where molecules are assumed to be stationary, and thus are limited to reacting with their nearest neighbors, along with possible desorption from the bulk.

While grain heating by cosmic rays has been shown to help desorption, temporarily heating the grains can cause temporarily enhanced thermal diffusion, or even temporarily more efficient thermal reactions. While the timescale of increased temperatures on grains is expected to be short (on the order of 10^{-5} s), which will probably not influence diffusion limited reactions. Heating may effect reactions where reactants are already close to each to each other, similar to the fast suprathermal reactions discussed throughout this thesis and in . There are similar fast reactions described in Jin & Garrod (2020), where a molecule is excited by some external factor, and then immediately react with its closest neighbor. This type of reaction is a good match for Monte Carlo simulations, where the grain structure is explicitly known and kept track of, though there are implementations of this type of reaction in rate-equation models.

Apart from new types of reactions and physical processes, there need to be further experimental and ab initio studies of thermal reactions. Chapter 4 explores novel pathways that may be efficient on grain surfaces, however, many of these reactions are not experimentally verified and may not be viable on surfaces, and are just based on abundances of surface species and their binding energies, hence the need for experimental or theoretical verification of energetics and barriers. Additionally, while many reactions have been studied under gas-phase conditions, surface reactions may not proceed the same as gas reactions. Surfaces have been shown to both catalyze and inhibit reactions, depending on the surface and the reactants (Perrero et al., 2022; Enrique-Romero et al., 2019).

Bibliography

Abplanalp M. J., Kaiser R. I., 2020, ApJ, 889, 3

Abplanalp M. J., Borsuk A., Jones B. M., Kaiser R. I., 2015, The Astrophysical Journal, 814, 45

Abplanalp M. J., Gozem S., Krylov A. I., Shingledecker C. N., Herbst E., Kaiser R. I., 2016, PNAS, 113, 7727

Adusei G. Y., Blue A. S., Fontijn A., 1996, J. Phys. Chem., 100, 16921

Agundez M., Marcelino N., Tercero B., Cabezas C., de Vicente P., Cernicharo J., 2021, arXiv:2104.11506 [astro-ph]

Agúndez M., Marcelino N., Cernicharo J., Roueff E., Tafalla M., 2019, A&A, 625, A147

Agúndez M., Cabezas C., Tercero B., Marcelino N., Gallego J. D., Vicente P. d., Cernicharo J., 2021, A&A, 647, L10

Andersen H. H., Bay H. L., 1981, in Behrisch R., ed., Topics in Applied Physics, Sputtering by Particle Bombardment I: Physical Sputtering of Single-Element Solids. Springer, Berlin, Heidelberg, pp 145–218, doi:10.1007/3540105212_9, https://doi.org/10.1007/3540105212_9

Arumainayagam C. R., et al., 2019, Chemical Society Reviews, 48, 2293

Bacmann A., Faure A., 2015, EAS Publications Series, 75-76, 325

Bacmann A., Taquet V., Faure A., Kahane C., Ceccarelli C., 2012, A&A, 541, L12

Balucani N., Ceccarelli C., Taquet V., 2015, Monthly Notices of the Royal Astronomical Society, 449, L16

Banks P. M., Kockarts G., 1973, Aeronomy.. https://ui.adsabs.harvard.edu/abs/1973aero.book.....B

Behrisch R., Eckstein W., 2007, Sputtering by Particle Bombardment: Experiments and Computer Calculations From Threshold to MeV Energies. Topics in applied physics, Springer, Berlin

Belloche A., Menten K. M., Comito C., Müller H. S. P., Schilke P., Ott J., Thorwirth S., Hieret C., 2008, A&A, 482, 179

Belloche A., Garrod R. T., Müller H. S. P., Menten K. M., Medvedev I., Thomas J., Kisiel Z., 2019, Astronomy and Astrophysics, 628, A10

Bennett C. J., Kaiser R. I., 2007a, ApJ, 660, 1289

Bennett C. J., Kaiser R. I., 2007b, The Astrophysical Journal, 661, 899

Bennett C. J., Osamura Y., Lebar M. D., Kaiser R. I., 2005, ApJ, 634, 698

Berger M. J., Coursey J. S., Zucker M. A., 1999

Berné O., Montillaud J., Joblin C., 2015, A&A, 577, A133

Bertin M., et al., 2013, The Astrophysical Journal, 779, 120

Bethe H., 1932, Z. Physik, 76, 293

Blagojevic V., Petrie S., Bohme D. K., 2003, Monthly Notices of the Royal Astronomical Society, 339, L7

Blasi P., 2013, Astron Astrophys Rev, 21, 70

Boschini M., Rancoita P., Tacconi M., 2014, Screened Relativistic (SR) Treatment for Calculating the Displacement Damage and Nuclear Stopping Powers for Electrons, Protons, Light- and Heavy- Ions in Materials, http://www.sr-niel.org/

Bouwman J., Goulay F., Leone S. R., Wilson K. R., 2012, J. Phys. Chem. A, 116, 3907

Box G. E. P., Draper N. R., 1987, Empirical Model-building and Response Surfaces. Wiley series in probability and mathematical statistics. Applied probability and statistics, Wiley, New York

Box G. E., Luceño A., Paniagua-Quinones M. d. C., Wiley Online Library UBCM Engineering Wiley Online Library UBCM Math & Statistics Wiley Online Library UBCM German Language Wiley Online Library UBCM All Obooks 2009, Statistical Control by Monitoring and Feedback Adjustment. John Wiley & Sons, Hoboken, N.J., http://RE5QY4SB7X.search.serialssolutions.com/?V=1.0&L=RE5QY4SB7X&S=JCs&C=TC0000550643&T=marc

Boyer M. C., Rivas N., Tran A. A., Verish C. A., Arumainayagam C. R., 2016, Surface Science, 652, 26

Brown W. L., Johnson R. E., 1986, Nuclear Instruments and Methods in Physics Research Section B: Beam Interactions with Materials and Atoms, 13, 295

Brown R. D., Crofts J. G., Gardner F. F., Godfrey P. D., Robinson B. J., Whiteoak J. B., 1975, The Astrophysical Journal Letters, 197, L29

Brown W. L., Lanzerotti L. J., Poate J. M., Augustyniak W. M., 1978, Phys. Rev. Lett., 40, 1027

Brown W. L., Augustyniak W. M., Lanzerotti L. J., Johnson R. E., Evatt R., 1980, Phys. Rev. Lett., 45, 1632

Brown W. L., et al., 1982, Nuclear Instruments and Methods in Physics Research, 198, 1

Burkhardt A. M., et al., 2021, ApJL, 913, L18

Canosa A., Páramo A., Le Picard S. D., Sims I. R., 2007, Icarus, 187, 558

Carroll P. B., Drouin B. J., Weaver S. L. W., 2010, ApJ, 723, 845

Caster K. L., Selby T. M., Osborn D. L., Le Picard S. D., Goulay F., 2021, J. Phys. Chem. A, 125, 6927

Cernicharo J., Marcelino N., Roueff E., Gerin M., Jiménez-Escobar A., Muñoz Caro G. M., 2012, The Astrophysical Journal Letters, 759, L43

Cernicharo J., Marcelino N., Agúndez M., Bermúdez C., Cabezas C., Tercero B., Pardo J. R., 2020, A&A, 642, L8

Cernicharo J., et al., 2021a, A&A, 647, L2

Cernicharo J., Agúndez M., Kaiser R. I., Cabezas C., Tercero B., Marcelino N., Pardo J. R., de Vicente P., 2021b, Astronomy and Astrophysics, 652, L9

Cesarsky C. J., Volk H. J., 1978, Astronomy and Astrophysics, 70, 367

Chang Q., Herbst E., 2016, ApJ, 819, 145

Charnley S. B., Tielens A. G. G. M., Millar T. J., 1992, The Astrophysical Journal, 399, L71

Christianson D. A., Garrod R. T., 2021, Front. Astron. Space Sci., 8, 643297

Chuang K.-J., Fedoseev G., Ioppolo S., van Dishoeck E. F., Linnartz H., 2016, Mon Not R Astron Soc, 455, 1702

Clements A. R., Berk B., Cooke I. R., Garrod R. T., 2018, Physical Chemistry Chemical Physics, 20, 5553

Cummings A. C., et al., 2016, ApJ, 831, 18

Dalgarno A., Griffing G. W., Bates D. R., 1958, Proceedings of the Royal Society of London. Series A. Mathematical and Physical Sciences, 248, 415

Dartois E., et al., 2013, Astronomy and Astrophysics, 557, A97

Dartois E., et al., 2015a, Nuclear Instruments and Methods in Physics Research Section B: Beam Interactions with Materials and Atoms, 365, 472

Dartois E., et al., 2015b, A&A, 576, A125

Dartois E., Chabot M., Barkach T. I., Rothard H., Auge B., Agnihotri A. N., Domaracka A., Boduch P., 2018, Astron. Astrophys., 618, A173

Dartois E., Chabot M., Barkach T. I., Rothard H., Augé B., Agnihotri A. N., Domaracka A., Boduch P., 2019, A&A, 627, A55

Daugey N., Caubet P., Retail B., Costes M., Bergeat A., Dorthe G., 2005, Phys. Chem. Chem. Phys., 7, 2921

Ehrenfreund P., Charnley S. B., 2000, Annual Review of Astronomy and Astrophysics, 38, 427

Ellder J., et al., 1980, The Astrophysical Journal Letters, 242, L93

Enrique-Romero J., Rimola A., Ceccarelli C., Balucani N., 2016, Mon Not R Astron Soc Lett, 459, L6

Enrique-Romero J., Rimola A., Ceccarelli C., Ugliengo P., Balucani N., Skouteris D., 2019, ACS Earth and Space Chemistry, 3, 2158

Enrique-Romero J., Ceccarelli C., Rimola A., Skouteris D., Balucani N., Ugliengo P., 2021, Astronomy and Astrophysics, 655, A9

Fedoseev G., Cuppen H. M., Ioppolo S., Lamberts T., Linnartz H., 2015, Mon Not R Astron Soc, 448, 1288

Feniou C., et al., 2020,] 10.5194/epsc2020-828, pp EPSC2020–828

Fuchs G. W., Cuppen H. M., Ioppolo S., Romanzin C., Bisschop S. E., Andersson S., Dishoeck E. F. v., Linnartz H., 2009, A&A, 505, 629

Fueki K., Magee J. L., 1963, Discuss. Faraday Soc., 36, 19

Gades H., Urbassek H. M., 1995, Nuclear Instruments and Methods in Physics Research Section B: Beam Interactions with Materials and Atoms, 103, 131

Garrod R. T., 2013, ApJ, 765, 60

Garrod R. T., Herbst E., 2006, A&A, 457, 927

Garrod R. T., Wakelam V., Herbst E., 2007, A&A, 467, 1103

Garrod R. T., Weaver S. L. W., Herbst E., 2008, ApJ, 682, 283

Ghesquière P., Ivlev A., Noble J. A., Theulé P., 2018, Astronomy and Astrophysics, 614, A107

Graedel T. E., McGill R., 1982, Science, 215, 1191

Graedel T. E., Langer W. D., Frerking M. A., 1982, The Astrophysical Journal Supplement Series, 48, 321

Groopman E. E., Nittler L. R., Willingham D. G., Meshik A. P., Pravdivtseva O. V., 2021, Applied Geochemistry, 131, 105047

Hamberg M., et al., 2011,] 10.1051/EAS/1146026

Hasegawa T. I., Herbst E., 1993, Monthly Notices of the Royal Astronomical Society, 261, 83

Hasegawa T. I., Herbst E., Leung C. M., 1992, The Astrophysical Journal Supplement Series, 82, 167

Herbst E., 2021, Frontiers in Astronomy and Space Sciences, 8

Herbst E., Klemperer W., 1973, The Astrophysical Journal, 185, 505

Herbst E., Klemperer W., 1976, Physics Today, 29, 32

Herbst E., Millar T. J., 2008, in , Low Temperatures and Cold Molecules. PUBLISHED BY IMPERIAL COLLEGE PRESS AND DISTRIBUTED BY WORLD SCIENTIFIC PUBLISHING CO., pp 1–54, doi:10.1142/9781848162105_0001, http://www.worldscientific.com/doi/abs/10.1142/9781848162105_0001

Herbst E., van Dishoeck E. F., 2009, Annu. Rev. Astron. Astrophys., 47, 427

Hewage D., Silva R., Yang D.-S., 2012, 67th International Symposium on Molecular Spectroscopy, p. TD03

Hincelin U., Wakelam V., Hersant F., Guilloteau S., Loison J. C., Honvault P., Troe J., 2011, A&A, 530, A61

Hollis J. M., Lovas F. J., Jewell P. R., 2000, The Astrophysical Journal Letters, 540, L107

Hudson R. L., Moore M. H., Cook A. M., 2005, Advances in Space Research, 36, 184

Huntress Jr. W. T., Mitchell G. F., 1979, The Astrophysical Journal, 231, 456

Indriolo N., Hobbs L. M., Hinkle K. H., McCall B. J., 2009, ApJ, 703, 2131

Ioppolo S., et al., 2021, Nature Astronomy, 5, 197

Iqbal W., Wakelam V., 2018, Astron. Astrophys., 615, A20

Jenkins E. B., 2009, ApJ, 700, 1299

Jiménez-Serra I., et al., 2016, ApJL, 830, L6

Jin M., Garrod R. T., 2020, The Astrophysical Journal Supplement Series, 249, 26

Johnson R. E., 1982, Introduction to atomic and molecular collisions. https://ui.adsabs.harvard.edu/abs/1982itam.book.....J

Johnson R. E., 1990, Energetic Charged-Particle Interactions with Atmospheres and Surfaces, X, 232 pp. 84 figs., 28 tabs.. Springer-Verlag Berlin Heidelberg New York. Also Physics and Chemistry in Space, volume 19

Johnson R. E., Brown W. L., 1982, Nuclear Instruments and Methods in Physics Research, 198, 103

Jones B. M., Zhang F., Kaiser R. I., Jamal A., Mebel A. M., Cordiner M. A., Charnley S. B., 2011, Proceedings of the National Academy of Sciences, 108, 452

Jose J., Zamir A., Stein T., 2021, Proceedings of the National Academy of Sciences, 118, e2101371118

Kaiser R. I., Vereecken L., Peeters J., Bettinger H. F., Schleyer P. v. R., Schaefer H. F., 2003, Astronomy and Astrophysics, 406, 385

Kalvāns J., 2018, ApJS, 239, 6

Kalvāns J., Kalnin J. R., 2019, Monthly Notices of the Royal Astronomical Society, 486, 2050

Kalvāns J., Kalnin J. R., 2020a, A&A, 633, A97

Kalvāns J., Kalnin J. R., 2020b, A&A, 641, A49

Kalvāns J., Silsbee K., 2022, Monthly Notices of the Royal Astronomical Society, 515, 785

Keller-Rudek H., Moortgat G. K., Sander R., Sörensen R., 2013, Earth System Science Data, 5, 365

Krasnokutski S. A., Huisken F., Jäger C., Henning T., 2017, The Astrophysical Journal, 836, 32

Kuan Y.-J., Charnley S. B., Huang H.-C., Tseng W.-L., Kisiel Z., 2003, The Astrophysical Journal, 593, 848

Laas J. C., Garrod R. T., Herbst E., Widicus Weaver S. L., 2011, The Astrophysical Journal, 728, 71

Lee K. L. K., et al., 2021, arXiv e-prints, 2101, arXiv:2101.05858

Lias S. G., Bartmess J. E., Liebman J. F., Holmes J. L., Levin R. D., Mallard W. G., 2020, in , NIST Chemistry WebBook, NIST Standard Reference Database Number 69. National Institute of Standards and Technology, Gaithersburg MD, 20899, https://doi.org/10.18434/T4D303

Lifshit A., Cohen Y., Braun-Unkhoff M., Frank P., ,] 10.1016/S0082-0784(96)80273-6, 26, 659

McGuire B. A., 2022, ApJS, 259, 30

McGuire B. A., Burkhardt A. M., Kalenskii S., Shingledecker C. N., Remijan A. J., Herbst E., McCarthy M. C., 2018, Science, 359, 202

McGuire B. A., et al., 2021, Science, 371, 1265

Mehringer D. M., Snyder L. E., Miao Y., Lovas F. J., 1997, ApJ, 480, L71

Michael J. V., Lee J. H., 1977, Chemical Physics Letters, 51, 303

Minissale M., et al., 2013, Physical Review Letters, 111, 053201

Minissale M., Dulieu F., Cazaux S., Hocuk S., 2016, A&A, 585, A24

Neufeld D. A., Wolfire M. G., Schilke P., 2005, ApJ, 628, 260

Parker J. K., Payne W. A., Cody R. J., Stief L. J., 2004, J. Phys. Chem. A, 108, 1938

Paulive A., Shingledecker C. N., Herbst E., 2021, Monthly Notices of the Royal Astronomical Society, 500, 3414

Paulive A., Carder J. T., Herbst E., 2022, Monthly Notices of the Royal Astronomical Society, p. stac2507

Perrero J., Enrique-Romero J., Martínez-Bachs B., Ceccarelli C., Balucani N., Ugliengo P., Rimola A., 2022, ACS Earth and Space Chemistry, 6, 496

Platzman R. L., 1955, Radiation Research, 2, 1

Remijan A., Snyder L. E., Liu S.-Y., Mehringer D., Kuan Y.-J., 2002, ApJ, 576, 264

Remijan A., Snyder L. E., Friedel D. N., Liu S.-Y., Shah R. Y., 2003, ApJ, 590, 314

Remijan A., Shiao Y.-S., Friedel D. N., Meier D. S., Snyder L. E., 2004, ApJ, 617, 384

Rimola A., Skouteris D., Balucani N., Ceccarelli C., Enrique-Romero J., Taquet V., Ugliengo P., 2018, ACS Earth Space Chem., 2, 720

Rook F. L., Johnson R. E., Brown W. L., 1985, Surface Science, 164, 625

Rothard H., Domaracka A., Boduch P., Palumbo M. E., Strazzulla G., Silveira E. F. d., Dartois E., 2017, J. Phys. B: At. Mol. Opt. Phys., 50, 062001

Ruaud M., Loison J. C., Hickson K. M., Gratier P., Hersant F., Wakelam V., 2015, Mon Not R Astron Soc, 447, 4004

Ruaud M., Wakelam V., Hersant F., 2016, Monthly Notices of the Royal Astronomical Society, 459, 3756

Schou J., 1980, Phys. Rev. B, 22, 2141

Shingledecker C. N., Herbst E., 2018, Phys. Chem. Chem. Phys., 20, 5359

Shingledecker C. N., Molpeceres G., Rivilla V. M., Majumdar L., Kästner J., ,] 10.3847/1538-4357/ab94b5, 897, 158

Shingledecker C. N., Le Gal R., Herbst E., 2017, Physical Chemistry Chemical Physics (Incorporating Faraday Transactions), 19, 11043

Shingledecker C. N., Tennis J., Gal R. L., Herbst E., 2018, ApJ, 861, 20

Shingledecker C. N., Vasyunin A., Herbst E., Caselli P., 2019a, The Astrophysical Journal, 876, 140

Shingledecker C. N., Álvarez Barcia S., Korn V. H., Kästner J., 2019b, ApJ, 878, 80

Shingledecker C. N., Lamberts T., Laas J. C., Vasyunin A., Herbst E., Kästner J., Caselli P., 2020, ApJ, 888, 52

Sigmund P., 1969, Physical Review, 184, 383

Skouteris D., Balucani N., Ceccarelli C., Vazart F., Puzzarini C., Barone V., Codella C., Lefloch B., 2018, ApJ, 854, 135

Soma T., Sakai N., Watanabe Y., Yamamoto S., 2018, ApJ, 854, 116

Spinks J. W. T., Woods R. J., 1990, An Introduction to Radiation Chemistry, 3rd ed edn. Wiley, New York, https://search.lib.virginia.edu/catalog/u2887205

Spitzer Jr. L., Tomasko M. G., 1968, Astrophysical Journal, vol. 152, p.971, 152, 971

Swings P., Rosenfeld L., 1937, ApJ, 86, 483

Taquet V., Wirström E. S., Charnley S. B., Faure A., López-Sepulcre A., Persson C. M., 2017, Astronomy and Astrophysics, 607, A20

Tennis J., Loison J.-C., Herbst E., 2021, The Astrophysical Journal, 922, 133

Tielens A. G. G. M., 2008, Annual Review of Astronomy and Astrophysics, 46, 289

Townsend L. W. T., 1993, Technical report, Comparisons of cross-section predictions for relativistic iron and argon beams with semiempirical fragmentation models, https://ntrs.nasa.gov/search.jsp?R=19930017921. https://ntrs.nasa.gov/search.jsp?R=19930017921

Vastel C., Ceccarelli C., Lefloch B., Bachiller R., 2014, ApJL, 795, L2

Vasyunin A. I., Herbst E., 2013a, The Astrophysical Journal, 762, 86

Vasyunin A. I., Herbst E., 2013b, ApJ, 769, 34

Wakelam V., Herbst E., 2008, The Astrophysical Journal, 680, 371

Wakelam V., et al., 2012, ApJS, 199, 21

Wakelam V., Dartois E., Chabot M., Spezzano S., Navarro-Almaida D., Loison J.-C., Fuente A., 2021, arXiv:2106.08621 [astro-ph]

Watanabe N., Kouchi A., 2002, The Astrophysical Journal Letters, 571, L173

Whittet D. C. B., et al., 1996, åp, 315, L357

Woods P. M., Millar T. J., Zijlstra A. A., Herbst E., 2002, The Astrophysical Journal, 574, L167

Woods P. M., Kelly G., Viti S., Slater B., Brown W. A., Puletti F., Burke D. J., Raza Z., 2012, ApJ, 750, 19

Woods P. M., Slater B., Raza Z., Viti S., Brown W. A., Burke D. J., 2013, ApJ, 777, 90

Xue C., Remijan A. J., Burkhardt A. M., Herbst E., 2019a, ApJ, 871, 112

Xue C., Remijan A. J., Brogan C. L., Hunter T. R., Herbst E., McGuire B. A., 2019b, The Astrophysical Journal, 882, 118

Yang D. L., Yu T., Wang N. S., Lin M. C., 1992, Chemical Physics, 160, 317

Zhou L., Zheng W., Kaiser R. I., Landera A., Mebel A. M., Liang M.-C., Yung Y. L., 2010, ApJ, 718, 1243

Zhou L., Maity S., Abplanalp M., Turner A., Kaiser R. I., 2014, ApJ, 790, 38

van Dishoeck E. F., Black J. H., 1988,] 10.1007/978-94-009-3007-0_15, 146, 209

Öberg K. I., van Dishoeck E. F., Linnartz H., 2009, Astronomy and Astrophysics, 496, 281

Öberg K. I., Bottinelli S., Jørgensen J. K., van Dishoeck E. F., 2010, ApJ, 716, 825

Appendices

Appendix A

Supplementary material from Chapter 2

Supplementary material referred to in Chapter 2 can be found published as Supplementary Material from Paulive et al. (2021).

Appendix B

Enhanced Sputtering and additional tables to environments other than TMC-1 for Chapter 3

Appendix B includes large figures and tables that are repetitive, but still contain relevant information to Chapter 3, due to slight variations in models. The large figures show ice abundances of common species, with surface ices denoted with a "J", and bulk ices identified with a "K". We find that these ices are less affected by sputtering compared to other ices because of greater fractional abundances. The more abundant molecules have less of a noticeable increase in desorption compared to ices with a lower abundance. The tables contain fractional abundances and column densities for B1-b, L483, L1989b, and Barnard 5.

Table B.1: List of observed column densities in cm^{-2} for selected molecules toward B1-b, with a reported H_2 column density of 10^{23} cm^{-2} (Cernicharo et al., 2012).

Compound	Column Density	Fractional Abundance
CH_3OH[a]	3.6×10^{14}	3.608×10^{-9}
CH_3CHO[a]	5.4×10^{12}	3.9×10^{-11}
$HCOOCH_3$[a]	8.3×10^{12}	8.3×10^{-11}
CH_3OCH_3[b]	3.0×10^{12}	2.5×10^{-10}

a (Öberg et al., 2010)
b (Cernicharo et al., 2012)

Table B.2: List of observed column densities in cm^{-2} for selected molecules toward L483. All observed abundances are from Agúndez et al. (2019), and with a H_2 column density of approximately 4×10^{23} cm^{-2}

L483		
Compound	Column Density	Fractional Abundance
CH_3OH	2.9×10^{13}	7.25×10^{-9}
CH_3CHO	3.8×10^{12}	9.5×10^{-11}
$HCOOCH_3$	2.3×10^{12}	5.7×10^{-11}
CH_3OCH_3	5.3×10^{12}	1.32×10^{-10}

Table B.3: List of observed column densities in cm^{-2} for selected molecules toward L1989B. The reported H_2 column density is 4×10^{23} cm^{-2}. Methanol detection is from Bacmann & Faure (2015) and other abundances are from Bacmann et al. (2012).

L1989B		
Compound	Column Density	Fractional Abundance
CH_3OH	1.2×10^{14}	1.2×10^{-9}
CH_3CHO	9.0×10^{12}	9.0×10^{-11}
$HCOOCH_3$	5.91×10^{12}	5.91×10^{-11}
CH_3OCH_3	4.6×10^{12}	5.91×10^{-11}

Table B.4: List of observed column densities in cm^{-2} for selected molecules toward Barnard 5, H_2 column density of 10^{21} cm^{-2} (Taquet et al., 2017).

Barnard 5		
Compound	Column Density	Fractional Abundance
CH_3OH	1.5×10^{14}	4.5×10^{-8}
CH_3CHO	5.2×10^{12}	1.6×10^{-9}
$HCOOCH_3$	4.3×10^{12}	1.3×10^{-9}
CH_3OCH_3	2.1×10^{12}	7.0×10^{-10}

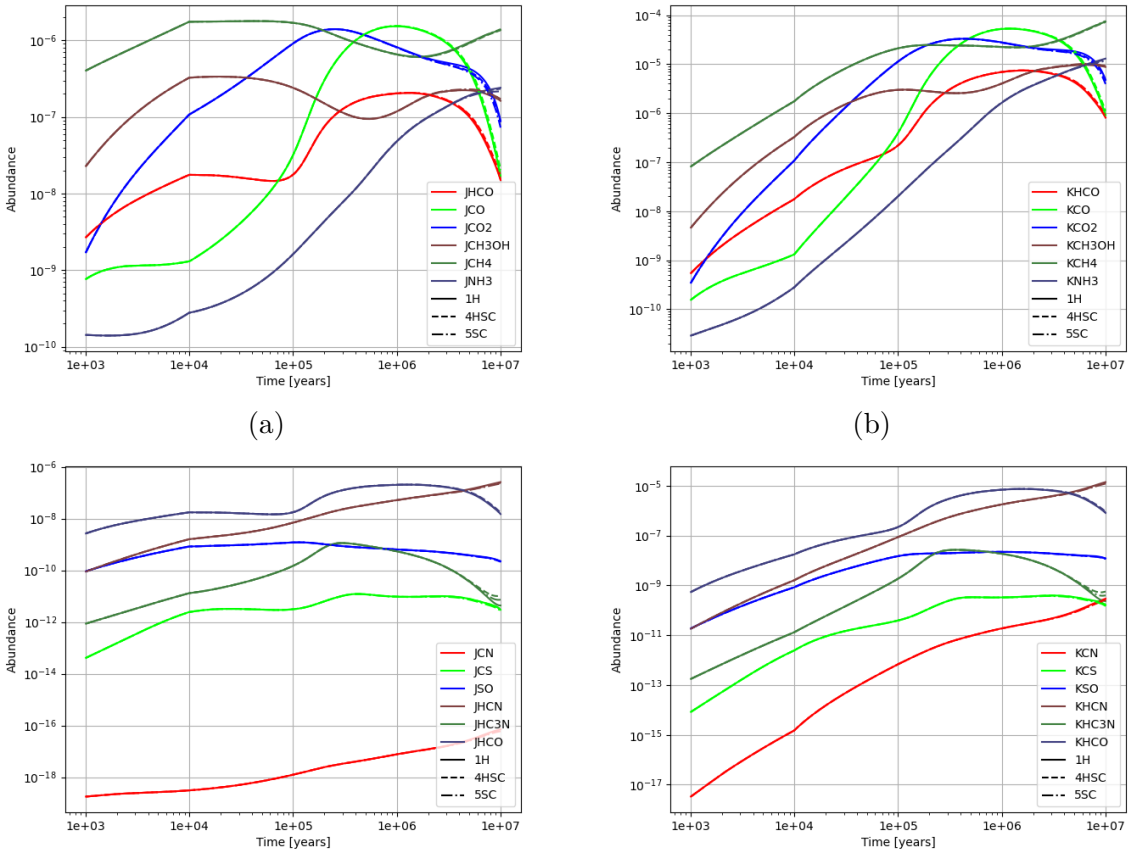

Figure B.1: Fractional abundance graphs of various ice species with respect to hydrogen. At the right are the surface abundances of select species, at the left are the bulk abundances. Individual species are a specific colour.At the top are common ices, while the bottom shows simple ices. Model 1H, without sputtering, is a solid line, models 4HSC and 5SC are dashed and dotted-dashed lines, respectively. Notable in these figures is that the ice abundances are not significantly affected by sputtering, showing that sputtering is not fast enough to significantly deplete ices on the grain surface, even with an increased rate coefficient for sputtering of CO_2 ices.

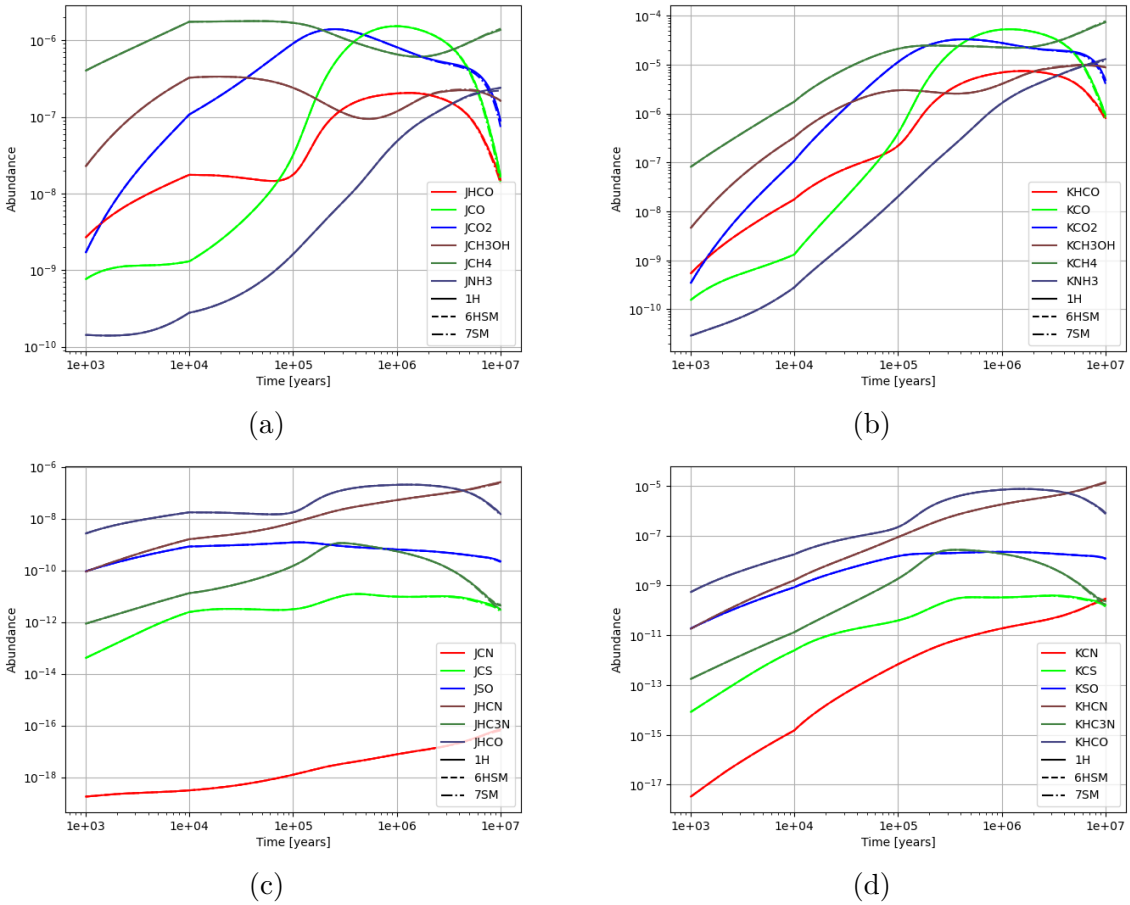

Figure B.2: Fractional abundance graphs of various common ices with respect to hydrogen. At the right are the surface abundances of select species, at the left are the bulk abundances. Individual species are a specific colour. At the top are common ices, while the bottom is simple molecules. Model 1H, without sputtering, is a solid line, models 6HSM and 7SM are dashed and dotted-dashed lines, respectively. Notable in these figures is that the ice abundances are not significantly affected by sputtering, despite the increased sputtering rate coefficient of a mixed ice.

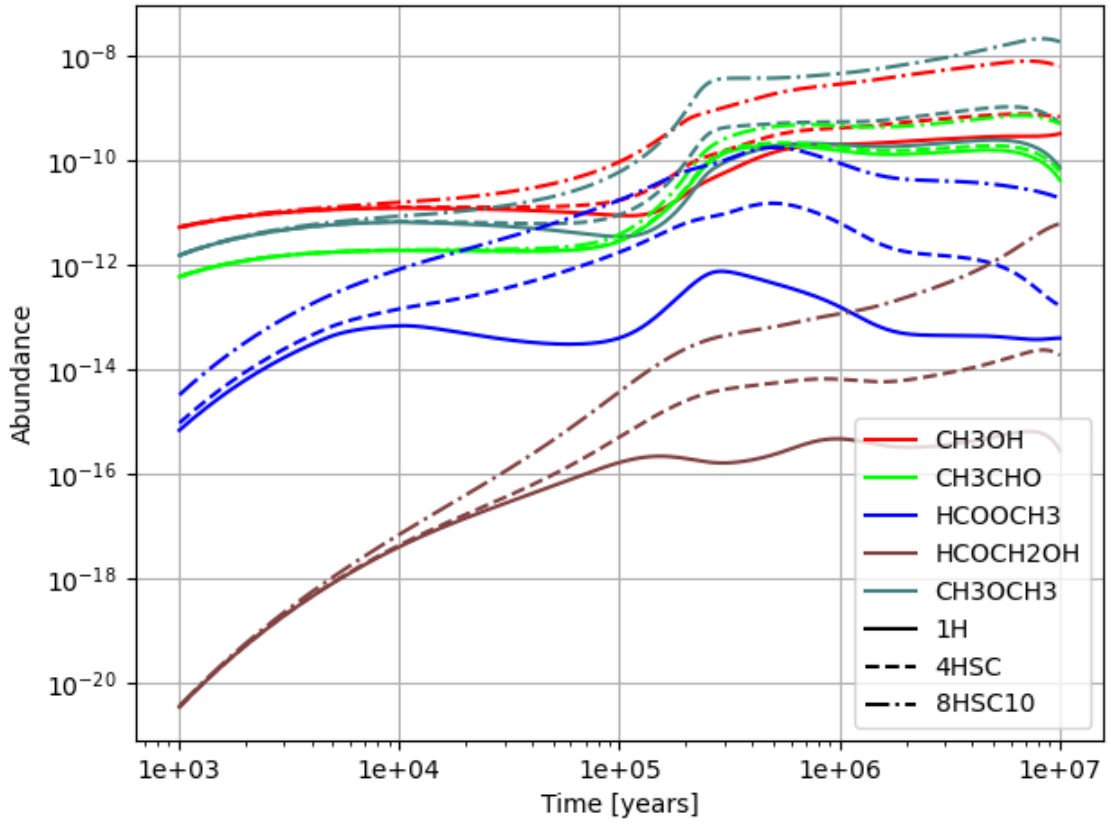

Figure B.3: Plot of the fractional gas-phase abundance of various COMs with respect to hydrogen. Different species are different colours, the solid lines are model 1H, the dashed lines are model 4HSC, and the dotted-dashed lines are model 8HSC10, a model with 10 times the rate coefficient of sputtering in model 4HSC. The resulting rate of sputtering for carbon dioxide ices in model 8HSC10 is 1.42×10^{-15} cm^{-3} s^{-1}.

Appendix C

Additional Radiolysis Reactions relevant to Chapter 4

This table lists the new radiolysis reactions utilized in Chapter 4. All reactions apply to both surface and bulk ices. Branching ratios are assumed to be equal, products are based on photodissociation products.

Reactants	Products	Branching Ratio	Type
C_6H_6			
C_6H_6 + Cosmic Ray (CR)	$\rightsquigarrow C_6H_5^* + H^*$	0.500	1
	$\rightsquigarrow C_6H_4^* + H_2^*$	0.500	1
	$\rightsquigarrow C_6H_5 + H$	0.500	2
	$\rightsquigarrow C_6H_4 + H_2$	0.500	2
	$\rightsquigarrow C_6H_6^*$	1	3
$C_{10}H_8$			
$C_{10}H_8$ + CR	$\rightsquigarrow C_6H_5^* + C_4H_3^*$	0.500	1
	$\rightsquigarrow C_6H_4^* + CH_2CHC_2H^*$	0.500	1
	$\rightsquigarrow C_6H_5 + C_4H_3$	0.500	2
	$\rightsquigarrow C_6H_4 + CH_2CHC_2H$	0.500	2
	$\rightsquigarrow C_{10}H_8^*$	1	3

Table C.1: Table of new suprathermal reactions of aromatic species discussed in Chapter 4. All reactions are for both surface ices and bulk ices.

Reactants	Products	Branching Ratio	Type
HCN			
HCN + Cosmic Ray (CR)	$\rightsquigarrow CN^* + H^*$	0.333	1
	$\rightsquigarrow N^* + CH^*$	0.333	1
	$\rightsquigarrow C^* + NH^*$	0.333	1
	$\rightsquigarrow CN + H$	1	2
	$\rightsquigarrow HCN^*$	1	3
HNC			
HNC + CR	$\rightsquigarrow CN^* + H^*$	0.333	1
	$\rightsquigarrow N^* + CH^*$	0.333	1
	$\rightsquigarrow C^* + NH^*$	0.333	1
	$\rightsquigarrow CN + H$	1	2
	$\rightsquigarrow HNC^*$	1	3
H_2CN			
H_2CN + CR	$\rightsquigarrow CN^* + H_2^*$	0.250	1
	$\rightsquigarrow HCN^* + H^*$	0.250	1
	$\rightsquigarrow CH_2^* + N^*$	0.250	1
	$\rightsquigarrow NH_2^* + C^*$	0.250	1
	$\rightsquigarrow CN + H_2$	0.5	2
	$\rightsquigarrow HCN + H$	0.5	2
	$\rightsquigarrow H_2CN^*$	1	3
H_2CCN			
H_2CCN + CR	$\rightsquigarrow CN^* + CH_2^*$	0.333	1
	$\rightsquigarrow CN^* + CH^*$	0.333	1
	$\rightsquigarrow C_2H_2^* + N^*$	0.333	1
	$\rightsquigarrow CN + CH_2$	1	2
	$\rightsquigarrow H_2CCN^*$	1	3
CH_3CN			
CH_3CN + CR	$\rightsquigarrow CN^* + CH_2^*$	0.333	1
	$\rightsquigarrow CN^* + CH^*$	0.333	1
	$\rightsquigarrow C_2H_2^* + N^*$	0.333	1
	$\rightsquigarrow CN + CH_3$	0.500	2
	$\rightsquigarrow H_2CCN + H$	0.500	2
	$\rightsquigarrow CH_3CN^*$	1	3
HC_3N			
HC_3N + CR	$\rightsquigarrow C_3N^* + H^*$	0.333	1
	$\rightsquigarrow CN^* + CCH^*$	0.333	1
	$\rightsquigarrow$ l-$C_3H^* + N^*$	0.333	1
	$\rightsquigarrow CN + CCH$	0.500	2
	$\rightsquigarrow C_3N + CH$	0.500	2
	$\rightsquigarrow HC_3N^*$	1	3

Table C.2: Table of new suprathermal reactions of nitrogen bearing species discussed in Chapter 4. All reactions are for both surface ices and bulk ices.